Contents

Acknowledgments

This thesis would not have been possible without the help from my advisor, Professor Miklos Gyulassy. I wish to give my deepest gratitude to him for his patient guidance and heart-warming care. I also wish to express my sincerest respect for his hardworking spirit, which has always been inspiring to me.

I would like to thank Professor Allan S. Blaer for his assistance to my graduate life. I would like to thank Mrs. Anne Billups and Irene Tramm for their help when I was in the theoretical physics group. I would also like to thank Mrs. Della Jean Dumlao and Mr. David Yan for their kindly assistances. I would like to thank especially Mrs. Sarah Goldstein and Stephen Vance for correcting the English of this thesis.

Working with colleagues in the nuclear theory group, Dirk H. Rischke, Masayuki Asakawa, and Bin Zhang has been very harmonious. Last but not least, I thank all my fellow graduate friends, who have made my five years at Columbia University very enjoyable.

List of Figures

List of Tables

Chapter 1

Introduction

The quark-gluon plasma phase of matter [1, 2], a state consisting of weakly interacting deconfined quarks and gluons, was predicted to exist soon after the discovery [3] of the asymptotic freedom property of Quantum Chromodynamics (QCD). That novel phase of matter was predicted to occur perhaps deep in the cores of neutron stars [4] and during the first few moments (microseconds) of the Big Bang [5]. It was also suggested that perhaps the quark-gluon plasma could be formed in the laboratory in very high energy collisions of hadrons or nuclei [6]. Since the mid 1970's the experimental search for new phases of nuclear matter [7, 8] using heavy ion reactions has been underway. Until 1984 only light ion reactions were possible to study at energies below 2AGeV (GeV per incident baryon) [9]. In the past ten years, experiments with heavy ion with energies up to 200 AGeV have been investigated [10, 11, 12]. In 1999 a new era of experiments with heavy ion beams in the collider mode at the Relativistic Heavy Ion Collider (RHIC) at the Brookhaven National Laboratory (BNL) with center of mass energies up

to 100AGeV will begin.

In this chapter, we will review key elements of QCD thermodynamics and the dynamics of heavy ion reactions in order to put the thesis work described in the later chapters into context. The work on open charm that forms this thesis is related to the search for the QGP state of matter at RHIC energies. It deals with a probe of the earliest moments of heavy ion reactions and is expected to be one of the key diagnostic tools of that plasma. In Chapter 1.1 we will review, from both the perturbative QCD and lattice QCD calculations, the basic idea about the phase transition from hadronic matter to the quark-gluon plasma. In Chapter 1.2 we will introduce nuclear collisions as a tool of studying the quark-gluon plasma, and estimate thermalization and chemical equilibration processes in heavy ion collisions. Then in Chapter 1.3 we will review several of the important proposed observables including Heavy Quarkonia, dileptons, direct photons, disoriented chiral condensates (DCC), transverse flow, and Hanbury-Brown Twiss (HBT). Finally in Chapter 1.4 we will give the introduction on open charm signal, which is the main subject of this thesis.

1.1 Quark-Gluon Plasma

One of the most remarkable properties of the Standard Model of strong interactions, QCD, is that the fundamental color degrees of freedom carried by quarks and gluons can not be directly observed. That property, called confinement, restricts physical observables to composite color neutral objects

called hadrons and nuclei. It is thought that this property is caused by the very complex, non-perturbative nature of the physical vacuum. That vacuum structure is also thought to account for the observed breaking of the dynamical chiral symmetry of QCD [13]. The naive perturbative QCD vacuum is not the ground state, but has an energy density $B \approx 200\text{GeV/fm}^3$ above the physical vacuum that is filled with gluon and quark condensates. The rich hadron spectroscopy and complex strong interaction phenomenology is caused by that non-trivial vacuum structure. As T.D. Lee has repeatedly emphasized over the past 20 years [14], understanding that structure is one of the fundamental problems of modern physics.

One of the few untested and key predictions of the Standard Model is that the structure of the physical vacuum could drastically change at high temperature and baryon density. Due to asymptotic freedom, as discussed below, the condensates could melt at sufficiently high temperature, and thus hadronic or nuclear matter is expected to transform into a weakly interacting gas of partons.

1.1.1 Asymptotic Freedom

From perturbative QCD it is known that the coupling constant depends on the momentum scale Q [3]. For $SU(N)$ gauge theory with n_f flavours of fermions, this is expressed as the renormalization group equation:

$$\frac{d\alpha_s}{dt} = b_0\alpha_s^2 + b_1\alpha_s^3 + O(\alpha_s^4) \ , \tag{1.1}$$

where $t \equiv \ln(Q^2/\Lambda^2)$, and

$$b_0 = \frac{\beta_0}{4\pi} = \frac{1}{4\pi}\left(\frac{11N}{3} - \frac{2n_f}{3}\right) \quad , \tag{1.2}$$

$$b_1 = \frac{\beta_1}{16\pi^2} = \frac{1}{16\pi^2}\left[\frac{34N^2}{3} - \left(\frac{10N}{3} + \frac{N^2-1}{N}\right) n_f\right] \quad . \tag{1.3}$$

For example, for QCD $SU(3)$ theory the lowest order expression of the coupling constant is

$$\alpha_s^{LO}(Q^2) = \frac{4\pi}{\left(11 - \frac{2n_f}{3}\right)\ln\left(\frac{Q^2}{\Lambda^2}\right)} \quad , \tag{1.4}$$

where Q is the momentum transfer and $\Lambda \sim 200$MeV.

Therefore QCD has asymptotic freedom in that for $n_f \leq 6$ the running coupling constant approaches zero at the limit of $Q \to \infty$. This raises the possibility that we will have a free gas of quark and gluon plasma when the nuclear matter is at high temperature or at high density [1].

1.1.2 Deconfinement and Chiral Restoration

From the asymptotic freedom of QCD one expects to have an ideal gas of quarks and gluons at high temperature. However at low temperature quarks and gluons are subject to color confinement, and chiral symmetry is spontaneously broken. Therefore at some high temperature we expect to have deconfinement and chiral restoration.

The QCD Lagrangian can be written as

$$\mathcal{L} = \frac{1}{4}F^a_{\mu\nu}F^a_{\mu\nu} + \sum_i \bar{\psi}_i\left(D + m_i\right)\psi_i \quad , \tag{1.5}$$

where following quantities expressed in terms of the gauge field A^a_μ are:

$$F^a_{\mu\nu} = \partial_\mu A^a_\nu - \partial_\nu A^a_\mu + g f^{abc} A^b_\mu A^c_\nu \ , \tag{1.6}$$

$$D = \gamma_\mu \left(i\partial_\mu + \frac{1}{2} g A^a_\mu \lambda^a \right) \ , \tag{1.7}$$

$$A_\mu \equiv \frac{1}{2} A^a_\mu \lambda^a \ , \tag{1.8}$$

where λ^a are the generators of the $SU(N)$ group in the fundamental representation. The λ^a satisfy the following relations with f^{abc} being the antisymmetric $SU(N)$ structure constants:

$$\left[\lambda^a, \lambda^b \right] = 2i f^{abc} \lambda^c \ , \tag{1.9}$$

$$Tr \left(\lambda^a \lambda^b \right) = 2\delta^{ab} \ . \tag{1.10}$$

The above Lagrangian in eq.(1.5) has exact symmetry only when the quark masses are infinity or zero. In the former case we have the pure gauge theory with $Z(N)$ symmetry, and in the latter case we have chiral symmetry.

When the quarks are infinitely heavy, we can study the deconfinement phase transition from the breaking of the global $Z(N)$ symmetry in the pure gauge theory. The order parameter is found to be the Polyakov loop operator

$$L(\vec{x}) = Tr \mathcal{P} \exp \left(i \int_0^{1/T} dt A_0(\vec{x}, t) \right) \ , \tag{1.11}$$

which takes the trace of the path integral of an exponential function.

The thermal expectation value of the Polyakov loop operator is related to the free energy of inserting a static quark in the vacuum:

$$< L(\vec{x}) > = \exp \left(- \frac{F_q - F_0}{T} \right) \ , \tag{1.12}$$

where F_0 stands for the free energy of the vacuum.

In the confining phase the field can not be screened in the pure gauge theory, and the string potential grows linearly with distance, it therefore takes infinite free energy to insert a quark and $< L(\vec{x}) >= 0$. However in the deconfining phase the field can be Debye screened and this results in $< L(\vec{x}) > \neq 0$. Thus $< L(\vec{x}) >$ is the order parameter for the deconfinement phase transition and provides information on the breaking of $Z(N)$ symmetry in pure gauge $SU(N)$ theory.

It was pointed out by Svetitsky and Yaffe [15] that the four dimensional $SU(N)$ pure gauge theory at finite temperature is in the same universality class as the three dimensional $Z(N)$ spin theory. Numerical studies on the effective models give strong evidence that $SU(3)$ pure gauge theory goes through first order deconfinement phase transition [16].

The situation with dynamical quarks is quite different. The $Z(N)$ global symmetry is explicitly broken by the finite quark mass. In general it is expected that with dynamical quarks the confinement phase transition weakens, since the field can be screened by $q\bar{q}$ pair productions and the strings can be broken even in the confining phase [17].

On the other hand, when the quarks are massless, the QCD Lagrangian is invariant under the following transformations on the fermion fields ψ_i:

$$\psi_i \rightarrow e^{i\alpha}\psi_i \ , \tag{1.13}$$

$$\psi_i \rightarrow e^{i\alpha\gamma_5}\psi_i \ , \tag{1.14}$$

$$\psi_i^R \rightarrow U^R \psi_i^R \ , \tag{1.15}$$

$$\psi_i^L \rightarrow U^L \psi_i^L \ , \tag{1.16}$$

where γ_5 is the Dirac matrix, and

$$U^R, U^L \in SU(n_f) \ , \tag{1.17}$$

$$\psi_i^R = \frac{1+\gamma_5}{2}\psi_i \ , \tag{1.18}$$

$$\psi_i^L = \frac{1-\gamma_5}{2}\psi_i \ . \tag{1.19}$$

Hence the Lagrangian has the following chiral symmetry

$$U_V(1) \times U_A(1) \times SU_R(n_f) \times SU_L(n_f) \ . \tag{1.20}$$

However, $U_A(1)$ symmetry is broken by quantum effects, and the corresponding axial current [18]

$$j_\mu^5 = \sum_i \bar{\psi}_i \gamma_\mu \gamma_5 \psi_i \tag{1.21}$$

is not conserved. Instead we have the Adler-Bell-Jackiw anomaly [19] as

$$\partial^\mu j_\mu^5 = \frac{n_f g^2}{32\pi^2} Tr\left(\epsilon^{\mu\nu\lambda\sigma} F_{\mu\nu} F_{\lambda\sigma}\right) \ . \tag{1.22}$$

As a result the chiral symmetry is [20]

$$Z_A(n_f) \times SU_R(n_f) \times SU_L(n_f) \ . \tag{1.23}$$

Pisarski and Wilczek [21] studied the following Lagrangian with the above chiral symmetry

$$\begin{aligned} \mathcal{L}_{ch} &= \frac{1}{2} Tr\left(\partial_\mu \Phi^\dagger \partial^\mu \Phi\right) - \frac{1}{2} m_\Phi^2 Tr\left(\Phi^\dagger \Phi\right) + c\left(Det\Phi + Det\Phi^\dagger\right) \\ &\quad - \frac{\pi^2}{3} g_1 \left[Tr\left(\Phi^\dagger \Phi\right)\right]^2 - \frac{\pi^2}{3} g_2 Tr\left[\left(\Phi^\dagger \Phi\right)^2\right] \ , \end{aligned} \tag{1.24}$$

where the fields are

$$\Phi_{i,j} \propto < \bar{\psi}_i \left(1+\gamma_5\right) \psi_j > \ , \tag{1.25}$$

and where g_1, g_2 are related to β_1, β_2 in the renormalization group.

The order of the chiral phase transition from the above general Lagrangian is found to depend strongly on n_f. The transition is first order for $n_f \geq 3$. For $n_f = 1$ the transition does not even exist. For the interesting $n_f = 2$ case, the transition depends sensitively on the parameter c, the magnitude of the mass term. The phase transition is first order if $c = 0$, weakens when c becomes bigger, and even disappears if c is too large. The exact nature of the phase transition has also been studied with mean field analysis and lattice Monte Carlo calculations.

1.1.3 QGP Perturbative Equation of State

For QCD with massless quarks, the thermodynamic potential was calculated as a function of temperature

$$\begin{aligned} \Omega &\equiv \frac{-1}{VT^3} \ln Z \\ &= -\left[a_0 + a_2 g^2 + a_3 g^3 + \left(a_{4l} \ln g^2 + a_4\right) g^4 \right. \\ &\quad \left. + \left(a_{5l} \ln g^2 + a_5\right) g^5\right] + O(g^6) \ , \end{aligned} \tag{1.26}$$

where Z is the partition function. The first four coefficients in the above equation are derived in terms of number of colors and flavours [22]

$$a_0 = \frac{\pi^2}{45}\left(N^2 - 1 + \frac{7}{4} N n_f\right) \ , \tag{1.27}$$

$$a_2 = \frac{-1}{144}\left(N^2-1\right)\left(N+\frac{5}{4}n_f\right) \quad , \tag{1.28}$$

$$a_3 = \frac{1}{12\pi}\left(N^2-1\right)\left(\frac{N}{3}+\frac{n_f}{6}\right)^{3/2} \quad , \tag{1.29}$$

$$a_{4l} = \frac{1}{32\pi^2}N\left(N^2-1\right)\left(\frac{N}{3}+\frac{n_f}{6}\right) \quad . \tag{1.30}$$

Then other thermodynamic quantities such as energy density, pressure and entropy density are expressed in terms of the thermodynamic potential Ω:

$$p = T\partial_V \ln Z = -T^4\Omega \quad , \tag{1.31}$$

$$\epsilon = \frac{T^2}{V}\partial_T \ln Z = 3p - T^5\frac{d\Omega}{dT} \quad , \tag{1.32}$$

$$s = \frac{\epsilon+p}{T} = \frac{4p}{T} - T^4\frac{d\Omega}{dT} \quad . \tag{1.33}$$

We expect there to be a free gas of quarks and gluons at the weak coupling limit $g \to 0$, so the leading term a_0 in eq. (1.26) just gives the Stefan-Boltzmann quantities for massless bosons and fermions:

$$p = a_0T^4 = \frac{\pi^2}{90}\left[2(N^2-1)+\frac{7}{8}N\cdot 2\cdot 2n_f\right] \quad , \tag{1.34}$$

$$\epsilon = 3a_0T^4 = 3p \quad , \tag{1.35}$$

$$s = 4a_0T^3 \quad . \tag{1.36}$$

When one considers finite baryon density, one introduces the quark chemical potential μ, and then the equation of state (EOS) is given by [23]

$$p = \frac{\pi^2}{90}\left[2(N^2-1)+\frac{7}{8}N\cdot 2\cdot 2n_f\right]+\frac{Nn_f}{6}\left(T^2\mu^2+\frac{\mu^4}{2\pi^2}\right) \quad , \tag{1.37}$$

$$\epsilon = 3p \ , \tag{1.38}$$

$$n = \frac{N n_f}{3\pi^2}\left(\mu^3 + \pi^2 T^2 \mu\right) \ , \tag{1.39}$$

$$s = \frac{\epsilon + p - \mu n}{T} \ , \tag{1.40}$$

where n is quark number density. We mostly concentrate our discussions on the physics for zero baryon density case, since small baryon density is expected for very high energy heavy ion collisions.

Perturbative methods provide us with a powerful tool to study QCD [24]. However, the result is an expansion in the coupling g, which is of the order 1 at any practical energies despite the fact the it is a decreasing function of energy. Therefore the higher order terms in eq. (1.26) are comparable with the lower terms. Furthermore the expansion often encounters technical difficulties such as the summation of infinite terms with the same order.

We take eq.(1.26) as an example. In order to eliminate the infra-red divergence at $O(g^8)$, one has to introduce a magnetic mass in the gluon propagator [25]

$$m_M \propto g^2 T \ . \tag{1.41}$$

Then there are infinite number of diagrams contributing at $O(g^6)$, since a diagram with n number of four gluon vertices gives a term which is proportional to

$$g^6 \left(\frac{g^2 T}{m_M}\right)^{n-3} \ . \tag{1.42}$$

Although eq.(1.26) is a perturbative result, it includes infinite resummation of ring diagrams that take into account the polarization and screening effects of the plasma. Similar problems occur at all higher orders, and it seems impossible to solve the problem, which is called "Linde's disease", analytically via perturbative expansion. Thus even when g is small, it seems that we still can not solve the problem analytically. Non-perturbative calculations starting from first principle are therefore urgently needed.

1.1.4 QGP Non-perturbative Equation of State

In order to overcome the difficulties encountered in perturbative QCD calculations, lattice QCD was proposed by Wilson in 1974 [26]. Lattice QCD regularizes the QCD Lagrangian by fixing the lattice spacing. Then thermodynamic properties of the QCD can be studied by Monte Carlo simulation [27]. First one needs to discretize the QCD action

$$S = \int_0^{1/T} dx_0 \int_V \mathcal{L} \ , \tag{1.43}$$

where the QCD Lagrangian $\mathcal{L}$ is given by eq.(1.5).

Wilson proposed a way to map the gluon part of the action to lattice [26]. First a link variable is defined to be

$$U_{n,\mu} = \exp\left[-\frac{iga}{2}\sum_b \lambda^b A^b_\mu (x = n \cdot a)\right] \ , \tag{1.44}$$

where a is the lattice spacing, n^λ is a point in the four-dimensional Euclidean lattice, and μ labels the direction of the link. Then the gluon part of the

action is

$$S_G = \beta \sum_{n;\mu<\nu} P_{n,\mu\nu} = \beta \sum_{n;\mu<\nu} \left[1 - \frac{1}{N} ReTr \left(U_{n,\mu} U_{n+\mu,\nu} U^{\dagger}_{n+\nu,\mu} U^{\dagger}_{n,\nu} \right) \right] \quad , (1.45)$$

where Re takes the real part of a function, and

$$\beta = \frac{2N}{g^2} \quad . \tag{1.46}$$

The above gluon action is equivalent to that in the QCD Lagrangian eq.(1.5) at the continuum limit $a \to 0$. We expand the trace term in eq.(1.45) to $O(a^3)$:

$$\begin{aligned} U_{n,\mu} U_{n+\mu,\nu} &= e^{-igaA_\mu} e^{-igaA_\nu(x+a_\mu)} \simeq e^{-igaA_\mu} e^{-iga(A_\nu + a\partial_\mu A_\nu)} \\ &\simeq e^{-iga(A_\mu + A_\nu) - iga^2 \partial_\mu A_\nu + (iga)^2 [A_\mu, A_\nu]/2} \quad , \end{aligned} \tag{1.47}$$

$$U^{\dagger}_{n+\nu,\mu} U^{\dagger}_{n,\nu} \simeq e^{iga(A_\mu + A_\nu) + iga^2 \partial_\nu A_\mu + (iga)^2 [A_\mu, A_\nu]/2} \quad , \tag{1.48}$$

$$\begin{aligned} \Rightarrow U_{n,\mu} U_{n+\mu,\nu} U^{\dagger}_{n+\nu,\mu} U^{\dagger}_{n,\nu} &\simeq e^{-iga^2(\partial_\mu A_\nu - \partial_\nu A_\mu - ig[A_\mu, A_\nu]) + O(a^3)} \\ &= e^{-iga^2 F^a_{\mu\nu} \lambda^a/2 + O(a^3)} \quad , \end{aligned} \tag{1.49}$$

$$\begin{aligned} \Rightarrow P_{n,\mu\nu} &= 1 - \frac{1}{N} ReTr \left(e^{-iga^2 F^a_{\mu\nu} \lambda^a/2 + O(a^3)} \right) \\ &= \frac{g^2 a^4}{4N} F^a_{\mu\nu} F^a_{\mu\nu} + O(a^6) \quad , \end{aligned} \tag{1.50}$$

$$\Rightarrow S_G = \frac{2N}{g^2} \sum_{n;\mu<\nu} P_{n,\mu\nu} = \frac{1}{4} V_4 F^a_{\mu\nu} F^a_{\mu\nu} + O(a^6) \quad , \tag{1.51}$$

where

$$V_4 \equiv (N_t a)(N_s a)^3 = \frac{1}{T} L^3 \tag{1.52}$$

is the volume of the four dimensional lattice.

The lattice regularization of fermion action turns out to have fundamental difficulties. The naive regularization produces 16 poles in the fermion propagator, thus results in 16 fermions from the every one original fermion. This fermion doubling problem can be solved in at least two ways. Wilson [26] proposed to add a large mass term to eliminate all the other 15 unwanted fermions. However, the mass term explicitly breaks the chiral symmetry, which is very important for the study of QCD phase transitions. Kogut and Susskind [28] proposed a way to reduce the 16 fermions to 4 (staggered fermion formulation), and this method has the advantage that part of the chiral symmetry still remains. Wilson's fermion method and staggered fermion method will agree and both produce the continuum fermionic Lagrangian in the limit $a \to 0$.

In the staggered fermion formulation, the fermion part of the action is given in terms of the fermion fields $\chi(\bar{\chi})$, which are anticommuting Grassmann variables

$$S_F = \sum_i \bar{\chi}_{n,i} Q^i_{n,m} \chi_{m,i} \quad . \tag{1.53}$$

Here the fermion matrix Q includes the usual derivative term and the mass term.

Once one fixes the formulation of the fermion action S_F, the partition function on lattice becomes

$$Z = \int \prod_{n,\mu} dU_{n,\mu} \prod_{m,i} d\chi_{m,i} d\bar{\chi}_{m,i} e^{-S_G - S_F} \quad , \tag{1.54}$$

where $\chi_{m,i}$ are the fermion fields on lattice. Then the expectation value of an operator $\hat{O}$ is

$$< \hat{O} >= Z^{-1} \int \prod_{n,\mu} dU_{n,\mu} \prod_{m,i} d\chi_{m,i} d\bar{\chi}_{m,i} \hat{O} e^{-S_G - S_F} \quad . \tag{1.55}$$

Since the fermion action S_F is bilinear in the fermion fields, it can be integrated out and only the gluonic degrees of freedom remain:

$$< \hat{O} >= Z^{-1} \int \prod_{n,\mu} dU_{n,\mu} \hat{O} \prod_{i} \det Q^i e^{-S_G} \quad . \tag{1.56}$$

The lattice QCD results on phase transitions are summarized in Figure 1.1 from ref.[29]. The order of the phase transition is plotted as a function of the light quark mass $m_{u,d}$ and the strange quark mass m_s measured in units of a^{-1}. We proceed anti-clockwise from the upper-right corner. In pure gauge theory where all quarks are infinitely heavy, there is a first order phase deconfinement transition [30]. With two flavours of quarks with small but finite masses, one has the two solid boxes on the upper border of Figure 1.1 and there is no phase transition [29], but there is a rapid crossover [31]. For two massless quarks there is a second order transition. When we have three (or more) massless quarks, the transition is known to be first order; and it remains first order even for the case of three light quarks [29], which is represented by the lower solid circle. For QCD with one flavour of massless quark, there is no phase transition. In lattice QCD physical quantities are expressed in terms of the lattice spacing a. To have a feeling of the magnitude of a, $m_\pi a \sim 0.4$ in calculations of ref. [29]. Therefore the real world where one has two nearly massless quarks and one heavier strange quark lies in

the area represented by the virtual circle in Figure1.1. To probe near the real QCD, the lattice calculation with $m_{u,d}a = 0.025, m_s a = 0.1$ (solid box in the middle of the figure) was performed but showed no phase transition. However, the current lattice calculations have uncertainties due to finite size effects. For example, in ref. [29] $m_K/m_\rho = 0.46$ instead of the physical value of 0.64. Much more work needs to be done to determine the exact QCD phase diagram.

The lattice QCD results on the equation of state of $SU(3)$ pure gauge theory is shown in Figure 1.2 [32]. The upper dashed straight line is the Stefan-Boltzmann value for the energy density according to eq. (1.35), and the other plotted physical quantities are the values extrapolated to the continuum limit. One notices that the energy density quickly approaches the ideal gas value after T_c, however the pressure approaches slowly and thus gives the biggest deviation from the ideal gas equation of state, $\epsilon = 3p$, at $T \sim (1-2)T_c$. From the perturbative QCD result given by eq. (1.26), the deviation from the ideal gas equation of state is

$$\frac{\epsilon - 3p}{T^4} = -T\frac{d\Omega}{dT} \simeq c_1 g T \frac{dg}{dT} = c_2 g^4 \quad , \tag{1.57}$$

where

$$c_1 = -\frac{N(N^2-1)}{72}, \quad c_2 > 0 \quad . \tag{1.58}$$

The deviation can also be connected to the gluon condensate

$$\epsilon - 3p = < G^2 >_0 - < G^2 >_T \quad , \tag{1.59}$$

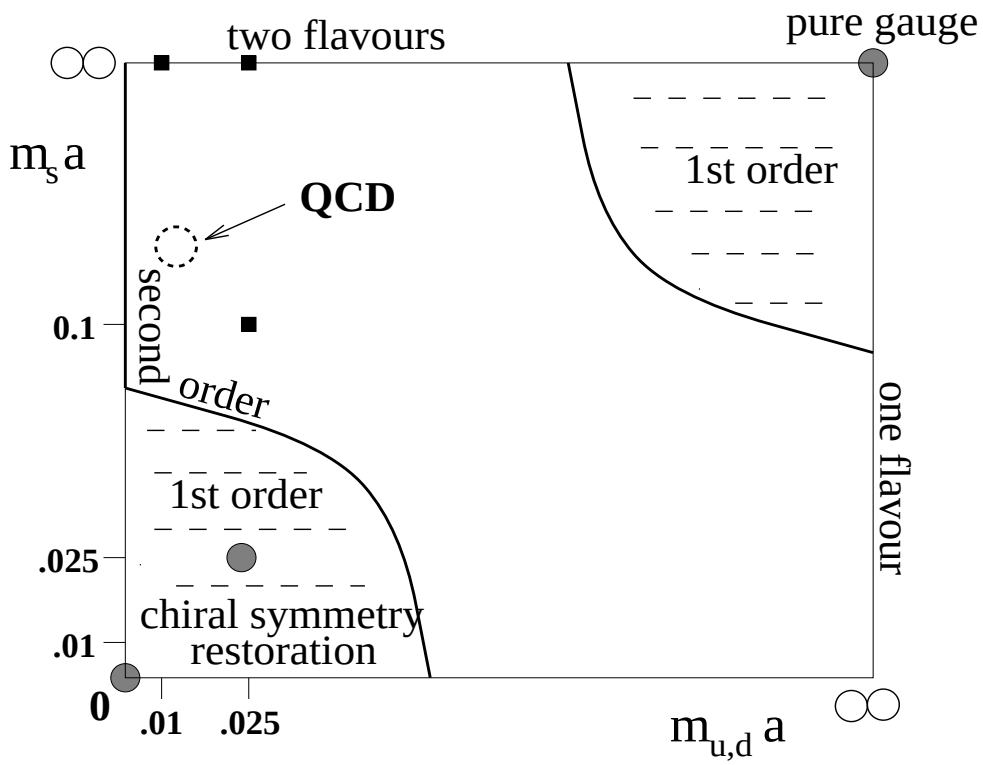

Figure 1.1: Phase transition from lattice QCD at finite temperature as a function of $m_{u,d}a$ and $m_s a$ from ref. [29].

where

$$< G^2 >_0 \sim 2 \text{ GeV/fm}^3 \ . \tag{1.60}$$

The zero temperature gluon condensate is important for the deviation of the quantity $(\epsilon - 3p)/T^4$ when close to T_c, and its effect decreases rapidly at high temperature. The deviation at high temperature $T/T_c \geq 2$ could be attributed to the leading order perturbative result in eq. (1.57) assuming a large running coupling constant $g^2(T) \sim 2$. However the perturbative expansion can not be expected to provide us a quantitative result in this case.

As seen above, the lattice calculation gives us valuable insight into the non-perturbative aspects of QCD. The critical temperature for the QCD phase transition appears to be about 150MeV [31], which means a critical energy density of about 1GeV/fm^3 according to eq. (1.35) for three flavour QGP. However, one needs higher temperature (and thus a much higher energy density) for the onset of the perturbative behaviour, as can be seen from Figure 1.2.

Nevertheless, one has to be careful when drawing conclusions from lattice QCD results before one understands uncertainties such as finite size effects. To give an example, we show the results of the equation of state for two flavour QCD. In Figure1.3 [33] energy density and pressure are plotted for two flavour QCD. The diamonds are the results on $N_t = 4$ lattices, while the circles and squares are those on $N_t = 6$ lattices. The bottom straight line indicates the Stefan-Boltzmann value for energy density, and the other two

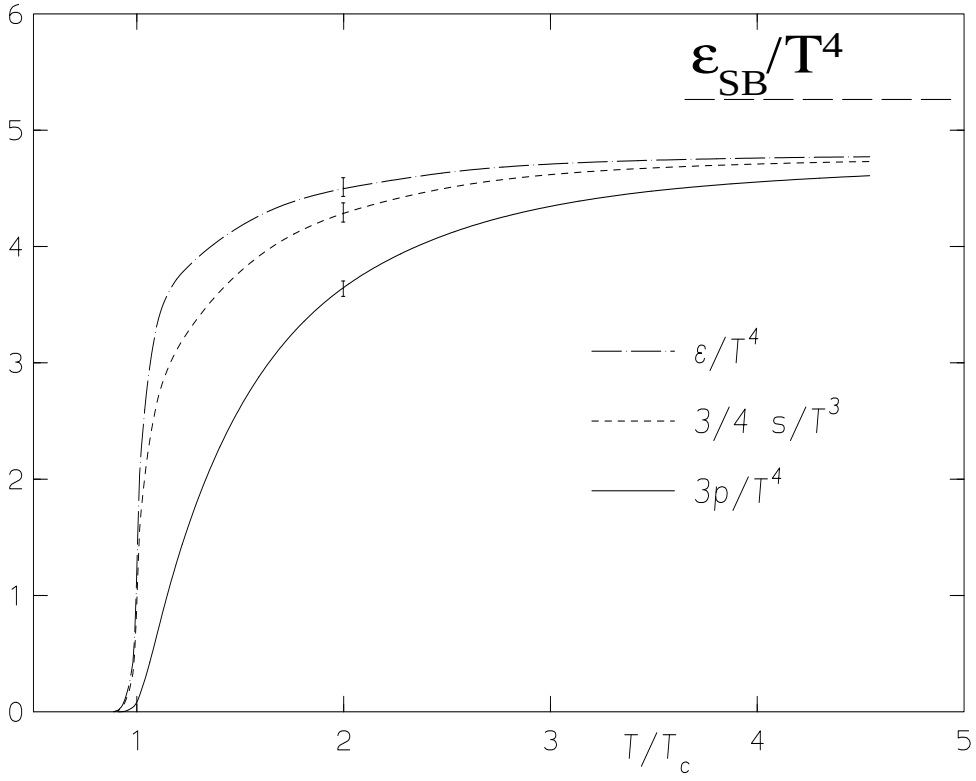

Figure 1.2: Energy density, entropy density and pressure for $SU(3)$ gauge theory as a function of T/T_c from ref. [32].

straight lines indicate the Stefan-Boltzmann values corrected for finite size effects.

By comparing $N_t = 4$ results with $N_t = 6$ results in Figure 1.3 one finds large finite size effects. This is not unexpected since one has significant finite size effect in the free theory on lattices already. For example, the finite temporal size effect for the energy density of an ideal gluon gas can be expressed approximately by [34]

$$\frac{\epsilon}{T^4} = \frac{3p}{T^4} \simeq (N^2-1)\frac{\pi^2}{15}\left(1 + \frac{30}{63}\frac{\pi^2}{N_t^2} + \frac{1}{3}\frac{\pi^4}{N_t^4}\right) \quad . \tag{1.61}$$

The finite temporal size effect can therefore be as large as 50% on $N_t = 4$ lattices for pure gauge theory. Improved actions on both gluon [35] and fermion part could help to limit the sensitivity to the finite size.

In order to improve the results from lattice QCD, larger machines are definitely needed. At present a 0.4 Teraflops supercomputer is under construction by N. Christ et al. at Columbia University [36]. That machine will be optimized for full QCD calculations, and will be one of the most promising lattice QCD projects to approach the continuum limit.

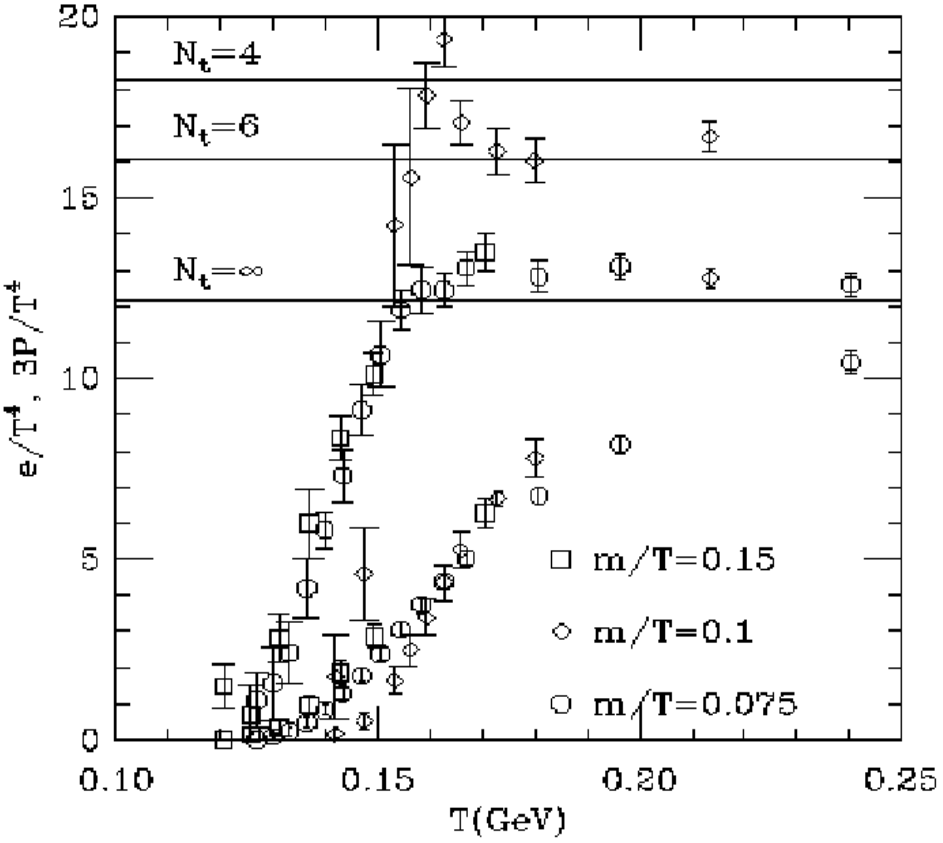

Figure 1.3: Equation of state for two flavour QCD on $N_t = 4$ and $N_t = 6$ lattices as a function of T from ref. [33].

1.2 Why Do We Need Heavy Ion Collisions?

In order to experimentally study the phase transition of the quark-gluon plasma, we need to achieve very high energy density in the lab. It is also important to have a large interaction volume in order to approach the thermodynamic limit of the new phase. It is hoped that high energy heavy ion collisions can provide us with these necessary conditions. Since the initial interaction volume and parton multiplicity turn out to be large, the dense parton system may go through both thermalization and chemical equilibration processes after its formation. At extremely high energies one may study an almost fully-equilibrated plasma of quarks and gluons with zero baryon density, and at currently accessible energies matter with high baryon density may be studies as well. The QCD phase transition is also expected to occur at high baryon density [2].

1.2.1 Glauber Geometry

In nuclear collisions many pp collisions occur almost simultaneously in a small nuclear volume. For hard perturbative QCD processes with small cross sections, the nuclear geometry and the QCD dynamics factorize to lowest order. Then it is assumed that they are independent two body reactions. For $A+B$ collisions at a fixed impact parameter $\vec{b}$, the number of binary collisions is given by [37]

$$N^{AB}(\vec{b}) = \int dp_\perp^2 dy_1 dy_2 d^2\vec{b}_1 d^2\vec{b}_2 \delta^{(2)}(\vec{b}-\vec{b_1}-\vec{b_2})$$

$$\times\, x_1\Gamma_{a/A}(x_1,Q^2,\vec{b_1})x_2\Gamma_{b/B}(x_2,Q^2,\vec{b_2})\frac{d\hat{\sigma}^{ab}}{d\hat{t}} \quad . \qquad (1.62)$$

For simplicity we do not consider nuclear shadowing effects in this section. Therefore the nuclear parton density in this case is simply

$$\Gamma_{a/A}(x,Q^2,\vec{s}) = T_A(\vec{s})f_{a/N}(x,Q^2) \quad , \qquad (1.63)$$

where $f_{a/N}(x,Q^2)$ is the structure function of parton a in the nucleon, and $T_A(\vec{s})$ is the nuclear thickness function

$$T_A(\vec{s}) = \int_{-\infty}^{\infty} dz n_A(\sqrt{z^2+|s|^2}) \quad , \quad \int d^2\vec{s}T_A(\vec{s}) = A \quad . \qquad (1.64)$$

To show A scaling of hard processes, we take the simplest hard sphere model with radius R_A for the nuclear density function

$$R_A \;=\; r_0 A^{1/3}, \quad r_0 \simeq 1.2 \text{ fm} \quad . \qquad (1.65)$$

Therefore

$$T_A(\vec{s}) \;=\; \frac{3A}{2\pi R_A^2}\sqrt{1-\frac{|s|^2}{R_A^2}} \quad , \qquad (1.66)$$

$$\Rightarrow N^{AB}(\vec{b}) \;=\; \int d^2\vec{b_1}d^2\vec{b_2}\delta^{(2)}(\vec{b}-\vec{b_1}-\vec{b_2})T_A(\vec{b_1})T_B(\vec{b_2})$$
$$\times \int dp_\perp^2 dy_1 dy_2 x_1 f_{a/N}(x_1,Q^2)x_2 f_{b/N}(x_2,Q^2)\frac{d\hat{\sigma}^{ab}}{d\hat{t}} \qquad (1.67)$$

$$\;=\; T_{AB}(\vec{b})\sigma^{pp} \quad , \qquad (1.68)$$

where

$$T_{AB}(\vec{b}) \;=\; \int d^2\vec{b_1}d^2\vec{b_2}\delta^{(2)}(\vec{b}-\vec{b_1}-\vec{b_2})T_A(\vec{b_1})T_B(\vec{b_2}) \qquad (1.69)$$

$$\;=\; \int d^2\vec{s}T_A(\vec{s})T_B(\vec{b}-\vec{s}) \quad . \qquad (1.70)$$

The scaling with atomic number A in central pA and AA collisions is, for example, given by

$$T_{pA}(0) = \int d^2\vec{s} T_p(\vec{s}) T_A(\vec{s}) \simeq \frac{3A^{1/3}}{2\pi r_0^2} \ , \tag{1.71}$$

$$\Rightarrow N^{pA}/N^{pp} \propto A^{1/3} \ . \tag{1.72}$$

$$T_{AA}(0) = \int d^2\vec{s} T_A^2(\vec{s}) = \frac{9A^{4/3}}{8\pi r_0^2} \ , \tag{1.73}$$

$$\Rightarrow N^{AA}/N^{pp} \propto A^{4/3} \ . \tag{1.74}$$

An estimate shows that minijet gluons may be produced with a cross section $\sim$ 10mb in pp collisions at $\sqrt{s} = 200$AGeV [38]. This estimate was obtained with a conservative transverse momentum cutoff $p_0 = 2$GeV for the gluon scattering process. Thus, according to the above scaling with atomic number A, the number of minijet gluons may be on the order of thousands at RHIC.

1.2.2 Global Features of Heavy Ion Collisions

In this section we review the standard calculations for certain global features of heavy ion collisions such as energy density, temperature and multiplicity.

At present there are two major facilities for heavy ion experiments: the Alternating Gradient Synchrotron at Brookhaven (AGS), and the Super Proton Synchrotron at CERN (SPS). They are both fixed target machines. The AGS accelerates nuclear beams from proton to gold up to the energy of $29(Z/A)$GeV, and the SPS accelerates beams from proton to lead up to the

energy of $400(Z/A)$GeV. Two larger colliders are under construction: the Relativistic Heavy Ion Collider at Brookhaven (RHIC) [39], and the Large Hadron Collider at CERN (LHC) [40]. RHIC is scheduled to be completed in 1999 with the center of mass energy of 200AGeV for $Au + Au$ collisions. Heavy ion physics is one important part for the LHC program, and the center of mass energy for $Pb + Pb$ collisions at LHC will be 5.4ATeV.

The total multiplicity rapidity density for pp collisions from SPS to Tevatron energies [41] has been fit with

$$\left(\frac{dN}{dy}\right)^{pp} \simeq 0.9 \ln\left(\frac{\sqrt{s}}{2m_p}\right) \quad . \tag{1.75}$$

For AA collisions, that density can be parameterized approximately as

$$\left(\frac{dN}{dy}\right)^{AA} \simeq A^{\alpha}\left(\frac{dN}{dy}\right)^{pp} \quad , \tag{1.76}$$

where α can be determined at least from lower energy pA data

$$\alpha \simeq 1.1 \quad . \tag{1.77}$$

In the standard scenario based on Bjorken's longitudinal boost-invariant boundary conditions [42], the initial volume is assumed to be

$$V_0 = \pi r_0^2 A^{2/3} \tau_0, \quad \tau_0 \simeq 1\text{fm} \quad , \tag{1.78}$$

and is furthermore assumed to grow linearly with proper time. Given the average transverse momentum of final particles,

$$< k_\perp > \quad \simeq \quad 400\text{MeV} \quad , \tag{1.79}$$

$$\Rightarrow < m_\perp > \quad \simeq \quad 500\text{MeV} \quad . \tag{1.80}$$

Hence the initial energy density is

$$\epsilon_0 = \frac{< m_\perp > (dN/dy)^{AA}}{V_0} \simeq 0.1 A^{\alpha-2/3} \ln\left(\frac{\sqrt{s}}{2m_p}\right) \text{ GeV/fm}^3 \quad . \qquad (1.81)$$

From this equation, we realize that the initial energy density grows as a power of A, the atomic number of the heavy ion beam, but only grow logarithmically with the center of mass energy. Therefore it is much more efficient to reach a higher initial energy density by using heavy ion collisions than increasing the beam energy alone.

According to eq. (1.35) we get the initial temperature assuming that the initial state is an ideal gas of gluons and three flavor of massless quarks:

$$T_0 = \left(\frac{30\epsilon_0}{47.5\pi^2}\right)^{1/4} \simeq \epsilon_0^{1/4} \times 150 \text{ MeV} \quad , \qquad (1.82)$$

where ϵ_0 is expressed in the unit of GeV/fm^3.

In Figure 1.4 we plot the initial energy density and temperature as a function of the center of mass energy. We use eq. (1.81) and eq. (1.82) from the standard scenario, and assume AA collisions with $A \simeq 200$.

Note that the multiplicity density dN/dy is about 300 times the energy density (in the unit of GeV/fm^3) according to eq. (1.81). In Figure 1.4 we see that almost all four experimental facilities can achieve an initial energy density above the critical $\epsilon_c \simeq 1$GeV/fm^3 for the QCD phase transition. However at the currently available AGS and SPS energies, the baryon stopping power is sufficiently large that matter is formed with high baryon density. We recall from the discussion of QCD thermodynamics that much less is known about

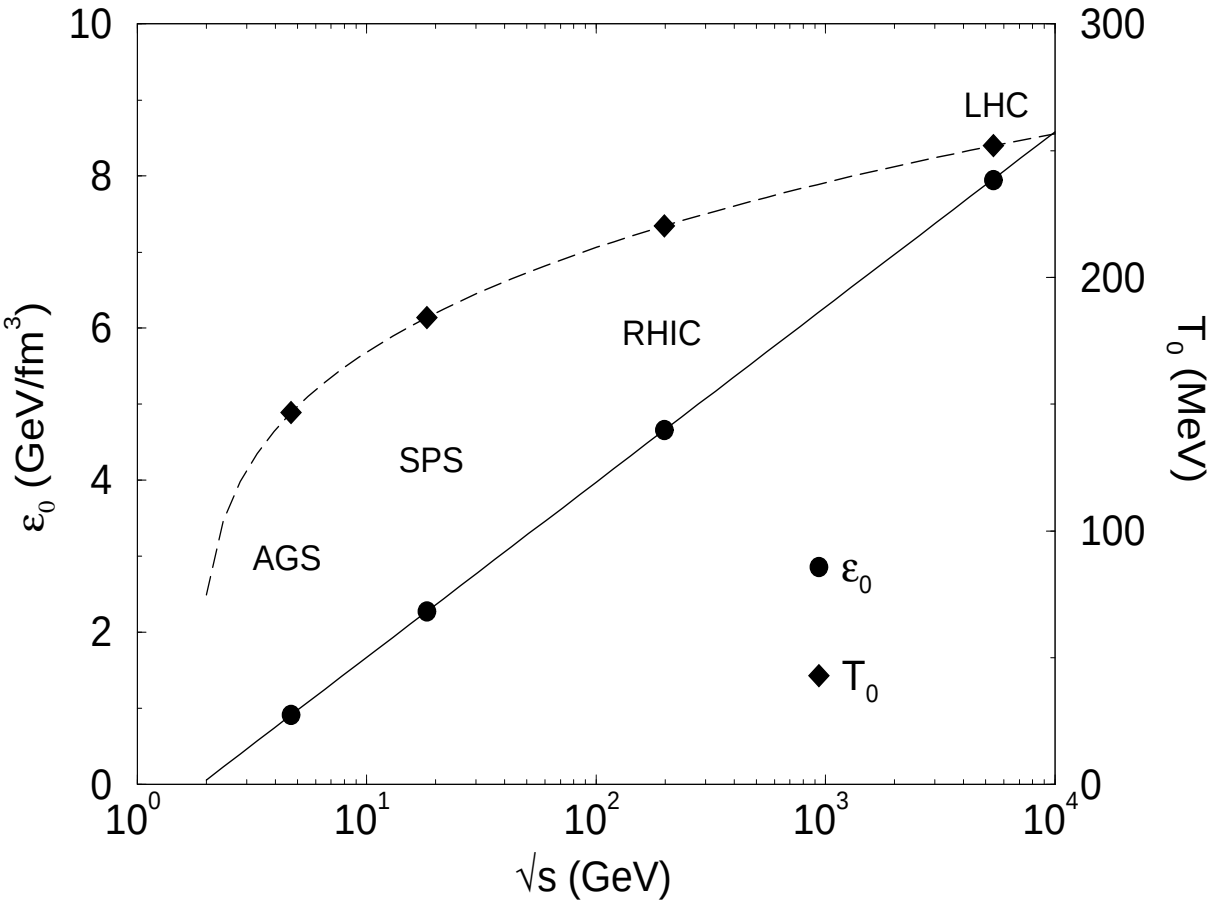

Figure 1.4: Initial energy density and temperature as a function of center of mass energy of heavy ion collisions.

the high baryon density case than the zero baryon density case, and we expect to gain valuable knowledge from these experiments. At future collider facilities, matter is expected to be formed at much lower baryon densities.

We have to stress that the above estimates for the global quantities in this section are based on a standard scenario, which only provides an order of magnitude estimate. Much higher energy densities may be achieved by taking multiple minijet production into account, as we discuss later in Chapter 3.1. Factors such as a bigger $< k_\perp >$ [43], a larger α from more secondary scatterings [44] as found in cascade models, and a smaller τ_0 as in the hot glue scenario [45] can all result in higher temperatures for the initial QGP system. However, we note that even the conservative estimate [42] stated above gives a high enough initial energy density to motivate the search for quark-gluon plasma in heavy ion experiments.

1.2.3 Thermalization

The quark-gluon plasma is defined to be an asymptotically free gas of quarks and gluons with both thermal and chemical equilibration. After the dense system of quarks and gluons is formed in high energy heavy ion collisions, it will approach thermalization via rescattering, and approach chemical equilibration via creation and annihilation processes. However, the parton system only has a finite lifetime. Thus it is important to know the time scales that the system requires to reach thermalization and equilibration, and whether the parton system can achieve both stages in its finite lifetime.

In this section we first follow Shuryak's estimate of the above elastic scattering cross sections [45], and remark on the limitations of that approach, and then estimate the thermalization time. Finally we introduce new results on parton energy loss [46], which imply that faster thermalization may be possible via inelastic processes.

The cross sections for the relevant elastic processes are

$$\frac{d\sigma}{dt} = \frac{\pi\alpha_s^2}{s^2}M^2 \ , \tag{1.83}$$

$$M^2_{gg\to gg} = \frac{9}{2}\left(3-\frac{ut}{s^2}-\frac{us}{t^2}-\frac{st}{u^2}\right) \ , \tag{1.84}$$

$$M^2_{gq\to gq} = -\frac{9}{4}\frac{u^2+s^2}{us}+\frac{u^2+s^2}{t^2} \ , \tag{1.85}$$

$$M^2_{qq\to qq} = \frac{4}{9}\frac{u^2+s^2}{t^2} \ . \tag{1.86}$$

One may estimate the above cross sections by separating them into large-angle and small-angle scattering parts [45]. Since most entropy in high energy heavy ion collisions is in gluons [38], let us consider gluons.

For an ideal gas of gluons at a temperature T,

$$n_g = \int 2(N^2-1)\frac{d^3p}{e^{p/T}-1} = \frac{(N^2-1)T^3}{\pi^2}\int_0^\infty \frac{z^2dz}{e^z-1}$$

$$= \frac{2(N^2-1)\zeta(3)}{\pi^2}T^3 \equiv a_1T^3 \ , \tag{1.87}$$

$$\zeta(3) \simeq 1.202 \ , \tag{1.88}$$

$$\epsilon_g = \frac{2(N^2-1)\pi^2}{30}T^4 \equiv a_2T^4 \ , \tag{1.89}$$

$$\Rightarrow p_g = \frac{\epsilon_g}{n_g} \simeq 3T \ . \tag{1.90}$$

For an ideal gas of quarks, equations become

$$n_q = b_1 T^3, \ b_1 = \frac{9 n_f \zeta(3)}{\pi^2} \ , \tag{1.91}$$

$$\epsilon_q = b_2 T^4, \ b_2 = \frac{7\pi^2 n_f}{20} \ . \tag{1.92}$$

For large angle scatterings, the matrix elements in eq. (1.86) are finite. Therefore one might estimate the corresponding relaxation time using the average values of the Mandelstam variables for an ideal gas of gluons:

$$< s > /2 = - < t > = - < u > \simeq (3T)^2 \ , \tag{1.93}$$

$$\Rightarrow \ < M^2_{gg\to gg} > \sim 30.4 \ , \tag{1.94}$$

$$\Rightarrow \ \frac{1}{\tau_g^{large-angle}} = n_g < \sigma > \sim n_g \frac{\pi \alpha_s^2}{< s >^2} < M^2 >< t > \sim 5\alpha_s^2 T. \tag{1.95}$$

For small angle scatterings, the matrix elements are divergent at $t, u \to 0$. If one just use the finite Debye mass [47] to regulate the divergence [45], then the contribution from small angle scattering is

$$t_{min} = \mu_D^2 = g^2 T^2 \ , \tag{1.96}$$

$$\Rightarrow < M^2_{gg\to gg} > \ \sim \ \frac{9}{2} \frac{s^2}{t_{min}} \ , \tag{1.97}$$

$$\Rightarrow \frac{1}{\tau_g^{small-angle}} \sim \frac{9\pi\alpha_s^2}{t_{min}} \sim 2.2\alpha_s T \ . \tag{1.98}$$

Therefore the estimate of the rate for gluon elastic scatterings is

$$\frac{1}{\tau_g} \sim 5\alpha_s^2 T + 2.2\alpha_s T \ . \tag{1.99}$$

The above method [45] of treating the small angle divergence is far from exact. Although Debye screening eliminates the divergence from longitudinal exchange of gluons, the transverse interactions, i.e. the color-magnetic interactions, can not be simply screened. This problem was discussed earlier by Danielewicz and Gyulassy [48]. Later Baym et al. [49] found that the Landau damping of transverse gluons provides an effective cutoff at a distance $\sim 1/\mu_D$ for the infrared divergence of transverse interactions. The result for the gluon relaxation time considering the viscosity of a quark-gluon plasma in the weak-coupling limit is given by

$$\frac{1}{\tau_g} \simeq 4\alpha_s^2 \ln(1/\alpha) T \quad . \tag{1.100}$$

Comparing eq. (1.99) to eq. (1.100), we note that the more precise dependence of the relaxation time τ_g on the coupling constant α in eq. (1.100) is hinted by the combination of linear and quadratic α dependent terms in the crude estimate found in eq. (1.99).

Now we take eq. (1.100) and find that for a high temperature $T \sim 0.5$GeV, the thermalization time for the gluons is large:

$$\alpha \sim 0.3 \ , \tag{1.101}$$

$$\Rightarrow \tau_g \simeq 1\text{fm} \ . \tag{1.102}$$

Simila ranalysis gives a quark relaxation time which is about twice larger than the gluon relaxation time. Thus, via elastic scatterings it is difficult to quickly approach thermalization.

However, thermalization may be accelerated by inelastic processes such as parton radiations from multiple scatterings in the dense medium and/or gluon multiplication processes ($2\ g \rightarrow n\ g$, $n \geq 3$) [50]. The radiative energy loss due to multiple scatterings was first considered in QED by Landau, Pomeranchuk and Migdal (the LPM effect) [51]. Similar effects were considered in QCD by Gyulassy and Wang [52], and recently new calculations from Baier, Dokshitser, Mueller, Peigné and Schiff (BDMPS) [46] yield unexpected results. Instead of being finite, the energy loss per unit length in QCD for a fast parton grows with the energy of the parton as $\sqrt{E}$ when the medium is infinite, or grows with the medium length L when the parton is extremely energetic. The BDMPS result for the spectrum of radiative gluon energy loss per unit length is given by [46]

$$\omega \frac{dI}{d\omega dz} = \frac{3\alpha_s C_R}{2\pi\lambda_g}\sqrt{\kappa \ln\frac{1}{\kappa}}\ , \tag{1.103}$$

where $\kappa = \lambda_g \mu^2/\omega$, w is the frequency of the radiation, μ is the Debye mass induced by the medium, λ_g is the mean free path for the gluon, and C_R is the Casimir operator for the parton.

In terms of radiation frequency, the LPM effect in QCD occurs for

$$\omega_{BH} \sim \lambda\mu^2 < \omega < \omega_{Fact} \sim \frac{\mu^2 L^2}{\lambda}\ , \tag{1.104}$$

while the Bethe-Heitler regime lies below ω_{BH}, and the factorization regime lies above the frequency ω_{Fact} and up to the energy of the parton, E.

In the case of an infinite medium, the LPM effect occurs for frequencies

up to the order of E, and therefore

$$-\frac{dE}{dz} = \int d\omega \left(\omega \frac{dI}{d\omega dz}\right) \propto \int d\omega \sqrt{\frac{1}{\omega}\ln\omega} \propto \sqrt{E}\ln E \ . \quad (1.105)$$

While in the case of an infinite energy E, the LPM effect stops at ω_{Fact}, thus

$$-\frac{dE}{dz} \propto L \ln L \ . \quad (1.106)$$

This nonlinear behaviour may imply a huge radiative energy loss for fast partons in a dense system. The strong radiation may accelerate the process of thermalization, which is probably slow when one only includes the elastic scatterings according to the previous estimate.

The previous estimate of thermalization time, e.g. eq. (1.99), assumed at the initial stage a chemically equilibrated gluon gas. With a high initial temperature, the corresponding gluon density is expected to be large, eq. (1.88). However, the initial gluon density produced via minijets and soft mechanisms may still not be high enough to populate the whole phase space. In order to study the chemical equilibration of the dense parton system, as will be discussed in the next section, one needs the initial condition including thermalization time scale, temperature and chemical compositions for quarks and gluons. Therefore one has to take the non-zero chemical potential into account.

1.2.4 Chemical Equilibration

Chemical equilibration is approached via flavour creation and annihilation processes. The evolution of chemical composition can be described by a set of master equations [53]. In order to solve the equations one usually assume that the partons have reached approximate thermal distribution. As we will see, the time scale for chemical equilibration is much longer than that for thermalization, and therefore the above assumption is supported.

As discussed in the previous section, gluons and quarks in general are not in chemical equilibrium. With non-zero chemical potential, one can introduce fugacity parameters λ_g and λ_q [43]:

$$f_i = \sum_n \lambda_i^n e^{-n\beta u\cdot k} = \frac{\lambda_i}{e^{-\beta u\cdot k} \pm \lambda_i} \simeq \frac{\lambda_i}{e^{-\beta u\cdot k} \pm 1} \quad , \tag{1.107}$$

where $i = g, q$, $\beta = 1/T$, and u^μ is the velocity of the local co-moving frame.

We study the following dominant processes for parton creation and annihilation

$$gg \leftrightarrow ggg, \quad gg \leftrightarrow q\bar{q} \quad . \tag{1.108}$$

For a baryon symmetric system where $n_q = n_{\bar{q}}$, the evolutions of the parton densities are

$$\partial_\mu (n_g u^\mu) = \frac{1}{2}\sigma_3 n_g^2 \left(1 - \frac{n_g}{\tilde{n_g}}\right) - \sigma_2 n_g^2 \left(1 - \frac{n_q \tilde{n_g}^2}{\tilde{n_q}^2 n_g^2}\right) \quad , \tag{1.109}$$

$$\partial_\mu (n_q u^\mu) = \frac{1}{2}\sigma_2 n_g^2 \left(1 - \frac{n_g}{\tilde{n_g}}\right) \quad , \tag{1.110}$$

where

$$\sigma_3 = < \sigma\,(gg \to ggg)\, v >, \quad \sigma_2 =< \sigma\,(gg \to q\bar{q})\, v > \ , \qquad (1.111)$$

$$\tilde{n_g} = n_g/\lambda_g, \quad \tilde{n_q} = n_q/\lambda_q \ . \qquad (1.112)$$

The temperature evolution is

$$\partial_\mu\,(\epsilon u^\mu) + p\partial_\mu u^\mu = 0 \ . \qquad (1.113)$$

During early times one can neglect transverse expansion, and assume the Bjorken longitudinal expansion, hence the above equation becomes

$$\frac{d\epsilon}{d\tau} + \frac{\epsilon + p}{\tau} = 0 \ . \qquad (1.114)$$

For a thermally equilibrated quark and gluon gas, according to eqs. (1.90) and (1.92), the energy density becomes

$$\epsilon = 3p = (\lambda_g a_2 + \lambda_q b_2)\, T^4 \ . \qquad (1.115)$$

Hence the solution of eq. (1.113) is just

$$\epsilon\tau^{4/3} = (\lambda_g a_2 + \lambda_q b_2)\, T^4 \tau^{4/3} = \text{constant} \ . \qquad (1.116)$$

With the assumption of pure longitudinal expansion, one has

$$\partial_\mu\,(n_i u^\mu) = \frac{\partial n_i}{\partial \tau} + \frac{n_i}{\tau} \ . \qquad (1.117)$$

Therefore one can write eqs. (1.109) and (1.110) as

$$\frac{\dot{\lambda}_g}{\lambda_g} + 3\frac{\dot{T}}{T} + \frac{1}{\tau} = R_3\,(1 - \lambda_g) - 2R_2\left(1 - \frac{\lambda_q^2}{\lambda_g^2}\right) \ , \qquad (1.118)$$

$$\frac{\dot{\lambda}_q}{\lambda_q} + 3\frac{\dot{T}}{T} + \frac{1}{\tau} = R_2\frac{a_1}{b_1}\left(\frac{\lambda_g}{\lambda_q} - \frac{\lambda_q}{\lambda_g}\right) \ , \qquad (1.119)$$

where the overdot represents the derivative with respect to τ, a_1 and b_1 are from eqs. (1.88) and (1.92), and

$$R_3 = \frac{1}{2}\sigma_3 n_g, \quad R_2 = \frac{1}{2}\sigma_2 n_g. \tag{1.120}$$

The above rates R_3 and R_2 contain infrared divergences. One can estimate the rates using the Debye screening mass for gluons and the thermal quark mass to regulate the divergences [43, 54, 55]. Numerical results for the estimate are shown in Figure. 1.5 [55].

The initial conditions for above differential equations as in the case of $Au + Au$ collisions at RHIC energy $\sqrt{s} = 200$AGeV is [43]:

$$\tau_{iso} = 0.7\text{fm}, \;\; n_0 = 3.2\text{fm}^{-3}, \;\; < k_\perp >= 1.17\text{GeV} \;\; . \tag{1.121}$$

Using eq. (1.115), $\epsilon_0 = 4n_0 < k_\perp > /\pi$, and $\lambda_q^0 = 0.16\lambda_g^0$ [55]

$$n = (\lambda_g a_1 + \lambda_q b_1)\, T^3 \;\; . \tag{1.122}$$

One can obtain initial values of fugacities and temperature

$$\lambda_g^0 = 0.05, \quad \lambda_q^0 = 0.008, \quad T_0 = 0.57\text{GeV} \;\; . \tag{1.123}$$

Given the above initial conditions, the chemical equilibration eqs. (1.116), (1.118) and (1.119) can be solved numerically, and results of which are shown in Figure 1.6 [55].

In Figure 1.6 the temperature in this calculation drops faster than in Bjorken's free streaming case, since some energy is used to produce more partons in order to approach chemical equilibration. Gluons are much more

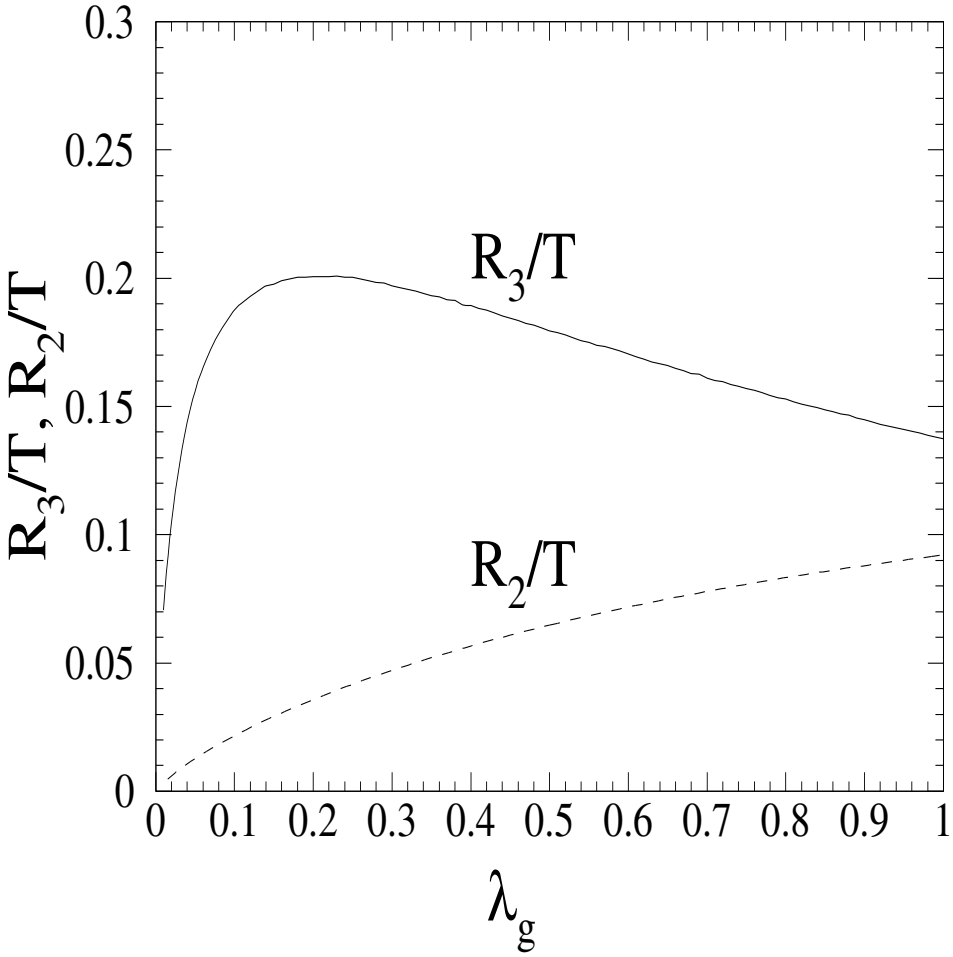

Figure 1.5: The gluon and quark production rates from ref. [55].

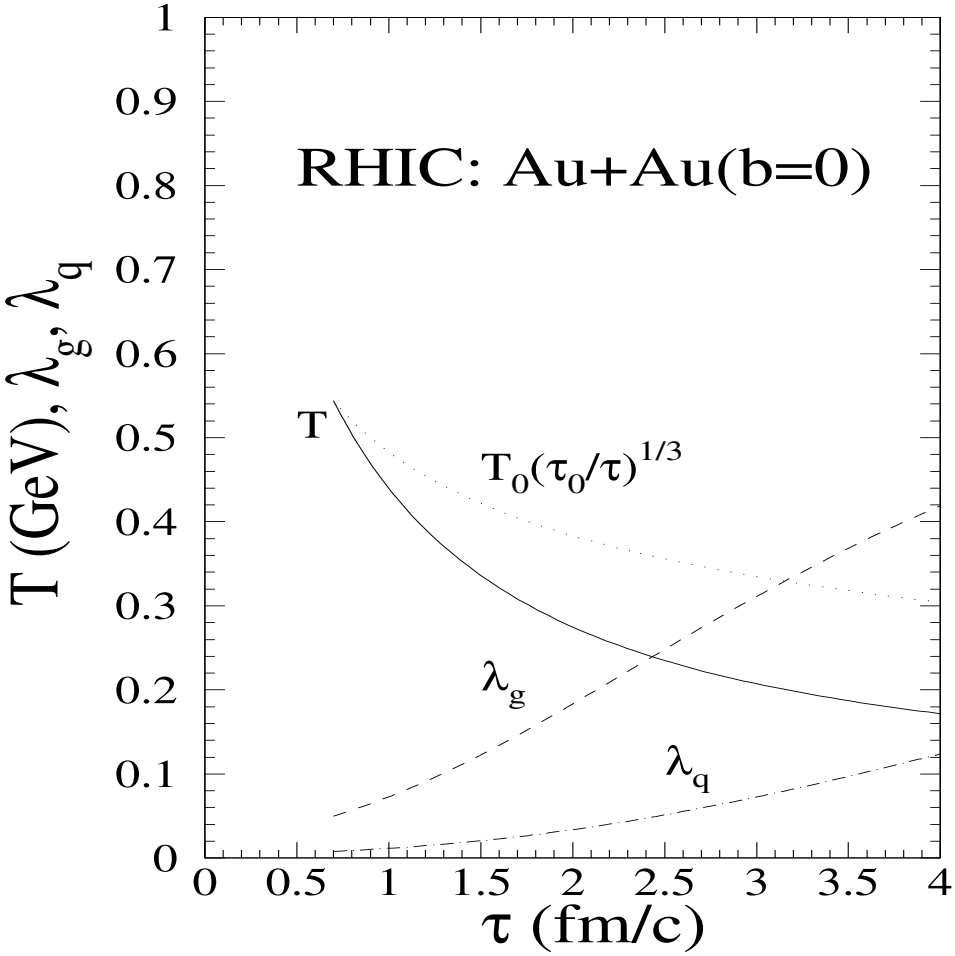

Figure 1.6: Chemical equilibration in $Au + Au$ collisions at RHIC from ref. [55].

likely to approach the chemical equilibrium than quarks. However, both of them can hardly reach chemical equilibrium within the lifetime of the plasma state.

One can see that the result in this study depends strongly on initial conditions. This particular set of initial conditions may be conservative. As discussed in Chapter 1.2.3, if fast thermalization could be achieved via inelastic processes, then one would begin with high initial parton fugacities, and the lifetime of the plasma would become longer. All of these contributions would accelerate the chemical equilibration. However, initial parameters are, unfortunately, quite uncertain since we have insufficient understanding of the soft physics. There are uncertainties in cutoff scales, rescattering cross sections, $2g \leftrightarrow ng$ process [50], and small-x gluon distributions. Therefore careful investigations are still needed to determine whether more equilibrated plasma can be formed at RHIC.

1.2.5 Phase Diagram

From lattice QCD numerical simulations, the QCD phase transition happens at $T_c = 150 \pm 10$MeV [31] at zero net baryon density. The QCD phase transition is also expected to occur at some high baryon density n_c^B at zero temperature, when the hadrons are so dense that the partons from different nucleons start to overlap. At present, there is no lattice QCD calculation on phase transitions with finite baryon density, and therefore there is uncertainty with the critical baryon density n_c^B. In general one expects that the QCD

phase transition occurs on a smooth curve on the plane of temperature T and the baryon chemical potential μ_B. In terms of baryon number densities, there is a jump from the hadronic phase to the QGP phase, just like the jump in the energy densities at zero baryon density. The phase diagram for the transition from the hadronic phase to the QGP phase is roughly plotted in Figure 1.7 as a function of the temperature T and the baryon chemical potential μ_B. Figure 1.8 shows the phase diagram as a function of the temperature T and the scaled baryon number density n_B/n_B^0, where $n_B^0 \simeq 0.14/\mathrm{fm}^3$ is the normal density in nuclear matter. The shaded area in Figure 1.7 represents the error from our current knowledge about the phase transition, and the shaded area in Figure 1.8 mostly represents the mixed phase.

Let us estimate the critical chemical potential at $T = 0$. For high density quark matter consisting of u, d quarks at zero temperature:

$$n_q = \frac{12}{(2\pi)^3}\int_0^{\mu_q} d^3p = \frac{2}{\pi^2}\mu_q^3 \ , \tag{1.124}$$

$$\Rightarrow \epsilon = \frac{3}{2\pi^2}\mu_q^4 \ . \tag{1.125}$$

If we assume that the QCD phase transition at zero temperature needs approximately the same critical energy density as in the zero baryon potential case, then

$$\epsilon_c \simeq 1\mathrm{GeV}/\mathrm{fm}^3 \ , \tag{1.126}$$

$$\Rightarrow \mu_q^c = \left(\frac{2\pi^2\epsilon_c}{3}\right)^{1/4} \simeq 480\mathrm{MeV} \ , \tag{1.127}$$

$$\Rightarrow \mu_B^c \simeq 3\mu_q^c = 1.4\mathrm{GeV} \ , \tag{1.128}$$

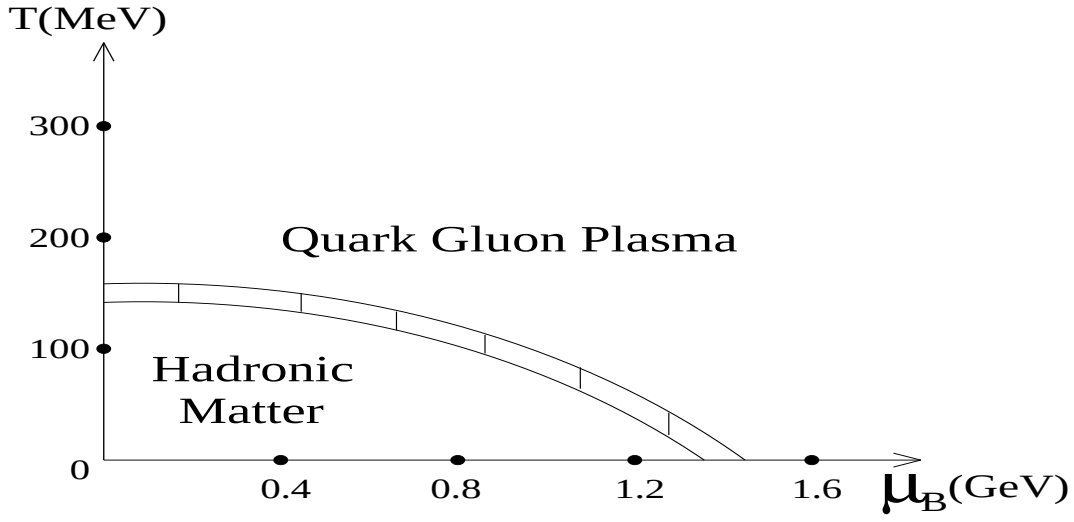

Figure 1.7: Schematic QCD phase transition diagram as a function of T and μ_B.

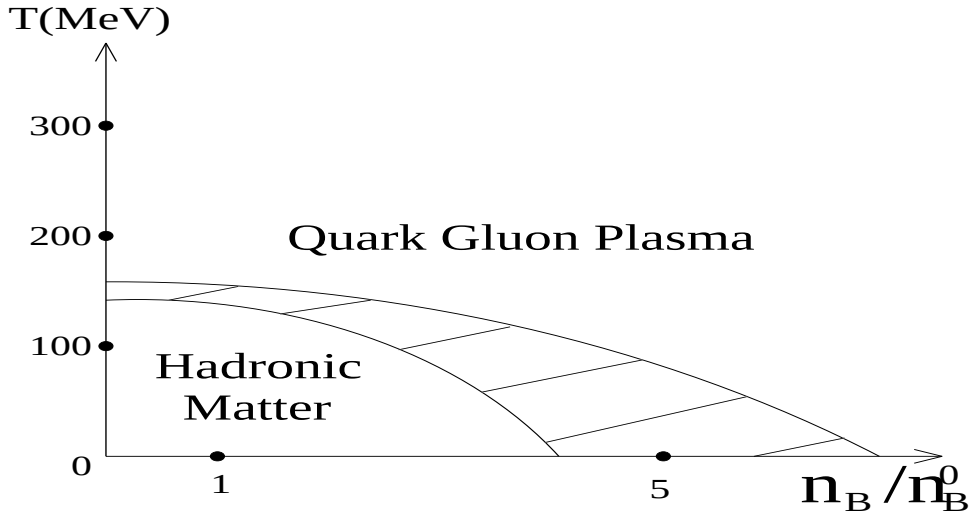

Figure 1.8: Schematic QCD phase transition diagram as a function of T and n_B/n_B^0.

$$n_B^c \simeq \frac{n_q^c}{3} = 0.93/\mathrm{fm}^3 \simeq 7 n_B^0 \text{ in quark matter phase.} \quad (1.129)$$

These estimates are consistent with the zero temperature values in Figure 1.7 and Figure 1.8. In order to obtain a general estimate on the phase transition boundary, expressions for the pressures in the two phases need to be known. The pressure $P_p(T,\mu)$ in the plasma phase is derived perturbatively and expressed in eq. (1.37). The hadronic equation of state can not be obtained from perturbative calculations, but can be parameterized for different hadron species. In this simple case one gets the parameterization of the EOS in the hadronic phase by adding the parameterizations for nucleons, pions and other resonances together. The energy density for nucleons, for example, can be parameterized as

$$\epsilon = n\left[m - W_0 + \frac{K(n/n_0 - 1)^2}{18} + \frac{3T}{2}\right] \quad , \quad (1.130)$$

where n is the nucleon density, m is the nucleon rest mass, W_0 is the binding energy, K represents the compressional energy density, and the last term is the thermal energy [56]. One then take Gibbs' criteria of phase equilibrium $P_h(T,\mu) = P_p(T,\mu)$ to determine the phase boundary curve $T_c(\mu)$, which is schematically shown in Figure 1.7 [57].

1.3 Signals of the Quark-Gluon Plasma

In this section we discuss several key observables of the quark-gluon plasma, as sketched in Figure 1.9. Among the probes of the early formed quark-gluon plasma, electromagnetic probes such as direct photons [45, 58, 59] and dileptons [6, 60] are the most direct signals, since they do not experience the subsequent thermalization and final state interactions. Heavy quarkonia [61] and heavy quark [44, 62] productions are also proposed to be the sensitive probes of the properties of the QGP. Recently new interesting experimental results such as low mass dilepton enhancement [63, 64] and J/ψ suppression in $A+B$ collisions [65] were presented. These results were heavily discussed at the Quark Matter'96 meeting [12].

1.3.1 Heavy Quarkonia

The production and suppression of heavy quarkonia bound states, such as J/ψ, was proposed by Matsui and Satz [61] to be an ideal test of the quark-gluon plasma production. The authors claimed that "there appears to be no mechanism for J/ψ suppression in nuclear collisions except the formation of a deconfining plasma, and if such a plasma is produced, there seems to be no way to avoid J/ψ suppression." The proposed suppression signature of QGP formation was first observed in 200 AGeV $O+U$ reactions at the CERN/SPS in 1987 [66]. However, far from settling the matter, the debate on the interpretation of those data and on the uniqueness of the QGP mechanism for suppression has only intensified since then.

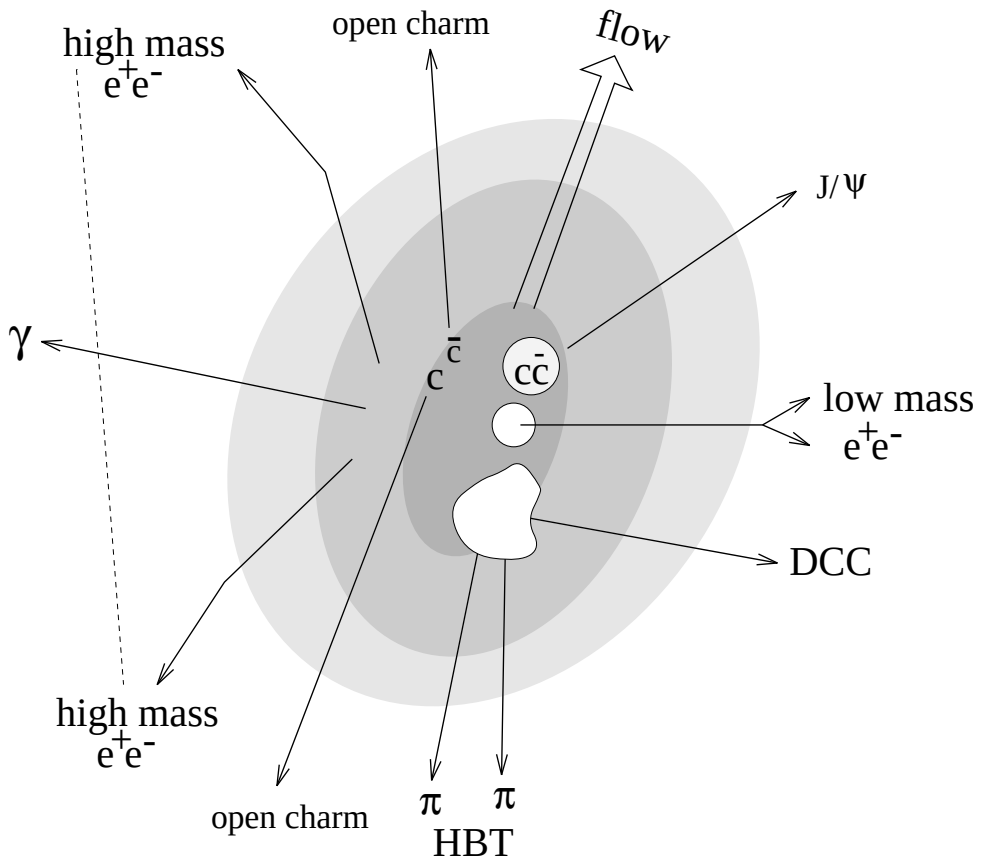

Figure 1.9: Several key observables of the quark-gluon plasma.

The nuclear suppression of charmonium was observed in p+A reaction and was found to depend linearly on $A^{1/3}$. In addition, the suppression was also observed for ψ'. Since the QGP production is *not* expected in $p+A$ collisions, alternate mechanisms for suppression of quarkonia production were proposed. One attempt to explain the $p + A$ data was to ascribe the suppression to nuclear gluon shadowing [67]. (We will discuss more fully the physics behind this effect later.) However, this explanation was later excluded because the lowest energy data at 150GeV did not fit into the universal shadowing curve. The most satisfactory explanation thus far [68] of J/ψ suppressions in both $p + A$ and *light* ion $O + U$ and $S + U$ reactions [69] is that it is due to pre-formation inelastic final state interactions of the color-octet $c\bar{c}g$ component which is produced in the initial hard glue-glue fusion event, with nucleons in the target with a cross section $\sigma_{\psi N} \sim 6mb$. In this **nucleon absorption model**, the J/ψ survival probability in nucleus A can be estimated as

$$S_A = \exp\left[-\int_{z_0}^{\infty} dz \rho_A(\vec{b}, z)\sigma_{\psi N}\right] \sim \exp\left(-\sigma_{\psi N}\rho_0 L_A\right) , \qquad (1.131)$$

where z is the longitudinal coordinate along the beam axis, and $\vec{b}$ is the impact parameter of the initial $gg \to c\bar{c}$ hard pQCD event in the target nucleus with density profile, ρ_A, normalized to A. The survival probability is the probability of having no final state interactions in the remaining part of the nucleus. It depends exponentially on the *effective* path length, L_A, travelled by the $c\bar{c}$ pair in a nucleus of mean density $\rho_0 \approx 0.14/\text{fm}^3$. We note that typically the average rapidity of the produced $c\bar{c}$ pair is high in the target frame and that is why the straight line (Eikonal) approximation can

be used.

In $A+B$ collisions, the data on quarkonia production are usually sorted in terms of an external calorimetric transverse energy trigger, E_T. The transverse energy is usually measured in a window with restricted rapidity and azimuthal angle coverages, and depends sensitively on the particular experimental device and configuration. Generally only a detailed Monte Carlo nuclear event generator such as HIJING [70] or VENUS [71] can provide a way to calculate the dependence of the observed transverse energy on the impact parameter of the collision. With such a generator, the conditional transverse energy probability density, $P^{AB}(E_T;\vec{b})$, that an $A+B$ reaction at impact parameter $\vec{b}$ will result in a measured E_T, can be estimated.

The survival probability of J/ψ in an $A+B$ reaction triggered with a given E_T can then be calculated as

$$\begin{aligned} S_{AB}(E_T) &\propto \frac{\sigma_\psi^{AB}(E_T)}{\sigma_{DY}^{AB}(E_T)} \\ &\propto \frac{1}{AB}\int d^2bP^{AB}(E_T;\vec{b})\, dz_A d^2b_A\; dz_B d^2b_B\; \delta^2(\vec{b}-\vec{b}_A-\vec{b}_B) \\ &\qquad \times \rho_A(z_A,\vec{b}_A)\rho_B(z_B,\vec{b}_B)e^{-\sigma_{\psi N}(\int_{z_A}^{\infty} dz\rho_A(\vec{b}_A,z)+\int_{z_B}^{\infty} dz\rho_B(\vec{b}_B,z))} \\ &= e^{-\sigma_{\psi N}\rho_0 L_{AB}(E_T)} \quad . \end{aligned} \tag{1.132}$$

In the first line the Drell-Yan cross section [72] is used to divide the quarkonium cross section, since the absence of final state interactions in $q\bar{q}\to\mu^+\mu^-$ makes the atomic number scaling of that cross section to be particularly simple. Integrated over transverse energy triggers and hence impact pa-

rameter, $\sigma_{DY}^{AB} = AB\sigma_{DY}^{NN}$. For the most central collision (high E_T) trigger $N_{DY}^{AA} \approx A^{4/3} N_{DY}^{NN}$ up to nuclear shadowing corrections. We note that both the above quarkonia and Drell Yan cross sections are understood to refer to comparable rapidity and transverse momentum kinematic regions.

In Figure 1.10 the ratio of J/ψ to Drell-Yan cross sections is plotted against the effective nuclear absorption length $L \equiv \langle L_{AB}(E_T) \rangle$. Unfortunately, the L dependence on the experimental observable E_T is rather model dependent [73]. Nevertheless, the exponential fit shows that both $p + A$ and $S + U$ data can be well explained taking $\sigma_{\psi N} \approx 6$ mb.

A caveat in the above nucleon absorption explanation of suppression in light ion reactions is that a larger suppression of ψ' is observed in $S+U$ collisions than for ψ [74]. This can only be understood in terms of an additional suppression mechanism that only applies to the larger sized ψ' states in the co-moving high density hadronic matter formed along side the quarkonium state.

The most provocative discrepancy seen in Fig. 1.10, however, is the failure of the nucleon absorption model to explain the latest data showing enhanced suppression of J/ψ in NA50 $Pb+Pb$ experiment [65]. The observed enhanced extra suppression of J/ψ in $Pb + Pb$ data has been interpreted [75] as the first direct evidence for the formation of quark gluon plasma.

The above claim has however been challenged by results of a recent study by Gavin and Vogt based on a more careful analysis of the co-mover suppression model [77]. In an earlier study of NA38 $S + U$ data, it is argued

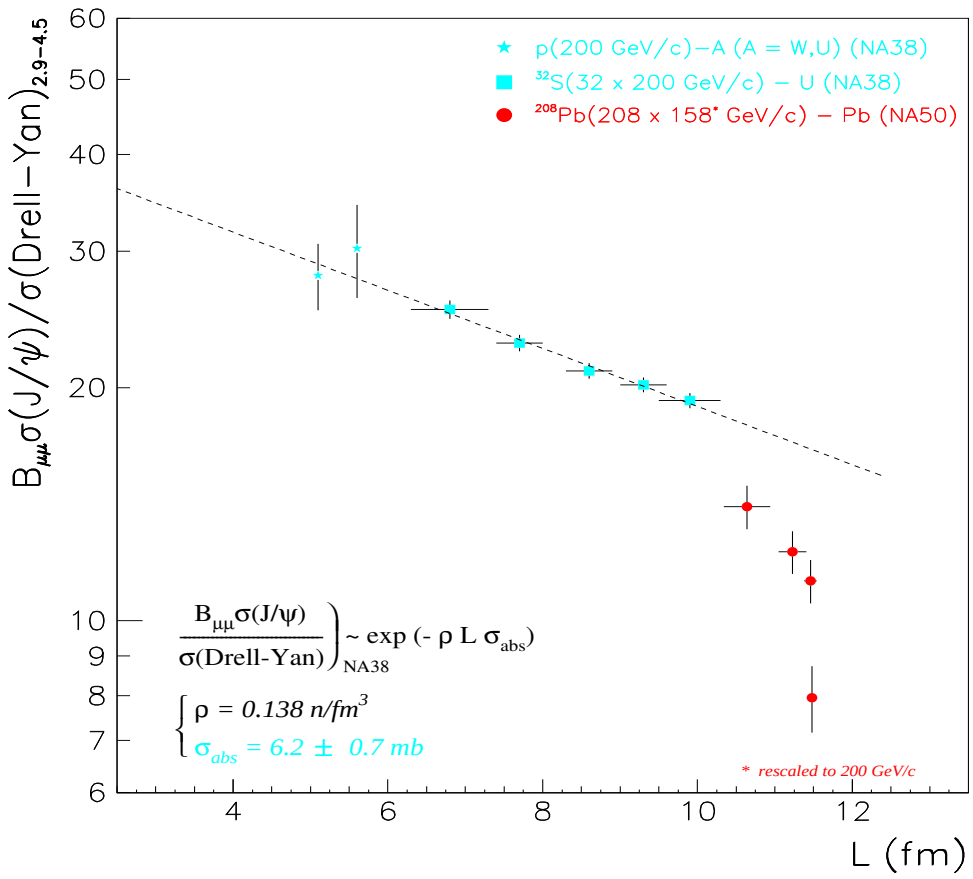

Figure 1.10: J/ψ to Drell Yan ratio in $p+A$, $S+U$ and $Pb+Pb$ collisions as a function of the average path length L from ref. [76].

[78] that nucleon absorption alone (even with a cross section of $7mb$) can not explain the E_T distribution of $S+U$ data, while co-mover dissociation cross section of $3mb$ together with nucleon absorption of $4.8mb$ could. Using the same parameters and updating the kinematical variables appropriate to the NA50 experiment, this model predicted the extra suppression of ψ in $Pb+Pb$ in quantitative accordance with the recent data.

The J/ψ survival probability due to co-mover scatterings can be simply estimated according to [79]

$$S_{co} = \exp\left(-\int_{\tau_0}^{\tau_F} d\tau n(\tau)\sigma_{co}v_{rel}\right) \ , \tag{1.133}$$

where due to Bjorken longitudinal expansion, the local co-moving density decreases with proper time as

$$n(\tau) = n_0\frac{\tau_0}{\tau} \ . \tag{1.134}$$

Here, τ_0 is the formation proper time of the quarkonium state in the frame where its longitudinal rapidity vanishes. The initial co-moving density is found to scale approximately linearly with transverse energy, $n_0 = \tilde{n_0}E_T/\tilde{E_T}$ [77]. The final proper time, τ_F, marking the time that the ψ exits the interaction area as it propagates in the transverse direction is approximately given by

$$\tau_F \approx \frac{R_A}{v_{rel}} \ . \tag{1.135}$$

The survival probability after the co-mover scattering with cross section σ_{co}

introduces another exponentially decreasing factor with increasing E_T:

$$S_{co} \simeq \exp\left[-\sigma_{co} v_{rel} \tilde{n_0} \tau_0 \ln\left(\frac{R_A}{v_{rel}\tau_0}\right) E_T/\tilde{E_T}\right] = \exp\left(-\beta E_T\right) \quad . \qquad (1.136)$$

Therefore, together with the nucleon absorption factor the survival probability including co-mover ψ dissociation processes is given schematically by

$$S_{AB}(E_T) \quad \propto < S_A S_B S_{co} > \sim e^{-\sigma_{\psi N}\rho_0 L_{AB}(E_T)} e^{-\beta E_T} \quad . \qquad (1.137)$$

Although the average nuclear absorption length $L_{AB}(E_T)$ grows with E_T, it has a geometrical upper limit $\sim (R_A + R_B)$ in central collisions. Therefore, nucleon absorption mechanism saturates at high E_T. However in central collisions E_T may fluctuate to higher and higher values as the local rapidity density of hadrons increases. Co-mover dissociation can therefore increase indefinitely with increasing E_T. The result of the detailed analysis [77] is shown in Figure 1.11. The suppression of J/ψ production as a function of the actual experimentally observed E_T is plotted for NA38 $S + U$ [69, 74] and NA50 $Pb + Pb$ data [65]. Furthermore, the co-mover model could also be adjusted to fit well the observed ψ' data in $p + A$, $S + U$ and $Pb + Pb$ collisions. This agreement indicates no compelling need to invoke the QGP explanation at this time from purely the phenomenological point of view. Theoretically, the validity of the large co-moving dissociation cross section has been questioned [80], but from the phenomenological side all the available data seem to be well accounted for by this conventional mechanism.

Another ambiguity associated with the interpretation of quarkonium data in terms of QGP formation is due to uncertainties in the basic production

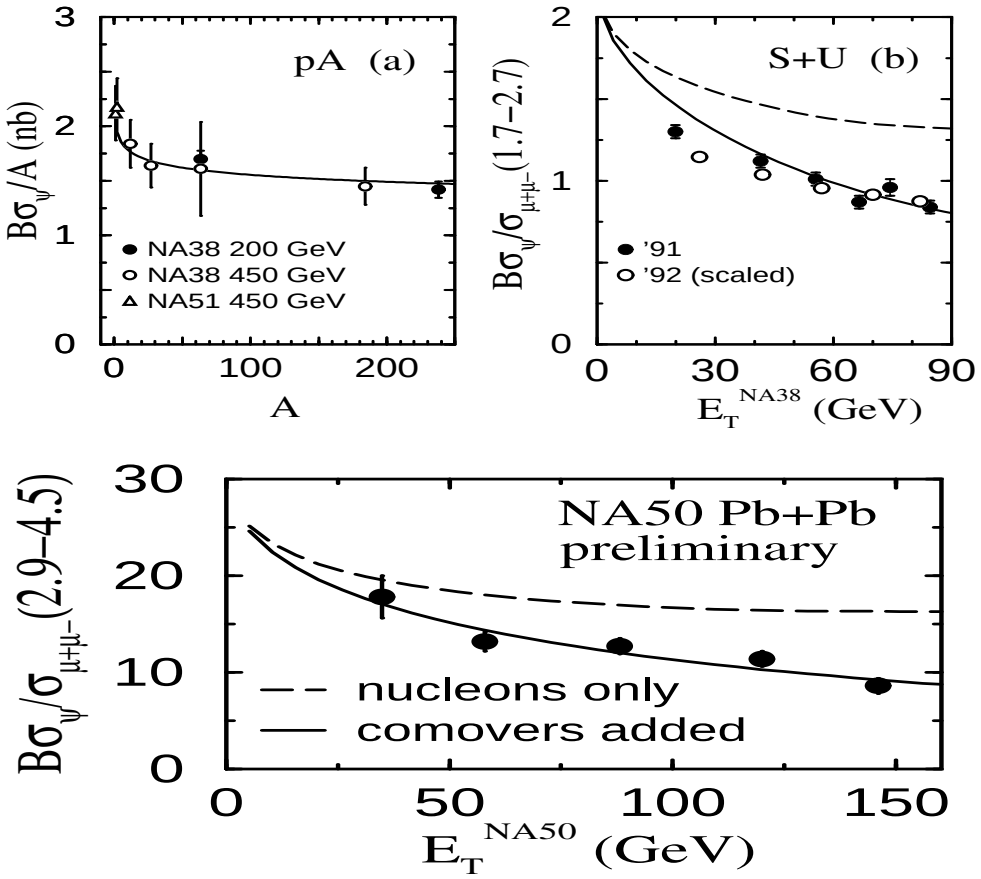

Figure 1.11: Co-mover J/ψ suppression vs $S+U$ and $Pb+Pb$ data from ref. [77].

mechanism of such bound heavy quark state even at the pp level. In the generalized version of the color evaporation model [81], it is assumed that charmonium cross sections are proportional to the sub-threshold charm cross section. With a fit proportionality constant of 3% [82], the model seems to give a good description (with a factor of 2) of the energy dependence of the total J/ψ production with pion and proton beams. It is also consistent with $\psi'/(J/\psi)$ ratio data. This model has only one parameter for any bound state. However, it remains to be justified that this factor is independent of processes. In particular, the factor for pion and proton beams differs somewhat and the color evaporation mechanism can easily depend on the environment and hence on A in nuclear reactions.

In the color-singlet model [83], on the other hand, it is assumed that charmonium cross sections are proportional to the cross section of forming a color-singlet $c\bar{c}$ state with the corresponding quantum numbers. Then the non-perturbative probability for the color-singlet state to convert to charmonium is related to the derivative of the wavefunction of the singlet state in the origin. This model was able to give absolutely normalized production cross section, and the ratio of different charmonium states. However, it completely fails to reproduce the high $p_\perp$ J/ψ data by orders of magnitude. Formally, its problem can be seen [84],e.g. via the infra-red divergence of the P-wave charmonium cross sections.

Recently, it was proposed that in some region of the phase space color-octet components might be dominant [85, 86]. Contrary to the color-singlet

model, the short-distance part of the interaction could also involve a color-octet $c\bar{c}$. Although the color-octet matrix elements are suppressed by powers of v, the relative velocity of the heavy quark in the quarkonia, color-octet mechanism might dominate in the processes where the leading term in v is suppressed by other small parameters such as strong coupling constant α_s or $m_Q/p_\perp$ at large transverse momentum. The conversion of the color-octet state to a color-singlet charmonium is described by non-perturbative matrix elements. With those color-octet matrix elements fixed by the data, the model gives good agreement with the shape of the $p_\perp$ distribution. Although the magnitudes of the unknown matrix elements are consistent with the non-relativistic QCD model (NRQCD) [87], more theoretical work is needed.

Given the above uncertainties in the production dynamics at the pp level as well as the ability for conventional nucleon absorption and co-mover dissociation mechanisms to explain the quarkonium data, it is important to consider a much wider class of observables in the search for QGP formation.

1.3.2 Dileptons

Dileptons are one of the direct electromagnetic probes. Thermal dileptons, for example, can tell us about the thermal profile of the dense plasma. In [59] it was proposed that in the hot-glue scenario, where the plasma is less chemically equilibrated but hotter than in the chemically equilibrated plasmas, dileptons of a few GeV energy will be enhanced over the standard scenario by a factor of 2.

However, in order to observe the interesting thermal signals, one has to deal with a large dilepton background. One such background is the dileptons decayed from heavy flavor meson pairs. In a study by Vogt et al. [88], it was suggested that dileptons from open charm decay would be about an order of magnitude above the thermal and Drell-Yan signals in the few GeV region, and therefore it would be very difficult to subtract this large background and observe the desired plasma signal. However, Shuryak [89] suggested that one important effect was missing in the arguments of that study [88], which was the energy loss of the charm quark in the dense medium formed after high energy $A + A$ collisions. Once one assumes that the charm quark would lose a finite amount of energy along its way (typically 2GeV/fm), then the dilepton spectrum from open charm will be pushed to the low mass region, and dileptons with a few GeV energy would be suppressed by over an order of magnitude. More theoretical work on the energy loss in a finite nucleus needs to be done before we know the magnitude of the suppression on high mass dileptons in $A + A$ collisions.

Very interesting data on low mass dilepton enhancement was reported at the Quark Matter'95 meeting [64, 90]. It was found that dileptons in the low mass region $0.2 - 1.5$GeV are enhanced by a factor of 5 in $S + Au$ collisions [63]. In Figure 1.12 the CERES $S + Au$ data is presented [64]. Similar effects were also observed in $S + W$ collisions [91].

Dileptons from vector mesons are of interest [92, 93] because they can provide information on the possible variation of hadron masses due to chiral

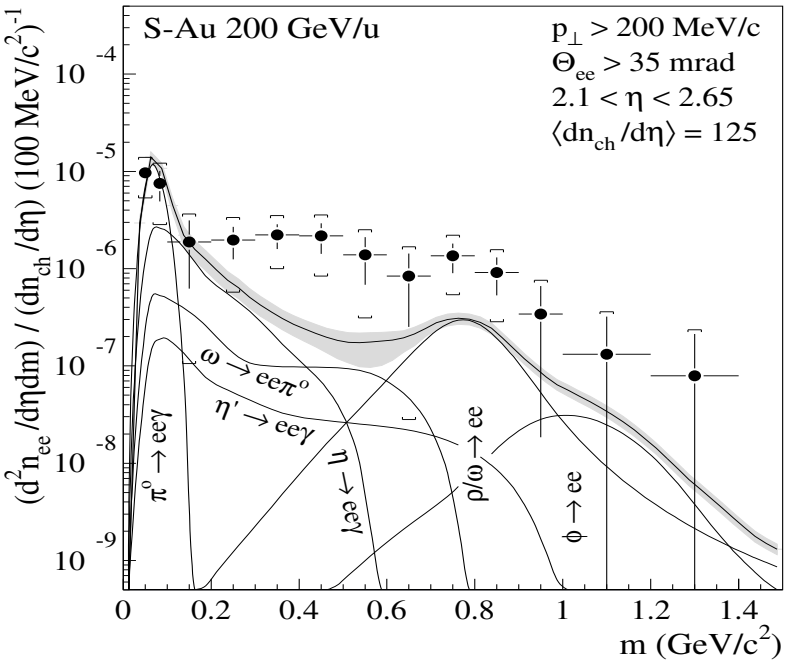

Figure 1.12: Low mass dilepton enhancement from CERES experiment from ref. [64].

symmetry restoration. The low mass dilepton enhancement was also one of the focal points of the Quark Matter'96 meeting [12].

It was proposed [94, 95] that the CERES data [63] could be explained by a drop of ρ meson mass in nuclear medium. In Figure 1.13 the assumption [95] of in-medium mass reductions of nucleons and ρ mesons is plotted for several baryon densities. The ρ mass was assumed to have dropped to 270MeV at the density $0.4/\mathrm{fm}^3$ and temperature 165MeV. However, this assumption of ρ mass drop is too large, and is inconsistent with QCD sum rules [96].

In Figure 1.14 the CERES data on low mass dilepton invariant mass spectra is plotted vs calculations from ref.[95] assuming the in-medium meson masses assumed in Figure 1.13. With the significant ρ mass reduction in the dense hadronic matter, the agreement with the CERES data is greatly improved in the invariant mass region from $2m_\pi$ to m_ρ.

In calculations from another group [97, 98] a smaller ρ mass dropping was assumed:

$$m_\rho^* \simeq m_\rho^0 (1 - 0.18\rho_B/\rho_0) \quad , \tag{1.138}$$

and these calculations also explained the CERES $S + Au$ data, as well as the HELIOS $S + W$ data [91].

We see that the explanations of the observed low mass dilepton enhancement are not unique. Different scenarios of ρ meson mass shifts in medium were assumed. In addition, the conventional scenario of the broadening of the ρ meson spectral function in medium [99] could enhance the low mass dileptons. The present experimental error bars are still too large to pin down

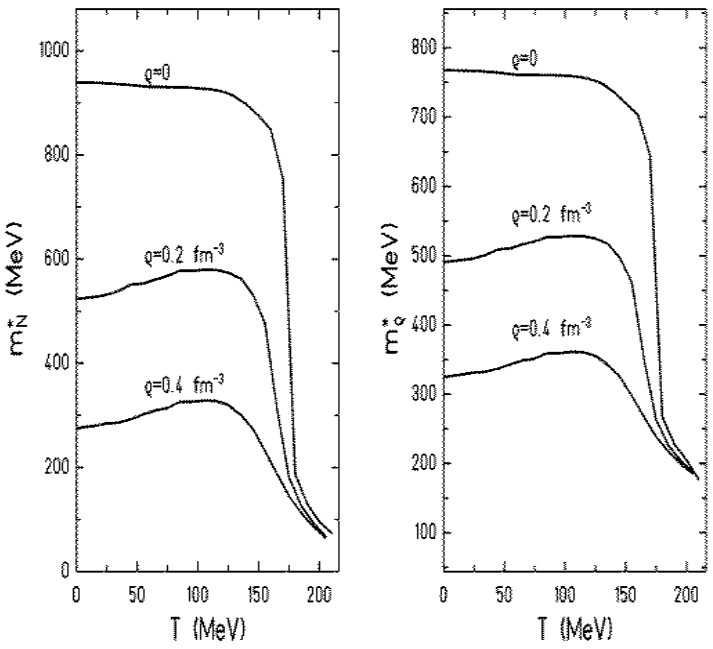

Figure 1.13: Assumption of in-medium nucleon and ρ meson masses as a function of temperature from ref. [95].

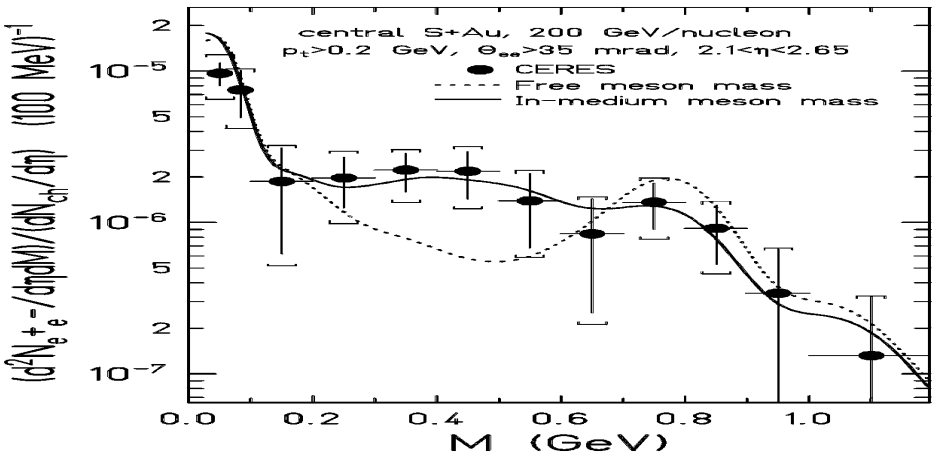

Figure 1.14: CERES data on low mass dileptons vs the calculation from ref. [95] assuming in-medium meson masses.

different models, and therefore more precise experimental data and further theoretical studies are needed to extract the physics from the CERES and HELIOS data.

1.3.3 Direct Photons

Direct photons are also one of the direct probes which could provide pristine information on the quark-gluon plasma. In addition, since the direct photon production in nucleon-nucleon collisions [100] is understood, its production in nucleus-nucleus collisions could provide constraints on the little-known gluon structure functions in the nucleus via the Compton process $gq \rightarrow q\gamma$.

Data on single photons in $S+Au$ collisions [101] was claimed to be understood only if the quark-gluon plasma is formed, because an overly simplified hadronic fireball model led to yields an order of magnitude [102, 103] above the data. The problem with this interpretation is that the fireball model is inconsistent with the observed rapidity and transverse momentum distributions.

A Large background is another problem with the direct photon measurements. Compared to dileptons, the photon background, which mainly comes from π_0 and η decays, is usually much higher [90]. Direct photon signatures are therefore rather difficult to disentangle [104].

1.3.4 Disoriented Chiral Condensate

The restoration of chiral symmetry at high temperatures is one of the most basic features of the QCD matter. According to lattice QCD calculations the critical temperature for chiral restorations coincides with that for the deconfinement transition. Thus the chiral phase transition in QCD is expected from both the theory study and lattice numerical simulations [21, 105]. A possible signal for the chiral transition is the formation of a coherent pion field called the disoriented chiral condensate (DCC) [106, 107, 108]. In equilibrium, a DCC can not grow larger than $\sim 1/T_c \sim$ 1fm [107]. However, in non-equilibrium it is possible to grow larger. A large domain of DCC will manifest itself by the striking fluctuation in the spectrum of neutral and charged pions in terms of the ratio $n_{\pi^0}/n_{\pi}^{total}$. There also exists some cosmic ray data [109] with that ratio far from the average value 1/3.

Most studies of this phenomena are based on the linear sigma model, with the effective potential as

$$V_{eff} = \lambda(\vec{\pi}^2 + \sigma^2 - v^2)^2/4 - H\sigma \quad , \tag{1.139}$$

where $m_\sigma = \sqrt{2\lambda v^2}$ as the sigma mass at $T = 0$ if $H = 0$, The explicit chiral symmetry breaking term $H\sigma$ takes into account the non-zero mass of the quarks in the real world. In the so-called quench scenario [108], the initial $(\sigma, \vec{\pi})$ field is assumed to be symmetric under chiral transformations

$$\sigma \rightarrow \sigma + \vec{\epsilon} \cdot \vec{\pi} \quad , \tag{1.140}$$

$$\vec{\pi} \rightarrow \vec{\pi} - \vec{\epsilon}\sigma \quad , \tag{1.141}$$

with $< \sigma >=< \pi_i >= 0$. The evolution of the field is then described by zero-temperature equations of motion. Long wavelength modes of the pion field are amplified according to

$$\frac{d^2}{dt^2}\vec{\pi}_k = (\lambda v^2 - k^2)\vec{\pi}_k \ , \tag{1.142}$$

because the Mexican-hat form of the effective potential makes the $\sigma = \pi_i = 0$ point unstable. In this quenched scenario the domain size could grow as large as $4 - 5$fm [110]. In the annealing scenario, $(\sigma, \vec{\pi})$ mean fields evolve almost synchronously with the effective potential, thus the system just oscillates close to the equilibrium point. Long wavelength modes are less amplified and domain size is therefore smaller [110].

DCC growth depends strongly on the initial condition, and it is one main uncertainty in present DCC studies [110, 111]. Furthermore, most studies are based on the linear sigma model, and this model is not dependable at the starting chiral symmetric phase where the temperature is above T_c. To verify that some pions come from the coherent source of the DCC domain, one can seek secondary signals such as pion pair correlations. However, Asakawa probed that the pion pair correlations are very small and mainly at $\theta = 180°$ [112]. Theories must be improved in order to give the size of the DCC domain in heavy ion collisions and/or the possibility that we would observe a strong pion number imbalance. Experiments to detect DCC formation could be done at RHIC, or as proposed in [113].

1.3.5 Directed Transverse Flow

Transverse flow from azimuthal anisotropy was observed recently in $Au + Au$ collisions at 10.8AGeV at the AGS [114]. It was first discovered in 1984 at much lower energies at Bevalac [115], and has been the subject of intense studies since then. In general, flow can provide information on the compressibility of the dense baryonic system and on the equation of state. It can also assist us in studying the role of the mean field in nuclear collisions.

The azimuthal distribution of energy and multiplicity would be isotropic if there were no collective transverse flow. Transverse flow manifests itself via the anisotropy in the azimuthal distribution on an event-by-event basis. To study the anisotropy, one can Fourier-transform the distribution $f(\phi)$ [116]:

$$f(\phi) = \sum_i f_i e^{in\phi} = \sum_i v_i e^{-i\psi_n} e^{in\phi} \quad . \tag{1.143}$$

For real functions, the above equation can be written as

$$f(\phi) = \sum_i v_i \left[\cos(n\psi_n)\cos(n\phi) + \sin(n\psi_n)\sin(n\phi)\right] \quad . \tag{1.144}$$

Anisotropy gives non-zero values of v_n ($n \geq 1$). Variables v_1 and ψ_1 for the first harmonic represent a shift of the center of the isotropy circle, with ψ_1 being the azimuthal angle of the reaction plane, which is the plane formed by the beam axis and the impact parameter vector. The variable v_2 represents the eccentricity of the ellipse in the reaction plane.

The above analysis is complicated by the fluctuation resulting from finite multiplicity in a nuclear collision [117]. Therefore the reaction plane can not

be exactly determined event by event, and the values of ψ_n suffer from this uncertainty. More importantly, the above variables for the harmonics for an ensemble of events are described not by a constant, but by a Gaussian distribution with a finite width.

The two-dimensional Gaussian would be centered at zero if there were no transverse flow:

$$\frac{d^2w}{v_n dv_n d\psi_n} = \frac{1}{2\pi\sigma_n^2} e^{\frac{-v_n^2}{2\sigma_n^2}} \quad . \tag{1.145}$$

Assuming that the fluctuation changes little with transverse flow, for

$$f(\phi) = \sum_i f_i \delta(\phi - \phi_i) \tag{1.146}$$

we have

$$v_n^2 = \frac{1}{\pi^2} < \sum_i f_i^2 >= \frac{N}{\pi^2} < f_1^2 > \quad , \tag{1.147}$$

$$\Rightarrow \sigma_n = \frac{N}{\pi^2}\sigma_1 \quad . \tag{1.148}$$

Note that σ_n is independent of n, and we now denote it as σ.

With transverse flow, the Gaussian is centered at non-zero $(\tilde{v_n}, \tilde{\psi_n})$:

$$\frac{d^2w}{v_n dv_n d\psi_n} = \frac{1}{2\pi\sigma^2} e^{-\frac{(\vec{v}_n - \vec{\tilde{v}}_n)^2}{2\sigma^2}} = \frac{1}{2\pi\sigma^2} e^{-\frac{v_n^2 + \tilde{v_n}^2 - 2v_n\tilde{v_n}\cos(\psi_n - \tilde{\psi_n})}{2\sigma^2}}, \tag{1.149}$$

$$\Rightarrow \frac{d^2w}{v_n dv_n} = \frac{1}{\sigma^2} e^{-\frac{v_n^2 + \tilde{v_n}^2}{2\sigma^2}} I_0(\frac{v_n\tilde{v_n}}{\sigma^2}) \quad , \tag{1.150}$$

where $I_0(x)$ is the modified Bessel function.

Redefining the dimensionless variable as

$$x_n \equiv \frac{v_n}{\sigma} \quad , \tilde{x_n} \equiv \frac{\tilde{v_n}}{\sigma} \quad , \tag{1.151}$$

the new distribution becomes

$$\frac{d^2w}{x_n dx_n} = \frac{1}{\sigma^2} e^{-(x_n^2+\tilde{x}_n^2)} I_0(x_n \tilde{x}_n) \quad . \tag{1.152}$$

The above distribution $\frac{d^2w}{x_n dx_n}$ resembles a Gaussian function when $\tilde{x_n} < 1$ and then is hard to be distinguished from the finite multiplicity fluctuation. However, when the transverse flow is strong enough so that $\tilde{x_n} > \sqrt{2}$, it has a minimum at $x_n = 0$, which is a distinct signature for the transverse flow.

From the experiment E877 at AGS [118], clear transverse flow signal is observed. In mid-central events, a clear minimum in the $\frac{d^2w}{v_1 dv_1}$ distribution is seen. The v_1 coefficients extracted from transverse energy anisotropy and multiplicity anisotropy are quite different, and the reason is that nucleons and pions have different flow patterns. For protons, transverse flow grows linearly as a function of p_T, and reaches 20% of the total transverse momentum at $p_T = 1$GeV. From the comparison with different transport models such as RQMD [119] and ARC [120], one can study the effect of the mean field in the nuclear collisions. The most striking collective flow signature of a QGP formation has been predicted to be a local minimum of the flow excitation function at the so-called "softest point" of the nuclear matter [121]. This proposed signature is being looked for at AGS.

1.3.6 Hanbury-Brown Twiss

Correlation functions for identical particles probe the source size and freeze-out time of the dense medium [122, 123]. The two-particle correlation func-

tion in momentum space is defined as

$$C_2(\vec{p}_1, \vec{p}_2) \equiv \frac{P(\vec{p}_1, \vec{p}_2)}{P(\vec{p}_1)P(\vec{p}_2)} \quad . \tag{1.153}$$

If the particles are classical without dynamical correlations, the above function is always equal to 1. For identical quanta with bosonic statistics [124], symmetrization introduces a dependence on two momenta and $C_2(\vec{p}_1, \vec{p}_2) = 2$ without dynamical correlations. More generally, for a source described by seven-dimensional phase space density function $S(x, \vec{p})$, the semi-classical expression for the correlation function is given by [123, 125]

$$C_2(\vec{K}, \vec{q}) = 1 + \frac{\int d^4x d^4x' S(x, \vec{K}) S(x', \vec{K}) e^{iq(x-x')}}{\int d^4x S(x, \vec{p}_1) \int d^4x' S(x', \vec{p}_2)} \quad , \tag{1.154}$$

where $\vec{K} = (\vec{p}_1 + \vec{p}_2)/2$, $q = (E_1 - E_1, \vec{p}_1 - \vec{p}_2)$, and $\int d^4x S(x, \vec{p}) \equiv P(\vec{p})$.

For an azimuthally symmetric source [126]

$$S(x, \vec{p}) \propto \exp\left[-\frac{x^2 + y^2}{2R_\perp^2} - \frac{z^2}{2R_z^2} - \frac{(t - t_0)^2}{2\Delta^2}\right] \quad , \tag{1.155}$$

using

$$q_0 = E_1 - E_2 = \frac{\vec{p}_1^{\,2} - \vec{p}_2^{\,2}}{E_1 + E_2} \simeq \frac{\vec{K} \cdot \vec{q}}{E_K} \equiv \vec{\beta} \cdot \vec{q} = \beta_{out} q_{out} + \beta_{long} q_{long} \quad , \tag{1.156}$$

where q_{long} is defined to be the component of $\vec{q}$ along the beam direction, q_{out} is the transverse component which is in the plane with the beam direction and the K vector, and q_{side} is the other orthogonal transverse direction. The approximation sign is valid for $|\vec{q}| \ll |\vec{K}|$, and $\beta_{side} \propto K_{side} = 0$ by definition. Thus

$$C_2(\vec{K}, \vec{q}) \;\; = \;\; 1 + \exp\left[-R_\perp^2(q_x^2 + q_y^2) - R_z^2 q_z^2 - \Delta^2 q_0^2\right] \tag{1.157}$$

$$\simeq \quad 1+\exp\left[-q_{side}^2 R_\perp^2 - q_{out}^2(R_\perp^2+\beta_{out}^2\Delta^2)\right.$$
$$\left.-q_{long}^2(R_z^2+\beta_{long}^2\Delta^2) - 2\beta_{out}\beta_{long}q_{out}q_{long}\Delta^2\right]. \quad (1.158)$$

In the longitudinally co-moving system (LCMS) where $K_{long}=0$, it becomes

$$C_2(\vec{K},\vec{q}) = 1+\exp\left[-q_{side}^2 R_\perp^2 - q_{out}^2(R_\perp^2+\beta_{out}^2\Delta^2) - q_{long}^2 R_z^2\right]. \quad (1.159)$$

Experimentally one usually uses the parameterization [127]

$$C_2(\vec{K},\vec{q}) = 1+\lambda\exp\left[-q_{side}^2 R_{side}^2 - q_{out}^2 R_{out}^2 - q_{long}^2 R_{long}^2\right] \quad . \quad (1.160)$$

Thus one can obtain information about the space-time dimension and expansion velocity of the emitting source from the fitted radius parameters. The chaoticity parameter λ is different from 1 due to other correlations and resonance decays. For charged particle correlations such as pion and kaon correlations, the Gamov correction due to Coulomb interactions is important and must be included. Data from $p+Pb$, $S+Pb$ and $Pb+Pb$ collisions [128] show that the fitted radii grow with the size of the system, and are generally larger than the projectile size. Pions have larger radii and smaller chaoticity than kaons due to more resonance decays. Because of collective flow phenomena associated with transverse expansion, the above simple formulae (1.158-1.160) are modified. The fitted radii do not correspond directly to the source size but must be interpreted in terms of a detailed transport model. Pion interferometry can nevertheless serve as a powerful signal of the QGP formation. Given a rapid crossover region around T_c, the speed of sound C_s^2

acquires a local minimum near T_c. As matter cools and crosses that mixed phase region, the minimum of C_s^2 causes the transverse expansion to stall for some time. This leads to the time delay signature of the phase transition that could be seen in detailed systematics of the q_{out}, q_{side} dependences of the function $C_2(q_{out}, q_{side})$ [121].

1.4 Open Charm

One of the main uncertainties in heavy ion physics is the initial conditions of the dense parton system. As shown in section1.2.4, for example, the initial momentum distribution, energy density and chemical composition determine the fate of the QGP. If the assumed initial conditions in eq. (1.121) [43] are true, we may not have fully equilibrated quark-gluon plasma at RHIC. Recently it is found that minijets lead to initial conditions characterized by large fluctuations of the local energy density and of the collective flow field. The "hot spots" [129] corresponding to higher local energy density may change the usual picture from cylindrically symmetric, homogeneous quark-gluon plasma to turbulent, volcanic plasma. Certain signals of QGP may be sensitive to this change of the initial condition. Initial conditions are themselves determined by the parton structure functions from the two colliding nuclei, mostly by the gluon structure function. Parton distributions in nuclei are depleted due to nuclear shadowing effects [130, 131]. As we go to higher energies in search of the quark-gluon plasma, we can see softer (small-x) partons deeper in the shadowing regime. It is therefore important

to understand nuclear parton distributions in order to calculate reliably all the other observables in $A + A$ collisions.

Open charm production is well suited to measure the initial gluon structure function and its nuclear modifications. At collider energies $\sqrt{s} > 200$ AGeV the initial minijet plasma is mostly gluonic [45, 38] with a quark content far below its chemical equilibrium value. Because open charm is produced mainly through gluon fusion, it can provide information on both the incoming gluon structure functions and the later-formed dense minijet plasma.

This thesis on open charm production [132] in high energy nuclear collisions is motivated by two recent studies [62, 44] which predicted widely different rates. In [62] the pre-equilibrium contribution was found to be almost equal to the initial gluon fusion rate, similar to the suggestion of the charm enhancement from thermal productions in the hot-glue scenario [45]. In [44], a more provocative claim was made that open charm may even be enhanced by over an order of magnitude above the initial perturbative QCD (pQCD) rate.

The proposed method to measure charm meson ($D/\bar{D}$) cross section at the Relativistic Heavy ion Collider (RHIC) is $e\mu$ coincidence measurements, or dilepton measurements. Traditionally, dileptons from charm decay are regarded as background, while thermal dileptons or Drell-Yan dileptons are considered as signals. Dileptons from Drell-Yan process probe the quark degrees of freedom, and thermal dileptons tell us about characteristics such

as temperature and phase transition in the dense plasma. However, those signals will probably be overshadowed by the large background of dileptons from charm meson ($D/\bar{D}$) decay in $Au + Au$ collisions at RHIC [88], and it is easier to measure the dileptons from open charm decay. In the QCD factorization limit, open charm mainly comes from initial gluon fusion, and it thus depends strongly on the gluon distribution in the nuclei.

The thesis discussed at length in the next chapters consists of two parts. First, it is shown that the pre-equilibrium charm production is small compared to the initial fusion rate [132, 54]. Second, it is shown that this dominance of the initial gluon fusion mechanism can be used to probe the gluon shadowing in nuclei [133]. While the first result of the thesis work is pessimistic in the sense that it indicates, contrary to an earlier claim [44], that open charm is not a good probe of the QGP formation, the second result is optimistic as it provides a new tool to measure the gluon shadowing via $p + A$ reactions.

Perturbative QCD analysis [131, 134] predicts that the gluon structure will be depleted at $x < 0.01$ due to gluon recombination processes. Shadowing of the quark nuclear structure functions, $q_A(x, Q^2)$, is well established from deep inelastic $\ell A \to \ell X$ reactions [130]. For heavy nuclei, the quark structure functions are shadowed by a factor, $R_{q/A}(x \ll 0.1, Q^2) \approx 1.1 - 0.1\ A^{1/3}$, nearly independent of Q^2. It is far less known about the gluon shadowing. In high energy nuclear collisions, the gluon nuclear structure is of central importance since it controls the rate of minijet production that de-

termines the total entropy produced at RHIC and higher energies [135]. The understanding of the gluon shadowing is therefore of fundamental interest in this field.

In Chapter 2 the dependence of the direct pQCD rates for charm production on structure functions, momentum scale Q^2 is reviewed, and we compare our results with a previous one [44]. Chapter 3 presents the results of part one of this thesis on the pre-equilibrium charm production. The important role of space-time and momentum correlations in suppressing that component of the charm production is emphasized. Chapter 4 contains the second part of this thesis. The dilepton spectra from open charm decay in $p + Au$ collision at 200 GeV/A are calculated and its sensitivity to the nuclear shadowing is quantitatively estimated. We pay particular attention to possible backgrounds of the dilepton spectra for the PHENIX detector geometry at RHIC. Discussion and summary are given at the end of each chapter. Chapter 5 presents an outlook of some open questions on charm productions.

Chapter 2

Initial Charm Production

In this chapter we will study how the direct pQCD rates of charm production depend on structure functions, momentum scale Q^2, and K-factor. We will then compare our results with results from the Parton Cascade Model [44].

2.1 Production Mechanisms

Heavy quark production in pp reactions was calculated long ago in [136] including both fusion and heavy flavor excitation processes in the leading order pQCD. It was proposed that the flavor excitation processes were dominant at high energies because a small Q^2 exchange can easily liberate any charm component in the nucleon while gluon fusion was suppressed because $Q^2 \geq 4M_c^2$. In the Parton Cascade Model [44], both mechanisms are incorporated to calculate s, c, b quark production in nuclear collisions. Results from this model suggested that the flavor excitation of the charm quark of nuclear structure functions would be the dominant source of charm production in nuclear collisions as well.

However, it is pointed out [137] that the original flavor excitation rates in [136] were too high in the $x_f \sim 0$ region due to neglected interference with other pQCD amplitudes of the same order. When all diagrams were added together, a large destructive interference was found to suppress the flavor excitation rates by powers of Λ/M_q, where $\Lambda \sim 300MeV$ is a typical QCD scale, and M_q is the heavy quark mass. The suppression factor appears in the process $g + c(\bar{c})$ where the charm is evolved from the structure functions using *perturbative* QCD, as also shown in [138].

We note that there is a possible non-perturbative charm component (intrinsic charm) in the nucleon. However, there are experimental constraints on the amount of this non-perturbative charm component [139, 140]. The total contribution of the intrinsic charm was shown in [141, 142] to be small (about 10%) in the midrapidity region where most of the charm is made. Although the contribution of the intrinsic charm component appears important at large x_f, its contribution to the total cross section is small and well within the uncertainties from other sources which we will discuss.

2.2 Cross Section

We therefore only include fusion processes for the parton level cross sections as in [62]. The cross sections are the following [136]:

$$d\sigma = dx_1 dx_2 f_1(x_1, Q^2) f_2(x_2, Q^2) \hat{\sigma}(\hat{s}) \ , \tag{2.1}$$

where $\hat{s} = x_1 x_2 s$.

Let $x_L = x_1 - x_2$, and $F = xf$ as the fractional-momentum parton distribution function, then

$$\begin{aligned} d\sigma &= d\hat{s}dx_L \frac{F_1(x_1,Q^2)F_2(x_2,Q^2)\hat{\sigma}(\hat{s})}{x_1x_2(x_1+x_2)s} \\ &= d\hat{s}dx_L \frac{F_1(x_1,Q^2)F_2(x_2,Q^2)\hat{\sigma}(\hat{s})}{\hat{s}\sqrt{x_L^2+4\hat{s}/s}} \quad , \end{aligned} \tag{2.2}$$

where

$$x_1 = (x_L + \sqrt{x_L^2+4\hat{s}/s})/2, x_2 = (-x_L + \sqrt{x_L^2+4\hat{s}/s})/2 \quad . \tag{2.3}$$

By assuming that Q^2 only depends on $\hat{s}$, we can explicitly obtain the pQCD differential cross sections for $a + b \to c\bar{c} + X$ as the following [136].

$$\hat{\sigma}_{q\bar{q}\to c\bar{c}} = \frac{8\pi\alpha_s^2(Q^2)}{27\hat{s}^2}(\hat{s}+2M_c^2)\ \chi \quad , \tag{2.4}$$

$$\hat{\sigma}_{gg\to c\bar{c}} = \frac{\pi\alpha_s^2(Q^2)}{3\hat{s}}\left[-(7+\frac{31M_c^2}{\hat{s}})\frac{1}{4}\chi + (1+\frac{4M_c^2}{\hat{s}}+\frac{M_c^4}{\hat{s}^2})\log\frac{1+\chi}{1-\chi}\right], \tag{2.5}$$

where $\chi = \sqrt{1-4M_c^2/\hat{s}}$.

2.3 Parton Structure Functions, Momentum Scale, and K-Factor

For the production in pp collisions, we use the light quark and gluon structure functions from Glück et al. [143] and Duke-Owens [144] for comparison. In Figure 2.1 we compare the parton structure functions from these two parameterizations together with MRSA [145] parameterization. The MRSA set

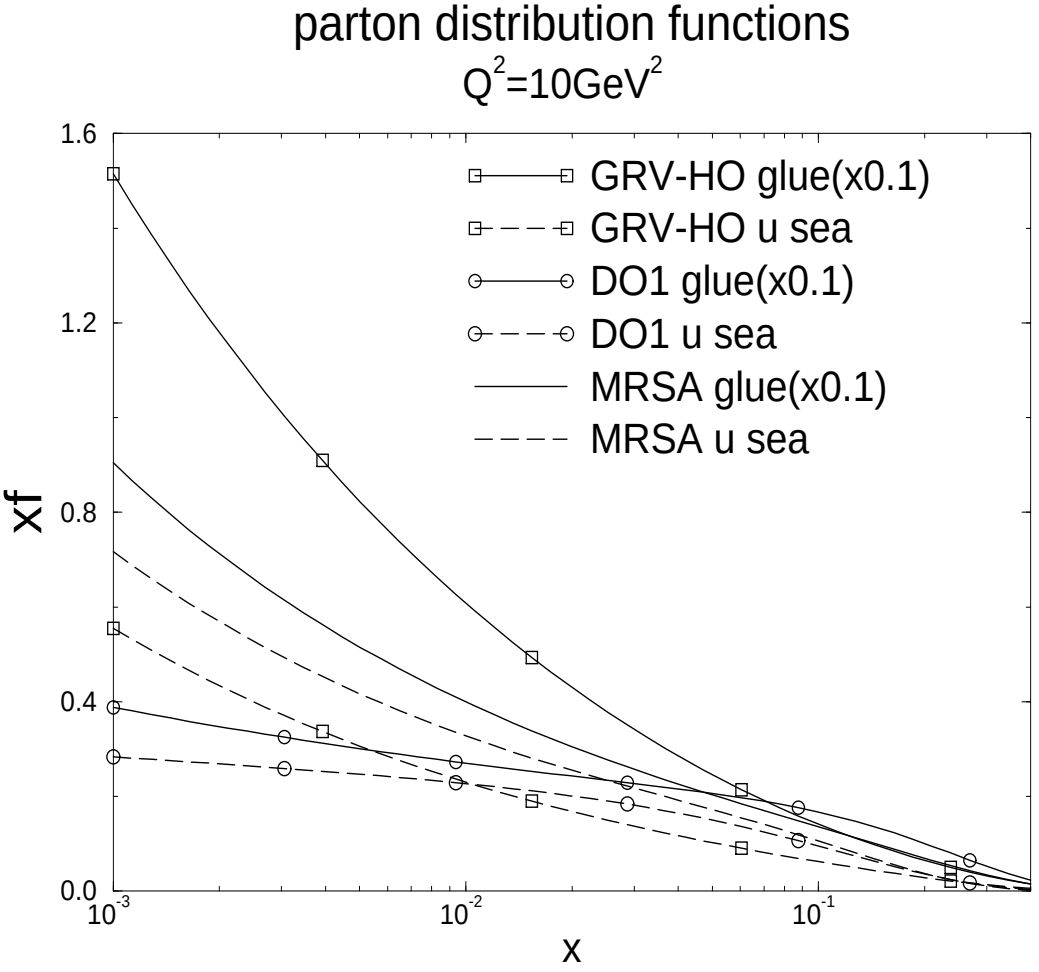

Figure 2.1: Parton momentum distribution functions for gluons and u sea-quarks as a function of Bjorken x for GRV-HO, DO1 and MRSA parametrizations.

Parton distribution functions	Λ(GeV)
GRV-LO set	0.25
GRV-HO set	0.20
Duke-Owens set 1(DO1)	0.20
Duke-Owens set 2(DO2)	0.40

Table 2.1: Lambda scales in different parton distribution functions

of parton distributions is very close to the latest parameterization CTEQ4M [146].

We consider the following two choices for the scale Q^2 in the coupling constant $\alpha_s(Q^2) = 12\pi/\left[(33-2n_f)\log(Q^2/\Lambda^2)\right]$. The Q^2 scale in the parton distribution functions is taken to be the same.

1. for $gg \to c\bar{c}, Q^2 = \hat{s}/2$; for $q\bar{q} \to c\bar{c}, Q^2 = \hat{s}$. ($Q^2$ choice-1)

2. for both $gg \to c\bar{c}$ & $q\bar{q} \to c\bar{c}, Q^2 = \hat{s}$. ($Q^2$ choice-2)

We take $n_f = 4$ for charm quark production and $n_f = 5$ for bottom quark production. The QCD scale Λ depends on the choice of parton distribution functions and is given in table 2.1.

To incorporate approximately the next-to-leading-order(NLO) corrections to the above rates, we multiply the leading order results by a K-factor. In general, the K-factor depends on the choice of parton distribution functions, the center of mass energy of the collision, and the type of the projectile and target particles. Calculations to order $O(\alpha_s^3)$ for the subprocesses were carried out [147, 148], and afterwards the calculations to order $O(\alpha_s^3)$ for $p+p$ collisions

were made [149, 150]. For DO1, $M_c = 1.5$ GeV, $Q^2 = 4M_c^2$, $P_{lab} = 100 - 1000$ GeV, the K-factor for $p + p$ collisions [149] was found to range from 2.85 to 4.1. There are other NLO calculations of charm production cross sections [151, 152], which reveal the dependence of the NLO K-factor on the transverse momentum and rapidity of the initially produced charm.

2.4 Comparison with Low-Energy Experimental *pp* Data

In Figure 2.2 we compare the so-calculated charm cross section to the limited data on inclusive $c\bar{c}$ production in pp collisions.

The NA34 data for σ_{charm} is taken directly from [153]. The values for the other data lines are computed from D-meson cross sections according to the argument in [154] by using the published experiment results [155, 156, 157, 158]. By assuming that $D_s/\bar{D}_s$ production accounts for 8% of the total cross section, hidden charm accounts for 1%, and $\Lambda_c\bar{D}/\bar{\Lambda}_c D$ production is smaller than $6.1\mu b$ at NA27, the conversion is done as the following:

$$\sigma(pp \to c\bar{c}X) \sim \frac{\sigma(\bar{D}/D)}{2(0.92 \pm 0.04)0.99}\left(1 + \frac{a(\leq 6.1)}{30.2 \pm 2.2}\right) \quad . \tag{2.6}$$

We then take $a = 6.1(0.)$ as the upper(lower) limit. Including the already-converted NA34/2 data, we have the following cross sections for $c\bar{c}$ in table 2.2.

Only statistical error is included in the above calculations. Earlier experiment results [159] show larger uncertainties among different experiments.

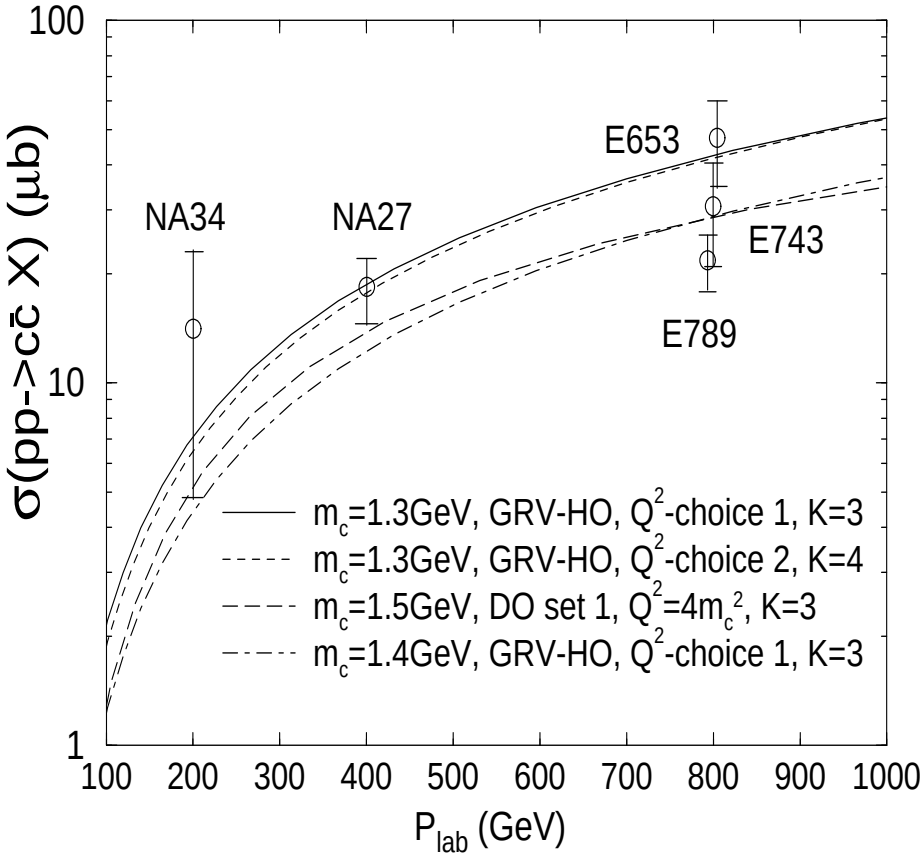

Figure 2.2: Cross sections for $pp \to c\bar{c}X$ as a function of P_{lab}.

Experiment	$P_{lab}(GeV)$	published original data(μb)	converted $\sigma_{c\bar{c}}(\mu b)$
NA27	400	$\Rightarrow \sigma(D/\bar{D}) = 30.2 \pm 2.2$	$14.7 - 22.1$
E743	800	$\Rightarrow \sigma(D/\bar{D}) = 48^{+10}_{-8}$	$21.0 - 40.5$
NA34/2	200		14.1 ± 9.3
E653	800	$\Rightarrow \sigma(D/\bar{D}) = 76 \pm 10$	$34.7 - 60.1$
E789	800	$\Rightarrow \sigma(D/\bar{D}) \sim 35.4 \pm 1.3$	$17.9 - 25.7$

Table 2.2: $c\bar{c}$ cross sections from low energy charmed meson data

In Figure 2.2, the solid line is our result with $M_c = 1.3$ GeV, $K = 3$, Q^2 choice-1 and GRV-HO set. As a consistency check, we also plot the long-dashed curve using the same parameters as in Figure 2.2 of [149] (i.e. DO1, $M_c = 1.5$GeV, $Q^2 = 4M_c^2$) using constant $K = 3$ for simplicity. Both the solid curve and the dashed curve fit the low energy data reasonably well, so we use these two parametrizations for the following high energy calculations in this chapter. Comparison of the solid and dot-dashed curves shows the strong dependence on the assumed charm quark mass for the GRV-HO set. Comparing the solid and dashed curve we see that different choices for the Q^2 scale can be compensated for by shifts in the K factor. These results, together with the large uncertainty of data, emphasize the need to measure pp and pA reactions in order to control uncertainties in the initial charm production rate, so that charm productions in AA can be properly calculated.

As a further check of the parameters we compare charmed hadron x_f results in Figure 2.3 with 400 GeV pp data [155]. The solid curve represents

the result $d\sigma/dx_f$ using the first parameterization. The dashed curve represents the result using the second parameterization. Both curves assume a δ function charm fragmentation function. The realistic fragmentation function used in [141] lowers the curves slightly and reveals the true high-x_f intrinsic charm component. In Figure 2.4 we compare $b\bar{b}$ production. Here we take $M_b = 4.75$ GeV as in [150], with $K = 3, n_f = 5$. The data point at $\sqrt{S} = 630$GeV is from [160]: $\sigma(p\bar{p} \to b + X) = 19.3 \pm 7(exp.) \pm 9(th.)\mu b$, and only the experimental error is indicated in Figure 2.4. The dashed cross at $\sqrt{S} = 1.8$ Tev is obtained indirectly from [150], and the error bar is only illustrative. At $\sqrt{S} = 1.8TeV$, our value is $41.8\mu b \times K = 125\mu b$. This is significantly larger than found in [150].

2.5 The A-scaling of Charm Productions

The dependence of cross sections of charm productions on atomic number A in $p + A$ collisions is usually parameterized as $\sigma_D^{pA} = \sigma_D^{pp} A^{\alpha}$. Earlier experiments gave $\alpha \simeq 0.76$ [161]. However, those experiments did not explicitly reconstruct D mesons and had lower statistics. Later experiments [162, 158] reconstructed D mesons and found $\alpha = 1.02 \pm 0.03 \pm 0.02$ [158], which is consistent with $\alpha = 1.$ from the Glauber geometry. We note that the value $\alpha = 0.76$ is taken from low energy experiments, where energy conservation suppresses the contribution from multiple collisions. At high energies, QCD factorization implies that $\alpha = 1$ for $p + A$ scaling is the appropriate scaling modulo small nuclear shadowing effects. The nuclear shadowing effect

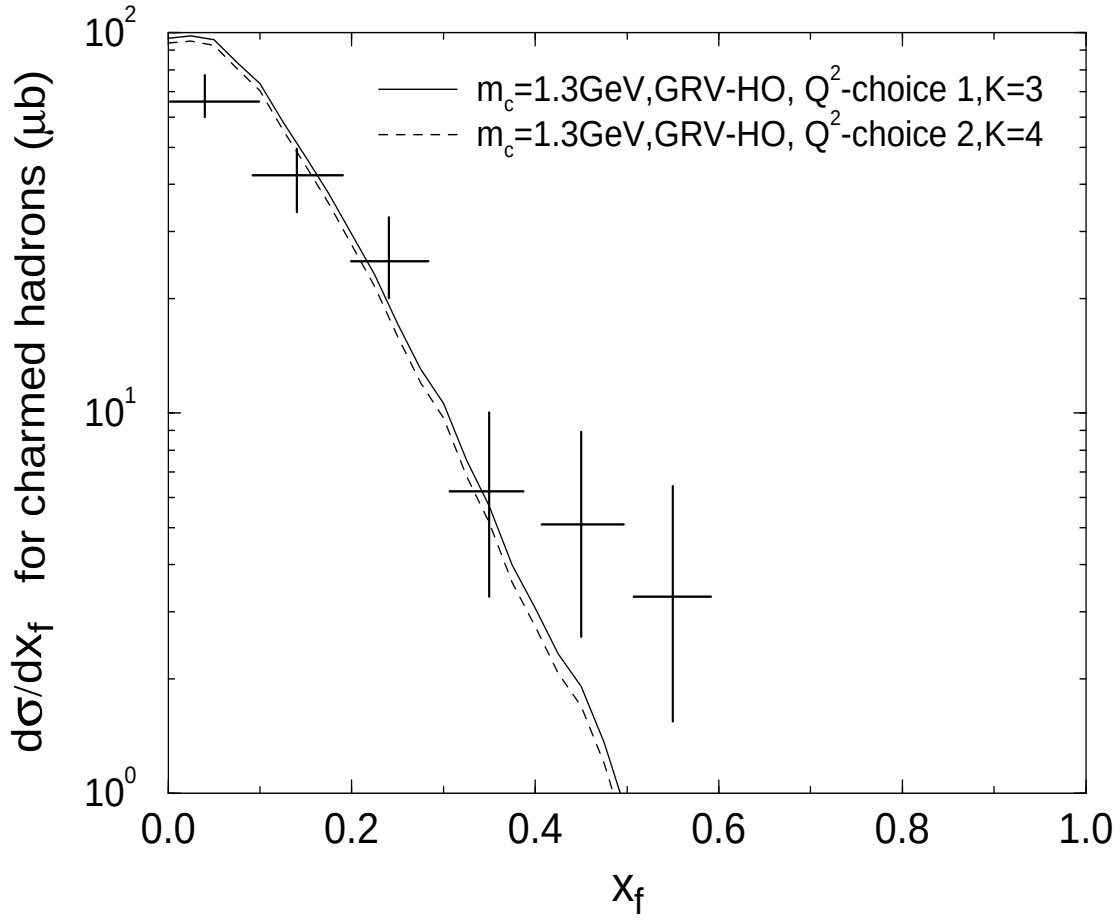

Figure 2.3: The production of charmed hadrons as a function of x_f for pp collisions at $P_{lab} = 400$ GeV.

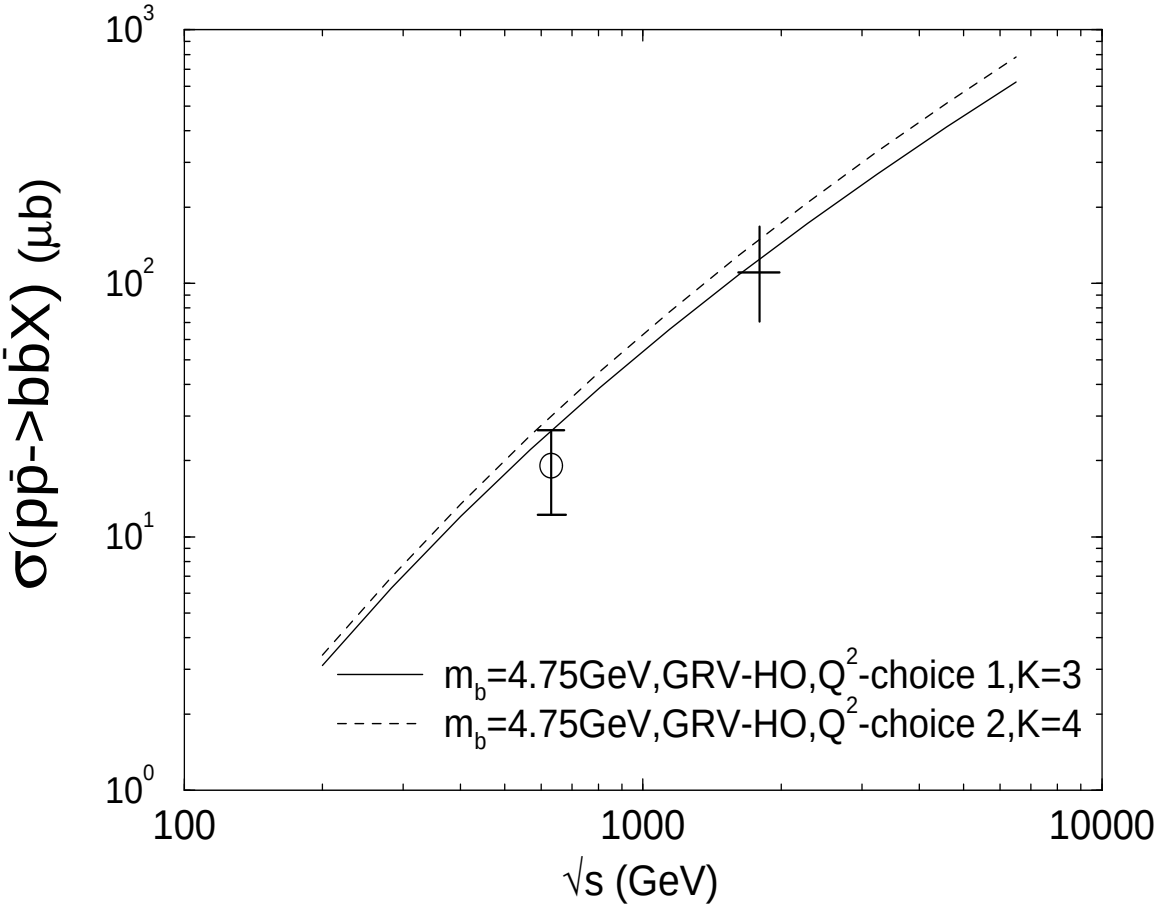

Figure 2.4: Cross sections for $p\bar{p} \to b\bar{b} + X$ vs $\sqrt{S}$.

on the A-scaling was estimated by Qiu [163], and he found that the nuclear shadowing could only lead to a small reduction in α ($\alpha \geq 0.96$) in low energy experiments [161]. In the sections for initial charm productions, we neglect the nuclear shadowing since it is a minor effect compared with effects in our focus.

2.6 Comparison with Results from Parton Cascade Model

Now we compare our results for the rapidity density of produced $c\bar{c}$ pairs at $Y = 0$ with results of [44]. Figure 2.5 shows the energy dependence in the range between RHIC and LHC ($\sqrt{s} = 200 - 6300$ AGeV) for $Au + Au$ collisions.

The scaling from pp results to AA is

$$\left(\frac{dN}{dY}\right)^{AA}_{Y=0} = A^{\alpha+1/3}\left(\frac{d\sigma}{dY}\right)^{pp}_{Y=0} / \sigma^{pp}_{inelastic} \quad , \tag{2.7}$$

where $\sigma^{pp}_{inelastic}$ is taken from [164], which is about $40.8mb$ at RHIC energy and $73.5mb$ at LHC energy. Glauber geometry for central high $A + A$ collisions gives $\alpha = 1$.

In Figure 2.5 the solid curve is the result we obtained using the same parameters as for the solid curve in Figure 2.2. The parameterization for the dashed curve in Figure 2.2 gives a curve higher than the solid curve by 15% to 30%. The four long-dashed curves, curve1 to curve4, are all from PCM calculations [44]. The top curve4 is the parton cascade model result

for the so-called QGP formation case, including both the fusion and the flavor excitation processes. That curve is much higher than our solid curve because it includes the contribution from flavor excitation processes. Curve3, the curve with solid squares, shows the contribution to curve4 from fusion processes only (processes (1) and (2) in the notation of [44]), and curve3 is very close to our results. The bottom curve1 is the parton model result extrapolated to AA from pp using the $A^{0.76}$ scaling measured at much lower energies. It is lower than our solid curve by a factor of 12 at the RHIC energy to 5 at the LHC energy. The main source of this difference is from the A-dependence of $p+A$ cross sections. The parton cascade model [44] used an A^{α} scaling with $\alpha = 0.76$ [161] instead of the value $\alpha = 1$ we use from Glauber geometry. To demonstrate the effect in different A^{α} scalings, we plot curve2, which is the parton model result scaled from pp to AA by $A^{4/3}$, and it is close to our results. As shown by the two arrows, curve4 becomes curve3 when the coherent cancellation of flavor excitation processes is considered, and curve1 becomes curve2 when the high energy scaling is used. Therefore, the factor ~ 50 enhancement of charm production suggested in [44] comparing curve1 with curve4 for charm production at $RHIC$ is a consequence of the inclusion of incoherent flavor excitation processes and the extrapolation from pp to AA via low energy scaling. The net dynamical enhancement in the PCM should be obtained by comparing curve2 with curve3. In that case Figure 2.5 leads to the expectation that the pre-equilibrium charm production should be comparable to the initial fusion rate. This removes the bulk of the

discrepancy between [62] and [44].

2.7 Summary

We calculated initial charm production in nuclear collisions. We demonstrated the sensitive dependence on the choice of structure functions, the Q^2 scale, and the K-factor. The parameters were fixed by fitting the limited available experimental data at lower energies. We emphasized the need for new measurements of pp and pA charm production to reduce the present large theoretical uncertainties. We argued that the copious charm production predicted in [44] was mainly due to the neglect of the coherent suppression of flavor excitation processes and the low energy pp to AA scaling. Our calculated initial charm yields are close to those computed in [62] and to the curve 2 in Figure 2.5 from [44].

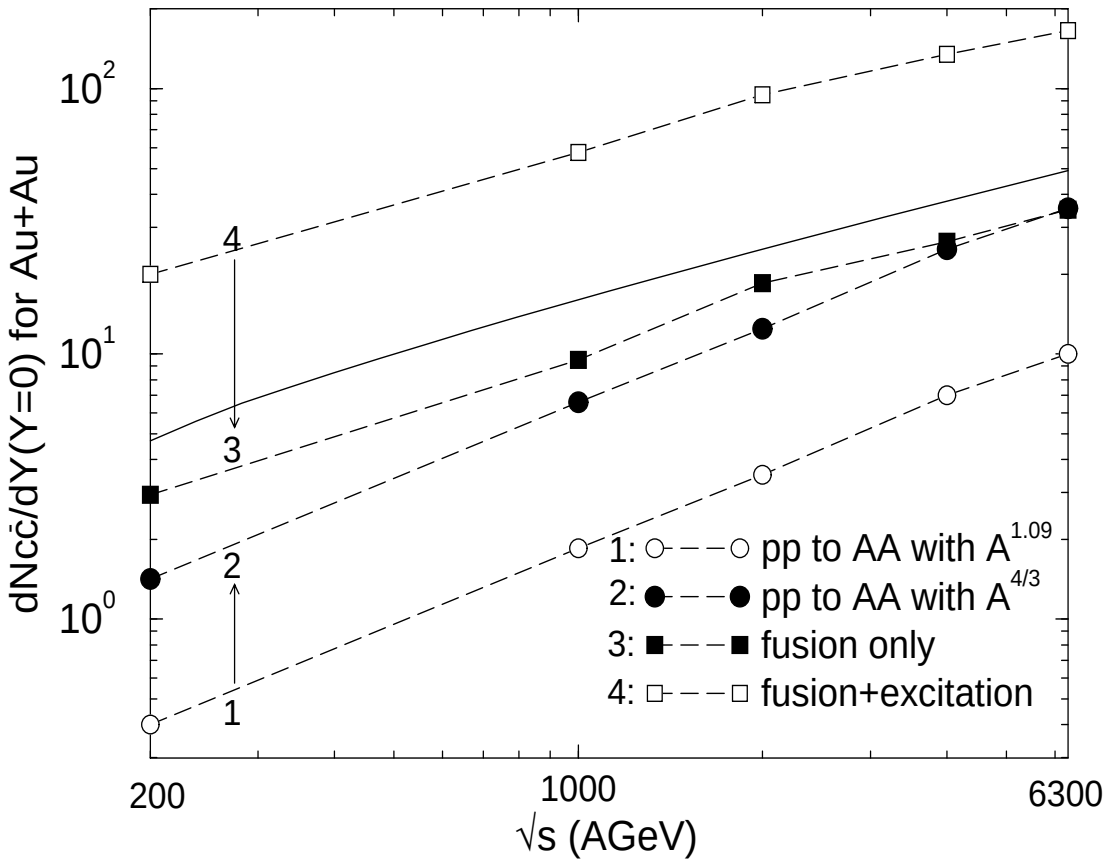

Figure 2.5: Comparison with Parton Cascade Model results on $(dN_{c\bar{c}}/dY)_{Y=0}$: the rapidity density of charm and anti-charm pairs for $Au + Au$ collisions as a function of $\sqrt{S}/A$.

Chapter 3

Pre-equilibrium Charm Production

In this chapter we consider the pre-equilibrium contribution to the charm yield in $A + A$ collisions. It is produced through final state interactions between partons in the dense minijet plasma. Here we only calculate the dominant contribution from minijet gluon fusion.

3.1 Spectrum of Minijets

The spectrum of minijet gluons in leading-order follows from [165]

$$\begin{aligned} \frac{d\hat{\sigma}}{d\hat{t}}_{gg\to gg} &= \frac{9}{2}\frac{\pi\alpha_s^2}{\hat{s}^2}\left[3 - \frac{\hat{u}\hat{t}}{\hat{s}^2} - \frac{\hat{u}\hat{s}}{\hat{t}^2} - \frac{\hat{s}\hat{t}}{\hat{u}^2}\right] \ , \\ \frac{d\hat{\sigma}}{d\hat{t}}_{gq\to gq} &= \frac{\pi\alpha_s^2}{\hat{s}^2}\left[-\frac{4}{9}\frac{\hat{u}^2+\hat{s}^2}{\hat{u}\hat{s}} + \frac{\hat{u}^2+\hat{s}^2}{\hat{t}^2}\right] \ . \end{aligned} \tag{3.1}$$

The term minijets refers to unresolved jets at a scale $p_\perp > p_{\perp\,cut}$. The inclusive cross section to produce minijets is given by

$$\frac{d\sigma}{dydp_\perp^2} = \int dy_3 x_1 f_1 x_2 f_2 \frac{d\hat{\sigma}}{d\hat{t}}(1+2\to 3+4) \ , \tag{3.2}$$

where f_1 is the incident parton distribution evaluated at $x_1 = p_\perp(e^y + e^{y_3})/\sqrt{s}$ at a scale $Q^2 = {p_\perp}^2$. The light-cone coordinates of the initial and final partons are:

$$\begin{aligned} p_1 &= \left[2x_1 p_0, 0, \vec{0}\right] \quad , \\ p_2 &= \left[0, 2x_2 p_0, \vec{0}\right] \quad , \\ p_3 &= \left[m_\perp e^{y_3}, m_\perp e^{-y_3}, -\vec{p_\perp}\right] \quad . \end{aligned} \tag{3.3}$$

The observed parton has momentum

$$p = \left[m_\perp e^{y}, m_\perp e^{-y}, \vec{p_\perp}\right] \quad . \tag{3.4}$$

The subprocess Mandelstam variables are $\hat{s}, \hat{t}$, and $\hat{u}$. For the calculation of minijet gluon fusion process in the following Chapter 3.2, we choose $Q^2 = \hat{s}$. As in [62], we use DO1 as the proton structure functions and $K = 2$, $M_c = 1.5$GeV for the minijet production. The nuclear shadowing effect is taken from [166]. In Figure 3.1 we show the resulting transverse momentum distribution of mid-rapidity minijet gluons at $\sqrt{s} = 200$ AGeV in open circles. We call this distribution the hard distribution since it only includes the hard gluons with $p_\perp > p_{\perp cut} = 2$GeV . The solid line in Figure 3.1 is the output of the Monte Carlo calculation via the HIJING model [70] that includes initial and final state radiation, and therefore fills the soft gluon region. The dashed line is our fit $0.06e^{-1.25p_\perp}$, which is discussed below. In Figure 3.2 we show the rapidity distribution of minijet gluons. The circles represent our result from the initial production. The dashed line represents the fit $\cos\left[\frac{\pi(\frac{y}{3.7})^{1.8}}{2}\right]$, where dN/dy scale is arbitrary.

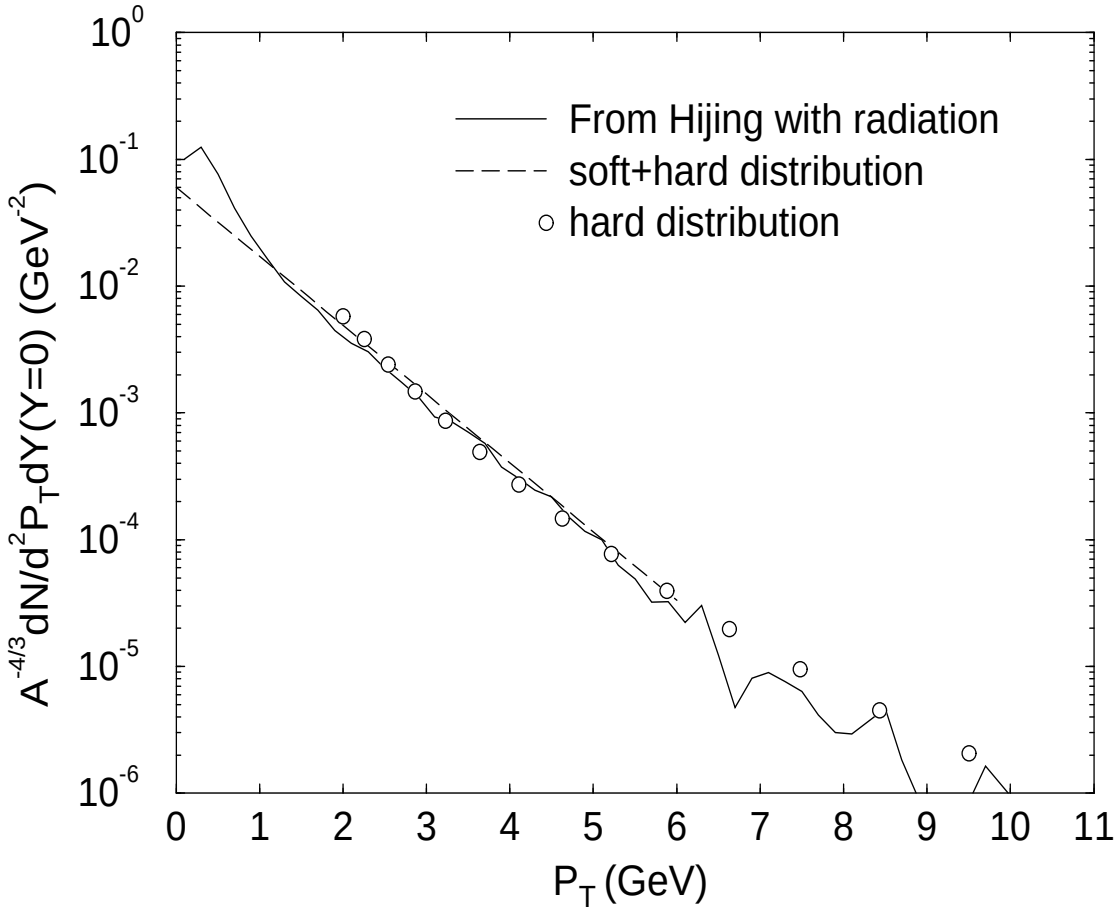

Figure 3.1: The minijet gluon $p_\perp$ distribution $A^{-4/3}\left(dN/dydp_\perp^{\vec{}}\right)_{y=0}$.

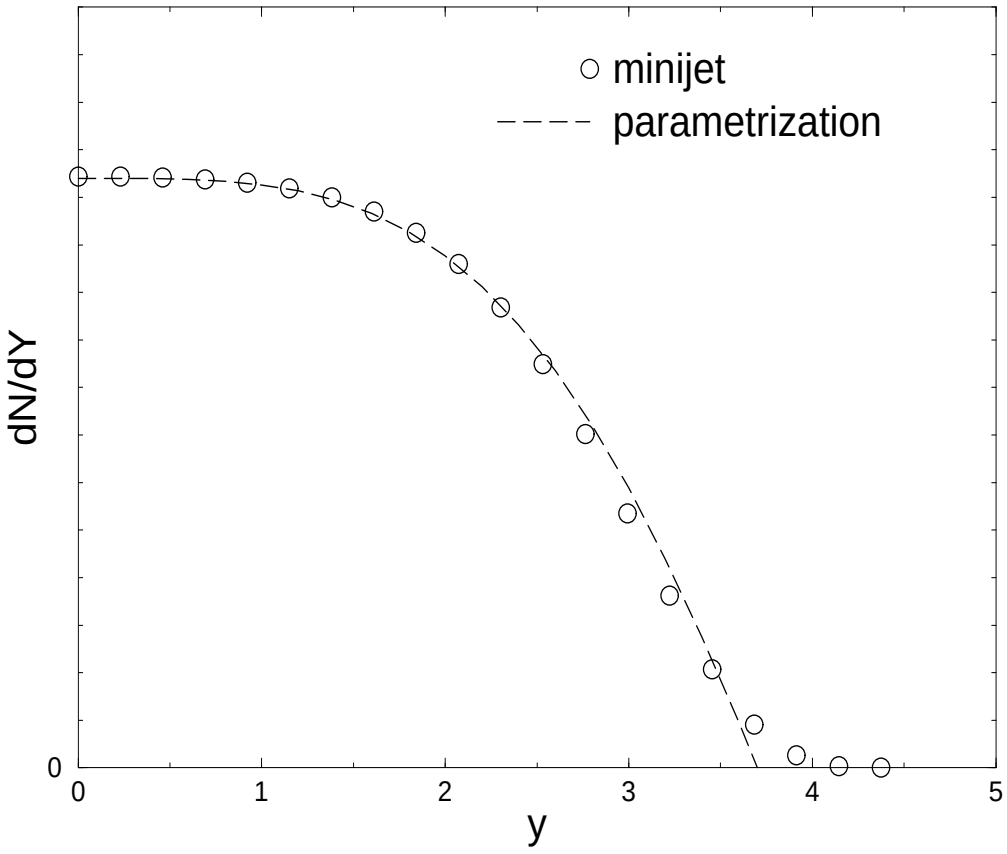

Figure 3.2: The minijet gluon rapidity distribution dN/dy.

For convenience we have parameterized the minijet spectrum (both soft and hard gluons) from the Monte Carlo calculation as the following:

$$\frac{dN}{dy d\vec{p_\perp}} \equiv g(p_\perp)\rho(y)A^{4/3} = 0.06 e^{-1.25 p_\perp} \cos\left[\frac{\pi(\frac{y}{3.7})^{1.8}}{2}\right] A^{4/3} \quad , \quad (3.5)$$
$$\text{with } |y| \leq 3.7 \ .$$

In the following, we call this parameterized distribution the soft+hard distribution. The soft+hard, hard, and Monte Carlo distributions are very close to each other in the semi-hard $p_\perp > 2$ GeV region at $y = 0$, as seen in Figure 3.1. The parameterized distribution falls underneath the Monte Carlo result in the region $p_\perp < 1$ GeV. However, the soft component is strongly model-dependent as it requires the furthest extrapolation from the pQCD hard domain. The Hijing yield in that region is due to initial and final state radiation. Other contributions in this soft domain from coherent strings are possible [38]. While most of the following results are obtained with the simple parameterization above, we will check the sensitivity to variations of the soft component as well. We also note that at bigger rapidity the $p_\perp$ spectrum falls more rapidly. The above parameterization does not include that property. However, this property only lowers the high $p_\perp$ tail, and only slightly changes the low $p_\perp$ part and the total number of the pre-equilibrium charm.

3.2 Two Extreme η - y Correlations

In ideal Bjorken dynamics, the space-time rapidity

$$\eta = 1/2 \log[(t+z)/(t-z)] \quad , \quad (3.6)$$

and the true momentum rapidity

$$y = 1/2 \log[(E + p_z)/(E - p_z)] \tag{3.7}$$

are assumed to be perfectly correlated. This is referred to as the inside-outside picture, and the phase-space distribution function in Bjorken correlation case has the form

$$\begin{aligned} F(\vec{x}, \vec{p}, t)_{Bj} &= \frac{(2\pi)^3}{\tau \pi R_A^2 p_\perp} \frac{dN}{dy d\vec{p_\perp}} \\ &\quad \times \delta(\eta - y)\Theta(\tau - \tau_i)\Theta(\tau_f - \tau) \ , \end{aligned} \tag{3.8}$$

where $\tau_i = 0.1 fm/c$ is the minijet formation time. $\tau_f \approx 1.7 fm/c$ as the proper time when the energy density of the pre-equilibrium minijets falls by an order of magnitude to $\sim 2GeV/fm^3$ due to rapid longitudinal expansion, and that is when we terminate the pre-equilibrium stage.

The phase space distribution is normalized such that

$$\int \frac{F(\vec{x}, \vec{p}, t)_{Bj} d^3x}{(2\pi)^3} = \frac{d^3N}{d^3p} = \frac{1}{E} \frac{dN}{dy d\vec{p_\perp}} \ , \tag{3.9}$$

In this chapter we study the pre-equilibrium charm production at $y = 0$ [62]:

$$\begin{aligned} \left(E \frac{d^3N}{d^3p} \right)_{y=0} &= \int d^4x \int \frac{1}{32(2\pi)^8} \frac{d^3p_1 d^3p_2 d^3p'}{\omega_1 \omega_2 E'} \\ &\quad \times F(\vec{x}, \vec{p_1}, t) \ F(\vec{x}, \vec{p_2}, t) \ |M|^2 \ \delta^{(4)} \left(\sum P^\mu \right) \ . \end{aligned} \tag{3.10}$$

Denoting

$$\begin{aligned} dN/dy d\vec{p_\perp} &\equiv g(y, p_\perp) \ , \\ \vec{p_{\perp 1}} &= p_{\perp 1}(\cos\phi_1, \sin\phi_1, 0) \ , \end{aligned} \tag{3.11}$$

the ideal $\eta - y$ correlation leads to

$$\left(E\frac{d^3N}{d^3p}\right)_{y=0} = \int_{\tau_i}^{\tau_f} \frac{d\tau}{32(2\pi)^2\tau\pi R_A^2} \times \int d\eta dp_{\perp 1} dp_{\perp 2} d\phi_1 d\phi_2 \frac{g(\eta, p_{\perp 1})g(\eta, p_{\perp 2})\delta(\sum E)|M|^2}{E'}$$

$$= \frac{\ln(\tau_f/\tau_i)}{32(2\pi)^2\pi R_A^2} \int d\eta dp_{\perp 2} d\phi_1 d\phi_2 \times \frac{g(\eta, p_{\perp 1,0})g(\eta, p_{\perp 2})|M|^2}{p_{\perp 2}\left[1-\cos(\phi_1-\phi_2)\right] - (E\cosh\eta - p\cos\phi_1)} \quad . \quad (3.12)$$

In deriving the above, we have used kinematic relations

$$E' = (p_{\perp 1} + p_{\perp 2})\cosh\eta - E \quad , \quad (3.13)$$

$$\frac{\delta(\sum E)}{E'} = \frac{\delta(p_{\perp 1} - p_{\perp 1,0})}{p_{\perp 2}\left[1-\cos(\phi_1-\phi_2)\right] - (E\cosh\eta - p\cos\phi_1)} \quad , \quad (3.14)$$

$$p_{\perp 1,0} = \frac{p_{\perp 2}(E\cosh\eta - p\cos\phi_2)}{p_{\perp 2}\left[1-\cos(\phi_1-\phi_2)\right] - (E\cosh\eta - p\cos\phi_1)} \quad . \quad (3.15)$$

In Figure 3.3 we show the numerical results of the above integral in equation (3.12).

The solid line is the $p_\perp$-distribution for the initial charm production from Chapter 2. The curve labeled with solid diamonds represents the pre-equilibrium contribution including both the soft ($p_\perp < 2$ GeV) and hard ($p_\perp > 2$ GeV) components of the minijet gluons. The curve labeled with hollow diamonds represents the pre-equilibrium contribution including only the hard component. We see that the pre-equilibrium contribution in this strongly correlated case is totally negligible. This result is similar to the thermal charm production contribution calculated in [62], except that, in

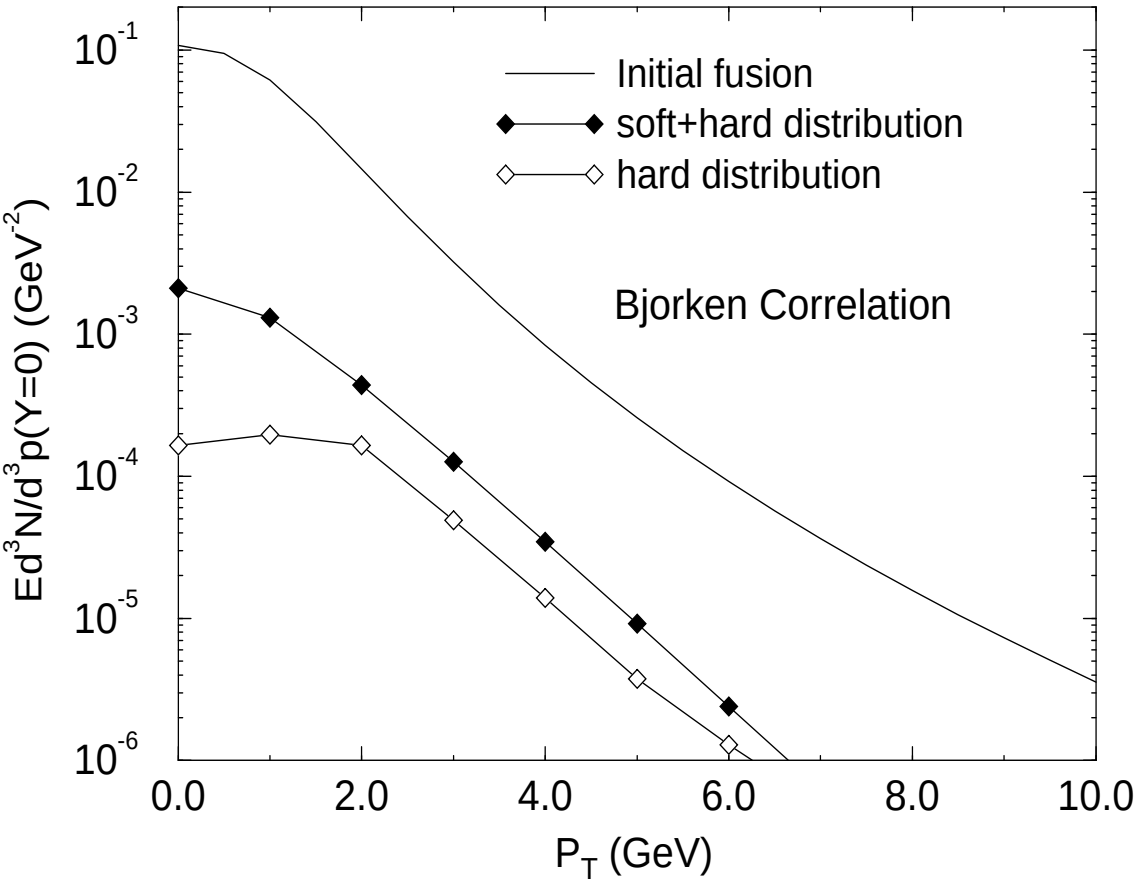

Figure 3.3: The distribution $(Ed^3N/d^3p)_{y=0}$ of charm quark production as a function of $p_\perp$ using $\delta(\eta - y)$-correlation .

our case, the curve extends to higher $p_\perp$ because of the broader initial mini-jet distribution in $p_\perp$.

Another extreme case, opposite to the ideal Bjorken picture, was considered in [62]. In that uncorrelated $\eta - y$ case, the gluon distribution was assumed to be completely uncorrelated as in an ideal thermal fireball. This assumption leads to

$$F(\vec{x},\vec{p},t)_{Fb} = \frac{(2\pi)^3}{p}\frac{1}{V}\frac{dN}{dydp_\perp^{\rightarrow}} \quad . \tag{3.16}$$

If one assumes a fixed volume $V = \tau_i \pi R_A^2$, then $\int dt \sim \tau_f - \tau_i$, and

$$\int \frac{d^4x}{V^2} \sim \frac{1}{\pi R_A^2}\frac{\tau_f}{\tau_i} \qquad \text{as in [62].} \tag{3.17}$$

Then from equation (3.10), we have

$$\left(E\frac{d^3N}{d^3p}\right)_{y=0} = \frac{I(p)}{32(2\pi)^2}\int\frac{d^4x}{V^2} = \frac{\tau_f/\tau_i}{32(2\pi)^2\pi R_A^2}I(p) \quad , \tag{3.18}$$

where

$$I(p) = \int \frac{dy_1 dy_2 dp_{\perp 2} d\phi_1 d\phi_2}{\cosh y_1 \cosh y_2}\frac{g(y_1,p_{\perp 1,0})g(y_2,p_{\perp 2})|M|^2}{D(y_1,y_2,p_{\perp 2},\phi_1,\phi_2,p)} \tag{3.19}$$

$$\frac{\delta\left(\sum E\right)}{E'} = \frac{\delta(p_{\perp 1} - p_{\perp 1,0})}{D(y_1,y_2,p_{\perp 2},\phi_1,\phi_2,p)} \quad , \tag{3.20}$$

$$p_{\perp 1,0} = \frac{p_{\perp 2}(E\cosh y_2 - p\cos\phi_2)}{D(y_1,y_2,p_{\perp 2},\phi_1,\phi_2,p)} \quad , \tag{3.21}$$

$$\begin{aligned} D(y_1,y_2,p_{\perp 2},\phi_1,\phi_2,p) = {} & p_{\perp 2}\left[\cosh(y_1-y_2) - \cos(\phi_1-\phi_2)\right] \\ & -(E\cosh y_1 - p\cos\phi_1) \quad . \end{aligned} \tag{3.22}$$

In Figure 3.4 we show the pre-equilibrium charm production for this uncorrelated case. The solid curve represents the initial charm production. The

curve labeled with solid circles represents the pre-equilibrium contribution including both the soft ($p_\perp < 2$ GeV) and hard ($p_\perp > 2$ GeV) components. It is much larger than the Bjorken-correlation case, and is comparable with the initial charm yield, as shown in Figure 3.4. This is similar to the result in [62] in which the pre-equilibrium charm production has almost the same magnitude and $p_\perp$-shape as the initial charm. The curve labeled with hollow circles represents the pre-equilibrium contribution including only the hard component.

3.3 Minimally-correlated $\eta - y$

From the above results we conclude that the pre-equilibrium charm production is very sensitive to the $\eta - y$ correlation of the minijets. We consider here the simplest source of $\eta - y$ correlations resulting from the minimal geometrical spread in initial production points required by the uncertainty principle. This type of correlations are included in the parton cascade model and discussed in [167]. The phase space distribution function including such minimal correlation has the form

$$\begin{aligned} F(\vec{x},\vec{p},t)_{Min} &= \mathcal{N}\int \frac{dN}{dy d\vec{p_\perp}} \frac{\theta(\tau_{max} - \frac{t}{\cosh y})}{1+(\frac{t_f(p)}{\Delta t})^2} \\ &\quad \times \rho_0(\vec{x_0},t_0)\delta(\vec{x}-\vec{x_0}-\vec{v}\Delta t) d^3x_0 dt_0 \ . \end{aligned} \tag{3.23}$$

The integration is over the space-time coordinates $(\vec{x}_0, t_0)$ of the production points of the gluons. These points are distributed according to a normalized density $\rho_0(\vec{x}_0, t_0)$. The delta function arises to take into account the free

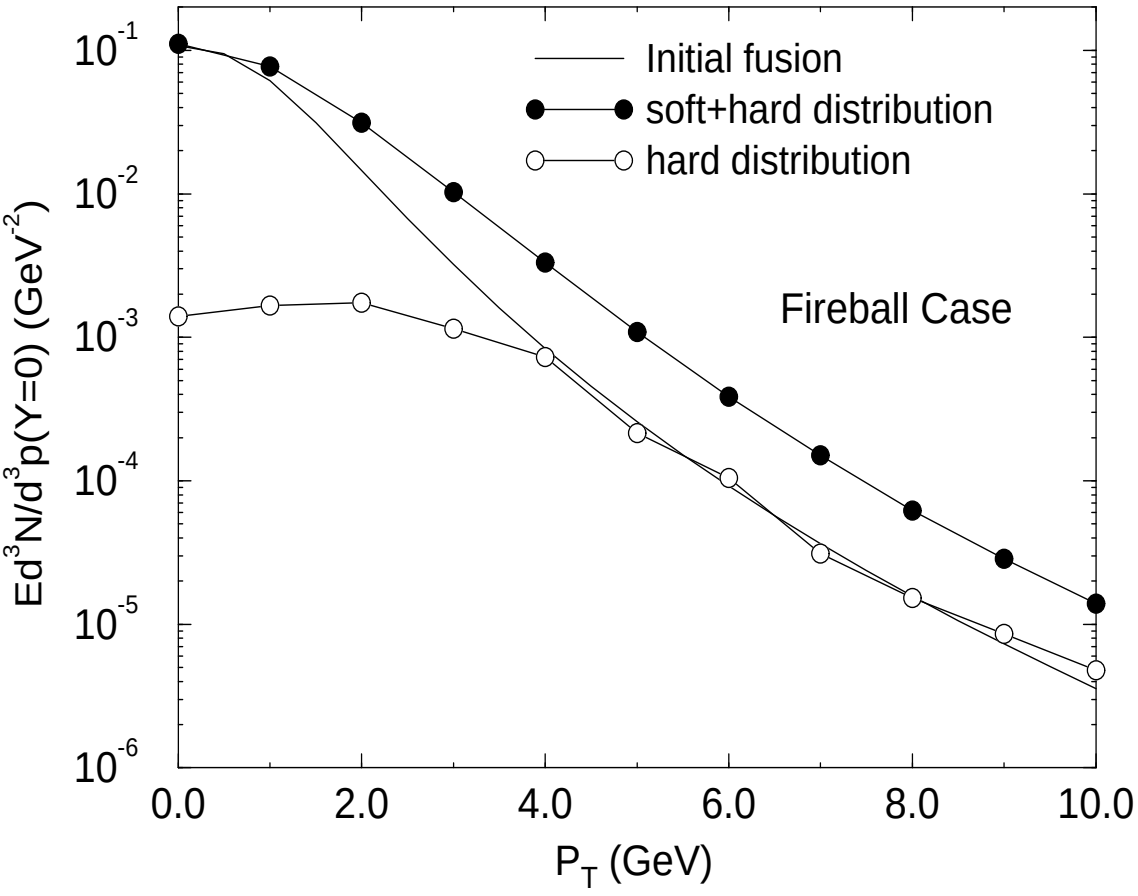

Figure 3.4: The distribution $(Ed^3N/d^3p)_{y=0}$ of charm quark production as a function of $p_\perp$ for the non-correlation case.

streaming of the partons from the production point, with velocity $\vec{v} = \vec{p}/E$, where $E = p_\perp \cosh y$ and $p_z = p_\perp \sinh y$. The theta function defines what we mean by pre-equilibrium. The proper time when the pre-equilibrium fusion is terminated is τ_{max}, which is determined below in Figure 3.6. The theta function insures that only those gluons with proper time less than τ_{max} contribute to pre-equilibrium charm productions.

The formation physics is included via the Lorentzian formation factor [168]

$$[1 + (t_f(p)/\Delta t)^2]^{-1} \quad , \tag{3.24}$$

where $\Delta t = t - t_0$ is the elapsed time, and the formation time is given by

$$t_f(p) \simeq \cosh y \frac{0.2\text{GeV}}{p_\perp}(fm) \quad , \tag{3.25}$$

We note that, at the early time, the above formation factor more accurately describes the interference phenomena suppressing production than the conventionally assumed factor

$$\theta[\Delta t - t_f(p)] \quad , \tag{3.26}$$

We assume

$$\int \rho_0(\vec{x_0}, t_0) d^3x_0 dt_0 = 1 \quad . \tag{3.27}$$

In this case the normalization factor is

$$\mathcal{N} = \frac{(2\pi)^3}{E} \quad , \tag{3.28}$$

so that

$$\lim_{t\to\infty}\frac{1}{(2\pi)^3}\int F(\vec{x},\vec{p},t)_{Min}d^3x=\frac{d^3N}{d^3p}\quad . \tag{3.29}$$

As discussed in [167], the production points are spread along the beam axis according to the uncertainty principle by an amount $\delta z\equiv d\sim\hbar/p_\perp$, since the dominant parton interaction leading to a $y=0$ parton with final $p_\perp$ has an initial longitudinal momentum $xP_0\sim p_\perp$. We take as a particular model

$$d=\frac{0.2}{p_\perp}(fm)\quad . \tag{3.30}$$

Clearly this is only a rough guess, but it allows us at least to investigate the sensitivity of the results to a particular $\eta-y$ correlation that results from this spatial spreading of the production points. We emphasize that it is precisely the uncertainty of the initial space-time formation physics that leads us to investigate the possibility of open charm production as an experimental probe of this physics.

Given the above assumption we take

$$\rho_0(\vec{x_0},t_0)=\frac{1}{\pi R_A^2}\delta(t_0)\frac{e^{-z_0^2/(2d^2)}}{\sqrt{2\pi}d}\quad , \tag{3.31}$$

where d is the mean spread for gluons depending on $p_\perp$ from above. This distribution only spreads out the production points along the beam axis. A more realistic treatment would also include a spread in the time coordinate.

Neglecting transverse expansion, we obtain finally

$$\begin{aligned}F(\vec{x},\vec{p},t)_{Min} &= \frac{(2\pi)^3}{\sqrt{2\pi}\pi R_A^2}\frac{p_\perp}{0.2}e^{-(z-\tanh y\ t)^2(\frac{p_\perp}{0.2})^2/2}\\ &\quad\times\frac{1}{p}\frac{dN}{dy\ d\vec{p_\perp}}\frac{\theta(\tau_{max}-\frac{t}{\cosh y})}{1+(\frac{0.2\cosh y}{p_\perp t})^2}\quad .\end{aligned} \tag{3.32}$$

Denote

$$\begin{aligned} a_1 &= \tanh y_1 \quad , \\ a_2 &= \tanh y_2 \quad , \\ b_1 &= (\frac{p_{\perp 1,0}}{0.2})^2/2 \quad , \\ b_2 &= (\frac{p_{\perp 2}}{0.2})^2/2 \quad , \end{aligned} \tag{3.33}$$

then after integration over z, we have the final expression as the following:

$$\begin{aligned} \left(E\frac{d^3N}{d^3p}\right)_{y=0} &= \frac{\sqrt{\pi}}{16(2\pi)^4 R_A^2}\int dy_2 dy_1 dp_{\perp 2} d\phi_2 d\phi_1 \\ &\times \frac{p_{\perp 1,0}\frac{p_{\perp 1,0}}{0.2}\frac{p_{\perp 2}}{0.2}|M|^2}{p_{\perp 2}\cosh y_1 \cosh y_2 (E\cosh y_2 - p\cos\phi_2)} \frac{g(y_1, p_{\perp 1,0})g(y_2, p_{\perp 2})}{\sqrt{b_1+b_2}} \\ &\times \int_0^{t_f} dt \frac{e^{\frac{-(a_1-a_2)^2 t^2}{1/b_1+1/b_2}}}{\left[1+(\frac{0.2\cosh y_1}{p_{\perp 1,0}t})^2\right]\left[1+(\frac{0.2\cosh y_2}{p_{\perp 2}t})^2\right]} \quad . \end{aligned} \tag{3.34}$$

In the above

$$t_f = \tau_{max}\min(\cosh y_1, \cosh y_2) \quad , \tag{3.35}$$

and $p_{\perp 1,0}$ is the same as in equation (3.22). Note that by using the unit GeV for momentum and unit fm for time, the expression $\left(E\frac{d^3N}{d^3p}\right)_{y=0}$ in equations (3.12), (3.18), and (3.34) has the dimension $GeV^{-4}fm^{-2}$. We require a factor $(\hbar c)^2 \sim (0.2GeVfm)^2$ to convert it to the dimension GeV^{-2}, which we have used in Figure 3.3, Figure 3.4,Figure 3.5 and Figure 3.7.

The numerical results of the above equation 3.34 are shown in Figure 3.5. The curve labeled with solid squares includes both components while that labeled with hollow squares includes only the fusion of hard gluons. The curve

labeled with diamonds represents the contribution from fusion of soft gluons both with $p_\perp < 2$GeV. This shows that the pre-equilibrium contribution comes mainly from the fusion of soft and hard gluons.

In Figure 3.6 the energy density at $z = 0$ as a function of proper time is shown assuming minimal correlation and Lorentzian formation probability. The solid curve includes both soft and hard components while the dashed curve is calculated using the hard distribution and includes only the hard component. The energy density increases and reaches maximum at the time about $0.1 fm/c$, then the energy density decreases linearly to $\sim 2GeV/fm^3$ at $\sim 1.7 fm/c$ for soft+hard distribution. We choose the above time as the cutoff τ_{max}.

3.4 Why Is the Pre-equilibrium Charm Yield So Small?: An Estimate

To understand why the pre-equilibrium charm yield is so small compared to the initial yield as found through tedious numerical calculations in the previous chapter, we consider here the calculation of the total number of pre-equilibrium charm pairs. The expression for that number is given by

$$N = \frac{(\hbar c)^2}{4(2\pi)^6} \int d^4x \int \frac{d^3p_1}{\omega_1} \frac{d^3p_2}{\omega_2} F(\vec{x}, \vec{p}_1, t) F(\vec{x}, \vec{p}_2, t) \hat{s} \hat{\sigma}(\hat{s}) \quad , \tag{3.36}$$

where $\hat{\sigma}(\hat{s})$ is the integrated cross section for the process $gg \to c\bar{c}$, see equation (2.5). Our main strategy is to estimate the mean difference between the two gluon rapidities, then, from the kinematical constraint on charm pro-

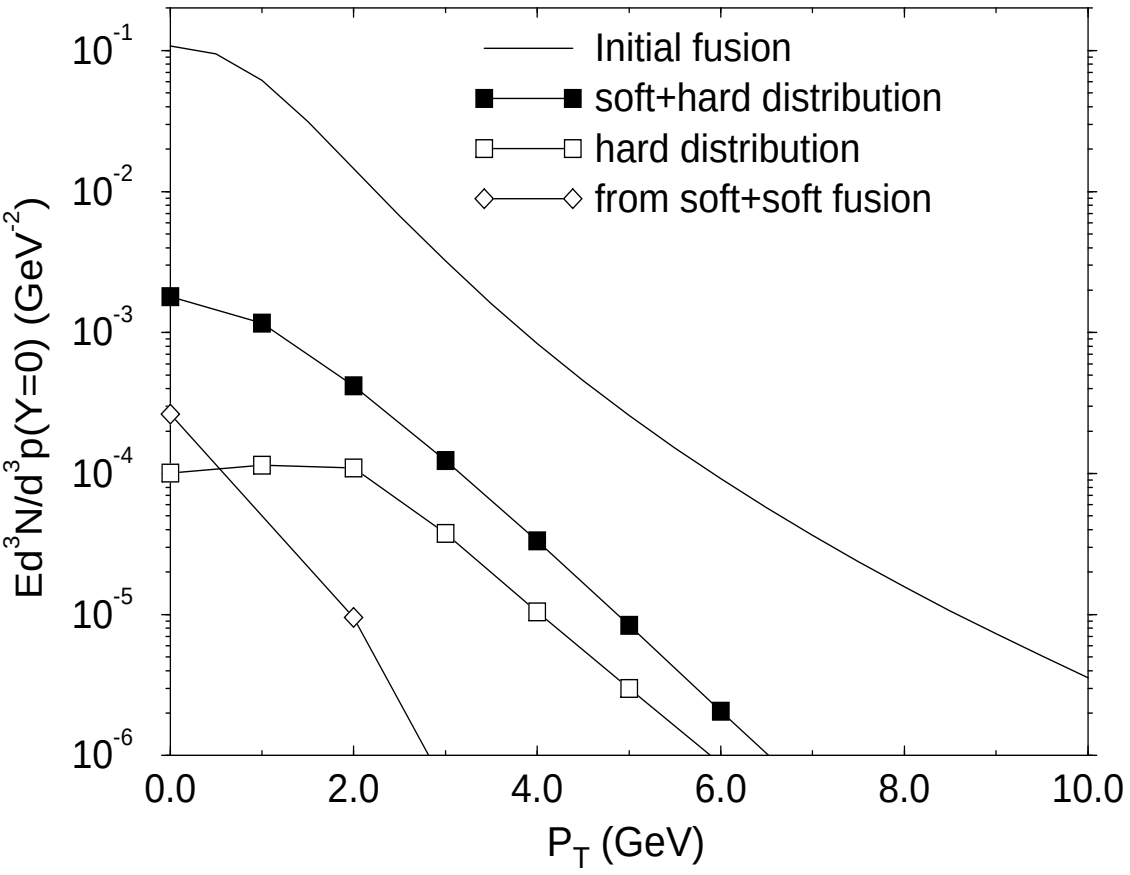

Figure 3.5: The distribution $(Ed^3N/d^3p)_{y=0}$ of charm quark production as a function of $p_\perp$ using minimal $\eta - y$ correlation.

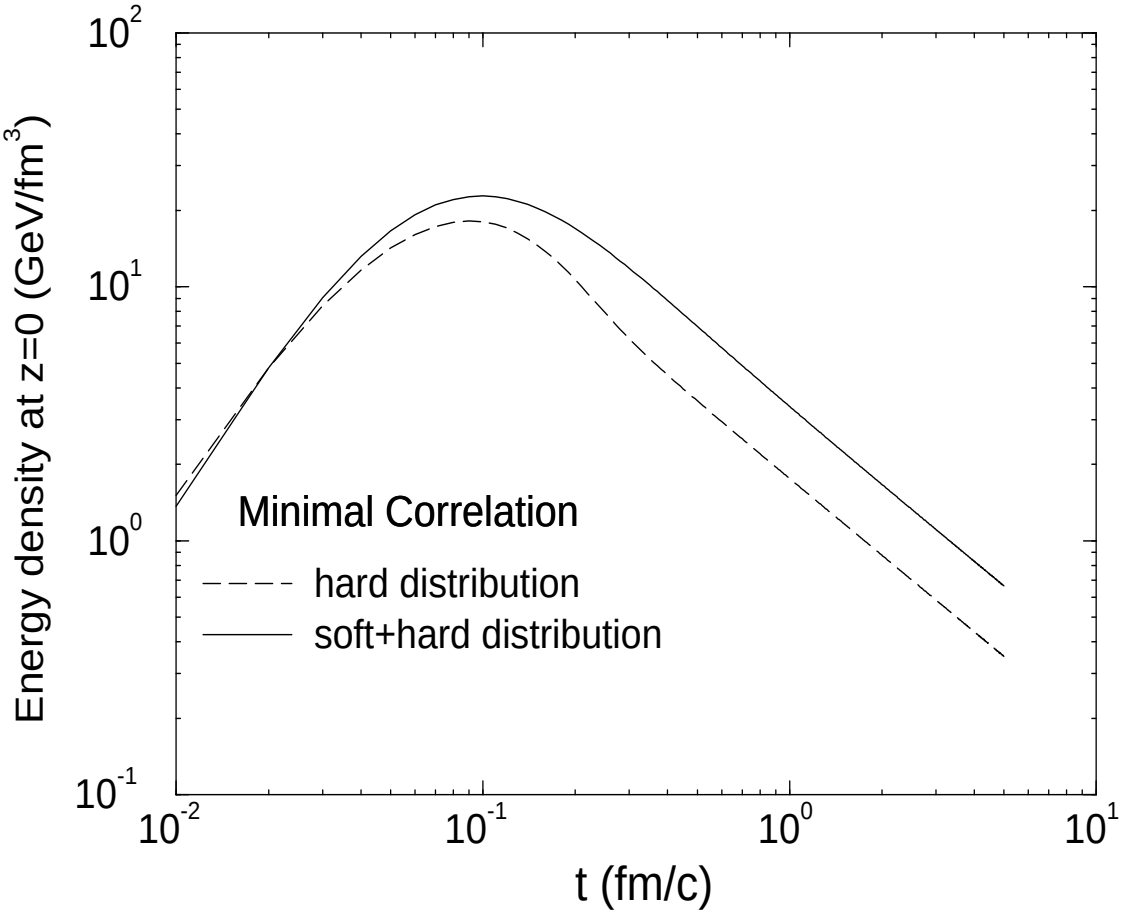

Figure 3.6: The energy density at $z = 0$ as a function of proper time.

duction ($\hat{s} \geq 4M_c^2$), estimate the effective lower cutoff for $p_\perp$ of the minijet gluons. Thus we separate the $p_\perp$ integrals from the rapidity integrals, and have a rough estimate for the total number of charm pairs.

For the fireball case,

$$F(\vec{x},\vec{p},t)_{Fb} = \frac{(2\pi)^3}{p}\frac{1}{V}\frac{dN}{dy d\vec{p_\perp}} \quad , \tag{3.37}$$

$$\hat{s} = 2p_{\perp 1}p_{\perp 2}\left[\cosh(y_1-y_2)-\cos(\phi_1-\phi_2)\right] \quad . \tag{3.38}$$

For the Bjorken case,

$$F(\vec{x},\vec{p},t)_{Bj} = \frac{(2\pi)^3}{p_\perp}\frac{dN}{dy d\vec{p_\perp}}\frac{\delta(\eta-y)}{\tau\pi R_A^2}\Theta(\tau-\tau_i)\Theta(\tau_f-\tau) \quad , \tag{3.39}$$

$$\hat{s} = 2p_{\perp 1}p_{\perp 2}\left[1-\cos(\phi_1-\phi_2)\right] \quad . \tag{3.40}$$

For all the cases, we use the fit to the gluon distribution given by equation (3.6), where

$$g(p_\perp) \equiv ae^{-bp_\perp} = 0.06e^{-1.25p_\perp} \quad . \tag{3.41}$$

Therefore,

$$\begin{aligned} N_{Fb} &= \frac{(\hbar c)^2\frac{\tau_f}{\tau_i}A^{8/3}}{4\pi R_A^2}\int dy_1\frac{\rho(y_1)}{\cosh y_1}\int dy_2\frac{\rho(y_2)}{\cosh y_2} \\ &\quad\times\int dp_{\perp 1}g(p_{\perp 1})\int dp_{\perp 2}g(p_{\perp 2})\int d\phi_1\int d\phi_2\hat{s}\hat{\sigma}(\hat{s}) \quad , \\ N_{Bj} &= \frac{(\hbar c)^2\ln\frac{\tau_f}{\tau_i}A^{8/3}}{4\pi R_A^2}\int d\eta\left[\rho(\eta)\right]^2 \\ &\quad\times\int dp_{\perp 1}g(p_{\perp 1})\int dp_{\perp 2}g(p_{\perp 2})\int d\phi_1\int d\phi_2\hat{s}\hat{\sigma}(\hat{s}) \quad . \end{aligned} \tag{3.42}$$

The dominant contribution is coming from the vicinity of the production threshold where $\hat{s} = 4M_c^2 = 9GeV^2$ [136]. From this we make the following rough estimates:

$$\begin{aligned} \hat{s}\hat{\sigma}(\hat{s}) &\sim \alpha^2(\hat{s}) \sim 0.06 \quad , \\ \int dp_\perp g(p_\perp) &\sim \int_{p_c}^{\infty} dp_\perp g(p_\perp) \sim \frac{a}{be^{bp_c}} \quad , \end{aligned} \tag{3.43}$$

where p_c is the effective cutoff value for $p_{\perp 1}$ and $p_{\perp 2}$ from the requirement $\hat{s} \geq 4M_c^2$.

For the fireball case,

$$\langle \cosh(y_1 - y_2) \rangle \equiv \frac{\int dy_1 dy_2 \frac{\rho(y_1)}{\cosh y_1} \frac{\rho(y_2)}{\cosh y_2} \cosh(y_1 - y_2)}{\int dy_1 dy_2 \frac{\rho(y_1)}{\cosh y_1} \frac{\rho(y_2)}{\cosh y_2}} \sim 4.0 \quad . \tag{3.44}$$

Since the minijet $p_\perp$ spectrum is dropping almost exponentially, the production heavily favors the smaller cutoff p_c, so the mean value of $\cos(\phi_1 - \phi_2)$ is most likely to be negative. We take

$$\langle \cos(\phi_1 - \phi_2) \rangle \sim -0.5 \quad . \tag{3.45}$$

Then

$$\hat{s} \sim 9p_c^2 \quad , \tag{3.46}$$

so the effective cutoff for the fireball case is

$$p_c \sim 1.0\text{GeV} \quad . \tag{3.47}$$

On the other hand, for the Bjorken case,

$$\begin{aligned} y_1 = y_2 = \eta \quad , \Rightarrow \hat{s} &\sim 3p_c^2 \quad , \\ \Rightarrow p_c &\sim 1.73\text{GeV} \quad . \end{aligned} \tag{3.48}$$

Using the same values as in Chapter 3.2: $\tau_i = 0.1fm$, $\tau_f = 1.0fm$ for fireball case, $\tau_f' = 1.7fm$ for Bjorken case, and

$$\int dy_1 \frac{\rho(y_1)}{\cosh y_1} \sim 2.8 \ ,$$
$$\int d\eta \left[\rho(\eta)\right]^2 \sim 4.9 \ . \tag{3.49}$$

We then have the estimate for the total number of the pre-equilibrium charm:

$$N_{Fb} \sim \frac{(\hbar c)^2 \frac{\tau_f}{\tau_i} A^{8/3}}{4\pi R_A^2} \, 2.8^2 (\frac{a}{be^{1.0b}})^2 (2\pi)^2 \left[\hat{s}\hat{\sigma}(\hat{s})\right] \sim 3.5 \ ,$$

$$N_{Bj} \sim \frac{(\hbar c)^2 \ln\frac{\tau_f'}{\tau_i} A^{8/3}}{4\pi R_A^2} \, 4.9 (\frac{a}{be^{1.73b}})^2 (2\pi)^2 \left[\hat{s}\hat{\sigma}(\hat{s})\right] \sim 0.098 \ . \tag{3.50}$$

Therefore we estimate $N_{Fb}/N_{Bj} \sim 35$, in rough agreement with the detailed numerics. We see that the large increase going from the Bjorken case to the fireball case results mainly from the different $p_\perp$ cutoff. In the uncorrelated fireball case, one allows particles with different rapidities to interact with each other (see equation (3.44)), thus more low $p_\perp$ gluons can take part in the interaction. Since the minijet $p_\perp$ spectrum drops almost exponentially, the fireball case produces much more pre-equilibrium charm than the Bjorken case (a factor of 6 increase from the smaller $p_\perp$ cutoff). Although the questionable linear proper time dependence in the fireball case also gives an considerable increase (about a factor of 3.5), it is not as important as the correlation effect.

For the minimal correlation case, the estimate is unfortunately not as

straightforward. The phase space distribution function is

$$F(\vec{x},\vec{p},t)_{Min} = \frac{(2\pi)^3}{\sqrt{2\pi}\pi R_A^2}\frac{e^{-(z-\tanh y\, t)^2(\frac{p_\perp}{\hbar c})^2/2}}{\hbar c\cosh y} \times\frac{dN}{dy\ d\vec{p_\perp}}\theta(\tau_{max}-\frac{t}{\cosh y})\theta(\frac{\hbar c\cosh y}{p_\perp}-\tau_{max}) \ , \quad (3.51)$$

and $\hat{s}$ is the same as in equation (3.38). In the above distribution function we choose to use the θ-function for the formation-time effect.

Using equation (3.36) and after the integration over z, we have

$$N_{Min} = \frac{(\hbar c)^2 A^{8/3}}{4\pi R_A^2\sqrt{\pi}}\int dp_{\perp 1} g(p_{\perp 1})\int dp_{\perp 2} g(p_{\perp 2})\int d\phi_1\int d\phi_2 \times \int dy_1\frac{\rho(y_1)}{\cosh y_1}\int dy_2\frac{\rho(y_2)}{\cosh y_2}\hat{s}\hat{\sigma}(\hat{s})\int_{t_{min}}^{t_{max}} dt\ \frac{e^{\frac{-(a_1-a_2)^2t^2}{1/b_1+1/b_2}}}{\sqrt{1/b_1+1/b_2}} \ , \quad (3.52)$$

where

$$t_{min} = \hbar c\max\left(\frac{\cosh y_1}{p_{\perp 1}},\frac{\cosh y_2}{p_{\perp 2}}\right) \ ,$$

$$t_{max} = \tau_f\min(\cosh y_1,\cosh y_2) \ , \quad (3.53)$$

and a_1, a_2, b_1, b_2 are defined the same as in equation (3.32).

We estimate that for the dominant part of the integral

$$\frac{1}{b_1}+\frac{1}{b_2}\sim\left(\frac{2\hbar c}{p_c}\right)^2 \ ,$$

$$t_{min}\sim\frac{\hbar c\cosh\bar{y}}{p_c} \ ,$$

$$t_{max}\sim\tau_f\cosh\bar{y} \ , \quad (3.54)$$

where $\bar{y} = (|y_1| + |y_2|)/2$. Now let $u = t\ p_c/(\hbar c \cosh \bar{y})$, then the last 3-dimensional integral in equation (3.52) without the factor $\hat{s}\hat{\sigma}(\hat{s})$ is

$$J \sim \int dy_1 \frac{\rho(y_1)}{\cosh y_1} \int dy_2 \frac{\rho(y_2)}{\cosh y_2} \frac{1}{2} \cosh \bar{y} \times \int_1^{\frac{\tau_f p_c}{\hbar c}} du\ e^{-[\frac{\sinh(y_1-y_2)\cosh \bar{y}}{2\cosh y_1 \cosh y_2}]^2 u^2} \quad . \tag{3.55}$$

The u-integral gives a dependence on τ_f which is similar to the logarithmic dependence in the Bjorken case, and the exponential form in the integrand forces the spread $y_1 - y_2$ to be small. Numerically, by taking $\tau_f \sim 1.7 fm/c$, $p_c \sim 2.0$ GeV (as the first-step value) in the u-integral, the above 3-dimensional integral is $J \sim 19.1$. When the integrand is weighed by $\cosh(y_1 - y_2)$, the integral is ~ 23.3. So

$$\langle \cosh(y_1 - y_2) \rangle \sim 23.3/19.1 \sim 1.22 \quad ,$$

$$\Rightarrow \hat{s} \sim 3.44 p_c^2 \quad , \Rightarrow p_c \sim 1.62 \text{GeV} \quad . \tag{3.56}$$

Note that the above determined value of p_c is insensitive to the first-step p_c value we tried in the u-integral.

Therefore for the total pre-equilibrium charm number,

$$N_{Min} \sim \frac{(\hbar c)^2 A^{8/3}}{4\pi R_A^2 \sqrt{\pi}} \int dp_{\perp 1} g(p_{\perp 1}) \int dp_{\perp 2} g(p_{\perp 2}) \int d\phi_1 \int d\phi_2\ J\ \hat{s}\hat{\sigma}(\hat{s})$$

$$\sim \frac{(\hbar c)^2 A^{8/3}}{4\pi R_A^2} \frac{J}{\sqrt{\pi}} (\frac{a}{b e^{1.62b}})^2 (2\pi)^2\ [\hat{s}\hat{\sigma}(\hat{s})] \sim 0.10 \quad . \tag{3.57}$$

Therefore $N_{Min}/N_{Bj} \sim 1$. From the above estimate we can see that although the minimally-correlated case allows particles with different rapidities to interact, the dominant contribution still comes from the region where the two

gluons have almost the same rapidity, thus there is no sizeable enhancement in the pre-equilibrium charm yield. The Minimally-Correlated case is very much like the Bjorken case in that the dominant contribution comes from $y_1 \simeq y_2$ region.

As a comparison to the above rough estimates in this chapter, the numerical integration gives $N_{Fb} = 3.8$, $N_{Bj} = 0.093$, and $N_{Min} = 0.078$, so $N_{Min}/N_{Bj} \sim 80\%$.

3.5 Discussion

In order to see the formation-time effect, in Figure 3.7 we compare the results from two different formation-time assumptions. The solid curve is obtained using the Lorentzian form in equation (3.24), and the dashed curve using the theta function form in equation (3.26). The result from this θ-function is about 10% higher at $p_\perp = 0$GeV, and 10% lower at $p_\perp = 9$GeV. The lack of sensitivity to the formation-time physics is due to the relative large $p_\perp$ for the gluon minijets in the charm production process. There would be more sensitivity had the production been dominated by low $p_\perp$ components.

We also see that for the soft+hard distribution, soft gluons significantly increase the pre-equilibrium charm production in both low-$p_\perp$ and high-$p_\perp$ region, with the largest increase in low-$p_\perp$ region. It is interesting to identify where the enhancement comes from. In Figure 3.5, the curve with diamonds shows the contribution from the fusion of soft gluons both with $p_\perp < 2$ GeV, and the curve with hollow squares shows the contribution from the fusion

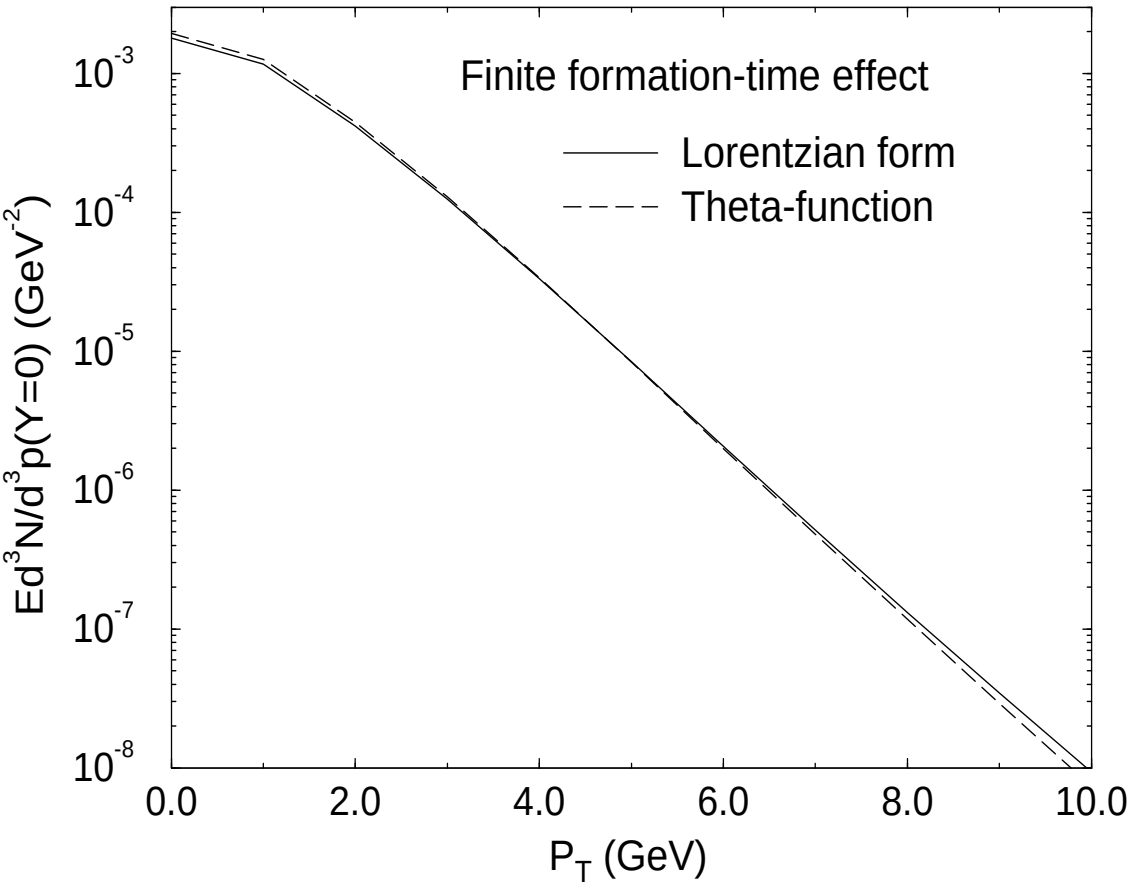

Figure 3.7: The distribution $(Ed^3N/d^3p)_{y=0}$ of charm quark production using different formation-time probability distributions.

of hard gluons both with $p_\perp > 2$ GeV. These two curves are both very low compared with the curve calculated from the soft+hard distribution. Therefore the enhancement going from the hard distribution to the soft+hard distribution is mainly due to the fusion of hard and soft minijet gluons.

We have noted before that our fit for the minijet gluon spectrum falls below the Monte Carlo result from HIJING calculation. We can fit the soft gluons from HIJING better by using $0.265e^{-2.6p_\perp}$ for $p_\perp \in (0, 1.1)$ GeV, and use the old fit $0.06e^{-1.25p_\perp}$ for higher-$p_\perp$ gluons. This new fit gives us more very soft gluons. Using the new fit, we have done the calculation for minimally-correlated case, and the result is different only by less than 10%. We therefore conclude that super-soft gluons are not very important for the pre-equilibrium charm production.

3.6 Summary

For the pre-equilibrium charm production, we studied the effect of correlations between the rapidity y and space-time rapidity η of minijet gluons. In the ideal Bjorken-correlated case, where $\eta = y_1 = y_2$, the pre-equilibrium charm production is negligible compared with the yield due to initial gluon fusion. For the opposite extreme fireball case, corresponding to uncorrelated y and η, the pre-equilibrium charm production is almost a factor of 50 larger than in the Bjorken-correlated case and is comparable with the initial charm yield [62]. With the estimates of the total pre-equilibrium charm number, we found that the difference comes mainly from the $\eta - y$ correlation. There-

fore, the pre-equilibrium charm production is very sensitive to the $(\eta - y)$ correlations in the initial state.

In order to investigate the effect of more realistic correlations that may exist in the initial minijet plasma, we introduced a minimal correlation model taking into account the uncertainty principle along the lines of [167]. This minimal correlation is similar to the ideal Bjorken correlation case and produces negligible pre-equilibrium charm compared with the initial charm yield.

Chapter 4

Gluon Shadowing In Lepton Pair Spectra From Open Charm Decay

Dileptons from charm decay are probably dominant relative to the conventional signals from the plasma at RHIC such as thermal dileptons [88]. Here we offer a different point of view on the dilepton measurement [133]. Instead of considering it merely as a background, we propose to use opposite-sign lepton pairs (ee,$e\mu$ and $\mu\mu$) from open charm decay in $p+A$ collisions as a measure of nuclear shadowing effects. We focus here on $p+A$ collision rather than $A+A$ to minimize the combinatorial π, K decay backgrounds and other final state interaction effects.

4.1 Introduction

The spectrum of dileptons produced in heavy ion collisions at high energies has been proposed in the past to provide information about the dynami-

cal evolution of quark-gluon plasmas (see, e.g., the review by Ruuskannen in [169]). Unlike hadronic probes, this spectrum is sensitive to the earliest moments in the evolution, when the energy densities are an order of magnitude above the QCD confinement scale (1 GeV/fm^3). However, the small production cross sections for pairs with invariant mass above 1 GeV together with the large combinatorial background from decaying hadrons necessitate elaborate procedures to uncover the signal from the noise. The PHENIX detector [39], now under construction at the Relativistic Heavy ion Collider (RHIC), is designed to measure $ee, e\mu$, and $\mu\mu$ pairs to carry out this task. One of the important background sources in the few GeV mass range arises from semileptonic decay of charmed hadrons ($D\bar{D}$). As shown recently in [88], the expected thermal signals in that mass range may only reach 10% of pairs from open charm decay. It is much more difficult to precisely measure these signals than to measure dileptons from charm decay, and special kinematical cuts and precise $e\mu$ measurements are necessary to uncover the thermal signals [39].

There have been several attempts [44, 62] to take advantage of the large open charm background as a probe of the evolving gluon density. Most mid-rapidity charm pairs are produced via gluon fusion [142]. Therefore, the dileptons from charm decay carry information about the distribution of primordial gluons before hadronization. In fact, the inside-outside cascade nature of such reactions greatly suppresses [132, 54] all sources of charm production except the initial perturbative QCD source. Therefore, the open

charm background is dominated by the *initial* gluon fusion ($gg \to c\bar{c}$) rate.

The initial $c\bar{c}$ rate depends strongly on the nuclear gluon structure function [170], $g_A(x, Q^2)$. The quantity of fundamental interest [131, 134] is the gluon shadowing function

$$R_{g/A}(x, Q^2) = \frac{g_A(x, Q^2)}{A g_N(x, Q^2)} \quad . \tag{4.1}$$

The point of this study is to demonstrate that the A dependence of continuum dilepton pairs in the few GeV mass region provides a novel probe of that unknown gluon structure. We also show that the required measurements of ee,$e\mu$, and $\mu\mu$ pair yields in $p + A \to \ell^+\ell^- X$ at $\sqrt{s} = 200$ AGeV are not only experimentally feasible at RHIC but also that the open charm signal can be easily extracted via the proposed PHENIX detector.

A key advantage of the continuum dilepton pairs from open charm decay over those from J/ψ decay is that it is possible to test the applicability of the underlying QCD dynamics at a given fixed $\sqrt{s}$ by checking for a particular scaling property discussed below. In quarkonium production the mass is fixed and the required scaling can be checked only by varying the beam energy. In $p + A \to J/\psi$ production the required scaling was unfortunately found to be violated in the energy range $20 < \sqrt{s} < 40$ AGeV [171], thus precluding a determination of R_A. Possible explanations for the breakdown of QCD scaling for J/ψ production and its anomalous negative x_F behavior [170, 171] include interaction of next-to-leading order quarkonium Fock state with nuclear matter [68], nuclear and co-mover J/ψ dissociation [172], and parton energy loss mechanisms [173]. It remains an open question whether

the required scaling will set in at RHIC energies $60 < \sqrt{s} < 200$ AGeV.

We propose to use ee,$e\mu$ and $\mu\mu$ pairs from open charm decays to probe the shadowing effects in nuclei. These three measurements cover three different rapidity regions as a result of the PHENIX detector geometry. In Chapter 4 we calculate the lepton pair spectrum from open charm decay in $p + Au$ at 200 GeV/A using two commonly used shadowing scenarios: the parameterization which does not depend on scale or parton component [70], and the scale-dependent, component-dependent shadowing [166]. The difference between these two shadowing scenarios is significant. The ratio curve of dilepton $dN/dMdy$ spectra from $p + A$ to those from pp has a similar shape to the shadowing curve. We then show that there is an approximate scaling among the ratio curves at different dilepton pair-mass M, which enables us to bring them together to the shadowing function curve. In Chapter 4.7 we first estimate the original backgrounds of the lepton pair spectra. The large number of electrons from Dalitz decay and the muons from random decay of pions or kaons results in large backgrounds for $e\mu$ and dilepton experiments. Without suppression and kinematical cuts, it is much higher than the signal from charm decay. In chapter 4.8, we consider the PHENIX detector geometry, a specific kinematical cut and the suppression factors of the background leptons. We calculate the lepton pair signal and backgrounds entering the detector, and the signal-to-background ratio is very promising. For ee and $e\mu$ spectra, the signal is bigger than the background. For $\mu\mu$ spectra, the signal is smaller than the background, but with the help of like-sign subtraction,

it is possible to also observe the $\mu\mu$ signal from open charm decay. In chapter 4.9, we show the signal and background for the single inclusive electron and muon spectrum. The signal from single inclusive leptons reflects the shadowing effects less effectively, and the signal-to-background ratio there is much smaller than that for the lepton pair case. Finally in chapter 4.12 we give the discussion and summary.

4.2 A Recent Attempt to Extract Nuclear Gluon Shadowing

Recently there appeared an attempt [174] to extract nuclear gluon shadowing from the high statistics F_2^A data on S_n and C taken by NMC [175].

Parton structure functions depend on Bjorken x, the momentum fraction of the parton in the frame where the nucleon (or nucleus) is moving very fast, and Q^2, the momentum scale at which the parton structure function is being resolved. The Q^2 evolution equations for the gluon number density, $G(x)$, and the quark number densities, $q_i(x)$ (i from 1 to $2n_f$), are given by the Altarelli-Parisi equations [176] as

$$\begin{aligned} \frac{\partial G(x)}{\partial t} &= \frac{\alpha}{2\pi}\int_x^1 \frac{dy}{y}\left[\sum_j P_{Gq_j}(z)q_j(y) + P_{GG}(z)G(y)\right] , \\ \frac{\partial q_i(x)}{\partial t} &= \frac{\alpha}{2\pi}\int_x^1 \frac{dy}{y}\left[\sum_j P_{q_iq_j}(z)q_j(y) + P_{q_iG}(z)G(y)\right] , \end{aligned} \tag{4.2}$$

where $z \equiv x/y$, and $t \equiv \ln(Q^2/Q_0^2)$. There are four splitting functions, $P_{Gq_j}(z), P_{GG}(z), P_{qq}(z), P_{q_iq_j}(z)$ and $P_{q_iG}(z)$, and a function $P_{AB}(z)$ is basi-

cally proportional to the probability that a parton B splits to a parton A with fraction z of the momentum of the parent parton B.

Based on the Altarelli-Parisi equation (4.2) for quarks, the Q^2 evolution equation for the quark distribution

$$F_2(x,Q^2) = x\sum_i e_i^2 q_i(x,Q^2) \tag{4.3}$$

is therefore given as

$$\frac{\partial F_2(x)}{\partial t} = \frac{\alpha}{2\pi}x\int_x^1 \frac{dy}{y}\left[\sum_{ij} e_i^2 P_{q_iq_j}(z)q_j(y) + \sum_i e_i^2 P_{q_iG}(z)G(y)\right] \tag{4.4}$$

$$= \frac{\alpha}{2\pi}x\int_x^1 \frac{dz}{z}\left[\sum_i e_i^2 P_{qq}(z)q_i(\frac{x}{z}) + \sum_i e_i^2 P_{qG}(z)G(\frac{x}{z})\right] \tag{4.5}$$

$$\equiv \frac{\alpha}{2\pi}\left(P_{qq} * F_2 + x\sum_i e_i^2 P_{qG} * G\right) \quad . \tag{4.6}$$

The above two convolutions are defined as

$$P_{qG} * G = \int_x^1 \frac{dz}{z}P_{qG}(z)G(\frac{x}{z}) = \int_x^1 \frac{dz}{2z}[z^2+(1-z)^2]G(\frac{x}{z}) \tag{4.7}$$

$$\begin{aligned} P_{qq} * F_2 &= \int_x^1 dz P_{qq}(z)F_2(\frac{x}{z}) \quad , \\ &= \int_x^1 dz \frac{N_c^2-1}{2N_c}\left[\frac{1+z^2}{(1-z)_+} + \frac{3}{2}\delta(1-z)\right]F_2(\frac{x}{z}) \\ &= \frac{4}{3}\int_x^1 dz\left[\frac{(1+z^2)F_2(x/z)-2F_2(x)}{(1-z)} + \frac{3}{2}\delta(1-z)F_2(\frac{x}{z})\right], \end{aligned} \tag{4.8}$$

with the divergence at $z=1$ being regularized by the definition

$$\int_0^1 dz\frac{f(z)}{(1-z)_+} \equiv \int_0^1 dz\frac{f(z)-f(1)}{(1-z)} \quad . \tag{4.9}$$

Using the approximation

$$\int_x^1 dz[z^2+(1-z)^2]\frac{x}{z}G(\frac{x}{z}) \simeq \frac{4x}{3}G(2x) \quad , \tag{4.10}$$

one can relate the second term in eq.(4.6), $P_{qG} * G$, directly to the gluon density function $G(x)$. Note that the first term in eq.(4.6), $P_{qq} * F_2$, is only related to $F_2(x)$, which can be computed from data.

Thus from the Q^2 dependence of the quark distribution F_2, one can extract some information on the gluon density G. In the above, one neglects the effects of higher order corrections and the non-linear recombination terms [131]. The non-linear term probably does not have a large magnitude unless the parton momentum fraction x is extremely small [131, 166, 177].

In Figure 4.1 [174], the so-extracted ratio of gluon density of tin to carbon $r(x, Q^2) = G^{S_n}(x, Q^2)/G^C(x, Q^2)$ is plotted against the gluon momentum fraction x in small x range $0.01 < x < 0.1$, together with the $F_2(x, Q^2)$ data from which the ratio $r(x, Q^2)$ is extracted. The ratio of gluon density shows both the shadowing effect in the lower range of x and the anti-shadowing effect in the higher range of x, similar to the case of quark shadowing.

4.3 The Q^2 Evolution of Nuclear Parton Distributions

There are mainly two steps to determine nuclear shadowing effects. First we need to know the parton distribution functions in nuclei at some initial momentum scale Q_0. Given the input nuclear parton distributions at the scale Q_0, we then calculate the parton structure functions at any values of scale Q according to evolution equations. As long as Q is within the perturbative QCD domain, Q^2 evolution equations are known from pQCD [176, 131].

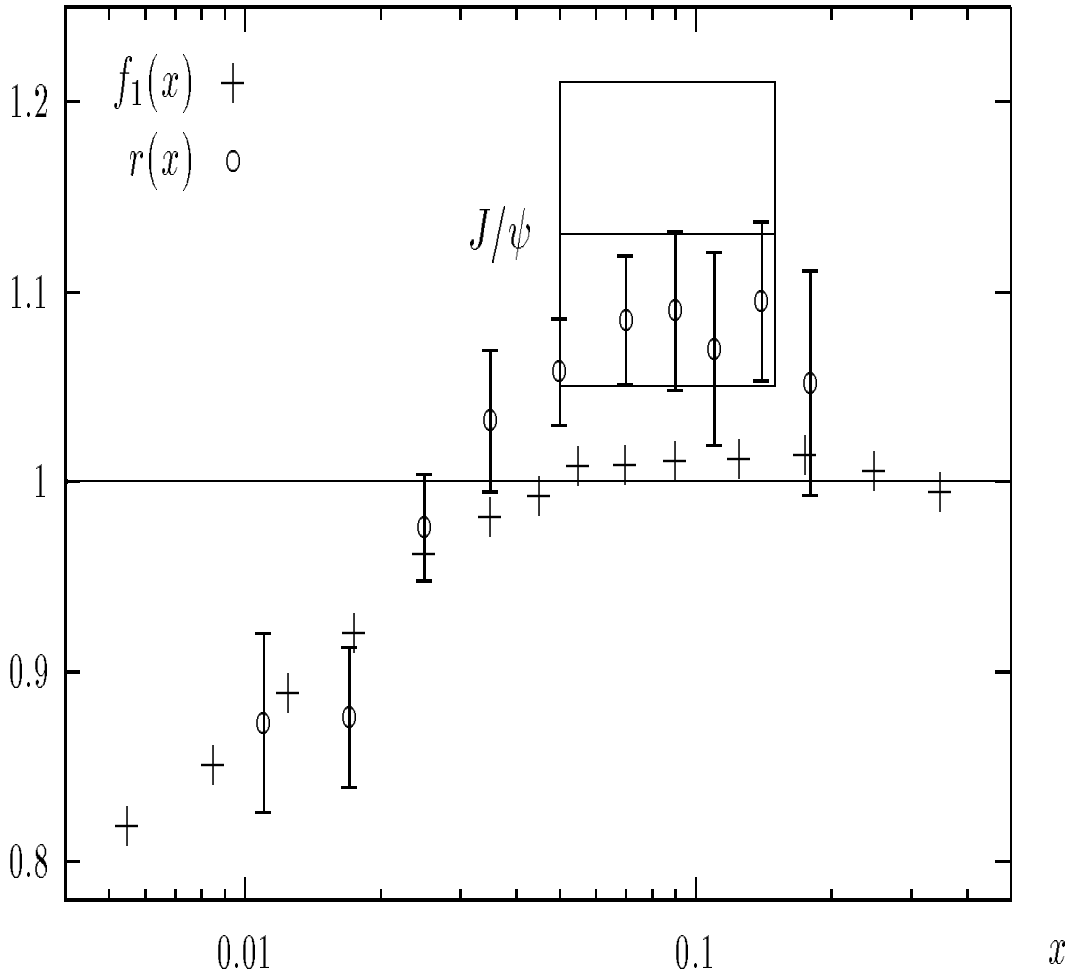

Figure 4.1: The ratio $r(x) = G^{Sn}(x)/G^{C}(x)$ of tin to carbon gluon density, together with the ratio of structure function, $f_1(x) = F_2^{Sn}(x)/F_2^{C}(x)$, as a function of x, from [174].

The input parton structure functions, $G(x,Q_0^2)$ and $q_i(x,Q_0^2)$, contain all non-perturbative nuclear effects at the scale Q_0. They are thus, in principle, not calculable within pQCD. However, it is not hard to imagine that nuclear shadowing effects occur to nuclear parton distributions [178]. We can imagine that shadowing effects occur when partons from different nucleons in nuclei begin to overlap spatially. For a nucleus with momentum p per nucleon, the longitudinal size of the parton with momentum xp is $\sim 1/(xp)$. The longitudinal separation of different nucleons is $\sim 2r_0m/p$, where m is the nucleon rest mass, and r_0 is the nucleon radius. Thus shadowing effects occur when $x < 1/(2r_0m)$. Shadowing effects grow as partons overlap more, until the partons are overlapping completely. This saturation of shadowing effects happens when the longitudinal size of the parton is about equal to the longitudinal size of the nucleus, i.e. $x \sim 1/(2R_Am)$, where R_A is the radius of the nucleus.

Q^2 evolution equations of parton density functions are usually given by Altarelli-Parisi equations (AP) [176], as expressed in eqs. (4.2). They can be rewritten separately for the gluon momentum distribution xG, the flavor singlet sea quark part xS, and the flavor nonsinglet valence quark part xV:

$$\begin{aligned} Q^2\frac{\partial}{\partial Q^2}xG(x,Q^2) &= \frac{\alpha(Q^2)}{2\pi}\int_x^1\frac{dy}{y}\Big[zP_{Gq}(z)y\left(V(y,Q^2)+S(y,Q^2)\right) \\ &\quad +zP_{GG}(z)yG(y,Q^2)\Big] \quad , \end{aligned} \tag{4.11}$$

$$\begin{aligned} Q^2\frac{\partial}{\partial Q^2}xS(x,Q^2) &= \frac{\alpha(Q^2)}{2\pi}\int_x^1\frac{dy}{y}\Big[zP_{qq}(z)yS(y,Q^2) \\ &\quad +zP_{qG}(z)yG(y,Q^2)\Big] \quad , \end{aligned} \tag{4.12}$$

$$Q^2\frac{\partial}{\partial Q^2}xV(x,Q^2) = \frac{\alpha(Q^2)}{2\pi}\int_x^1\frac{dy}{y}zP_{qq}(z)yV(y,Q^2) \ , \tag{4.13}$$

where the sea quark momentum distribution $xS = xu_s, xd_s$ or xs_s.

The four splitting functions are given as [176]

$$P_{qG}(z) = \frac{1}{2}\left(z^2+(1-z)^2\right) \ , \tag{4.14}$$

$$P_{GG}(z) = 6\left(\frac{1-z}{z}+\frac{z}{(1-z)_+}+z(1-z)\right) + \left(\frac{11}{2}-\frac{n_f}{3}\right)\delta(1-z) \ , \tag{4.15}$$

$$P_{qq}(z) = \frac{4}{3}\frac{1+z^2}{(1-z)_+}+2\delta(1-z) \ , \tag{4.16}$$

$$P_{Gq}(z) = \frac{4}{3}\frac{1+(1-z)^2}{z} \ , \tag{4.17}$$

where $(1-z)_+^{-1}$ is defined in eq. (4.9).

The AP-evolution means that as Q^2 increases, we can see more small-x partons and less high-x ones, because high-momentum partons lose energy by radiation. Thus the parton density can become very large at sufficiently small x. However, as the parton density becomes huge at small x, the AP-evolution equations have to be modified [131] because gluons then have more probability to recombine to reduce the numbers of partons in the nuclei. Mueller and Qiu [131, 178] modified the AP-equations by calculating the recombination probabilities for gluons to go into gluons or into quarks. The AP-evolution equation(4.11) for gluons and equation(4.12) for sea quarks are

modified to the following AP+MQ-equations:

$$Q^2\frac{\partial}{\partial Q^2}xG(x,Q^2) = \frac{\alpha(Q^2)}{2\pi}\int_x^1\frac{dy}{y}\Big[zP_{Gq}(z)y\Big(V(y,Q^2)+S(y,Q^2)\Big) + zP_{GG}(z)yG(y,Q^2)\Big] - \frac{n}{Q^2}R_{gg\to g}(x,Q^2) \ , \quad (4.18)$$

$$Q^2\frac{\partial}{\partial Q^2}xS(x,Q^2) = \frac{\alpha(Q^2)}{2\pi}\int_x^1\frac{dy}{y}\Big[zP_{qq}(z)yS(y,Q^2) + zP_{qG}(z)yG(y,Q^2)\Big] - \frac{n}{Q^2}\Big[R^{(1)}_{gg\to q}(x,Q^2)+R^{(2)}_{gg\to q}(x,Q^2)\Big] \ , \quad (4.19)$$

where the nuclear number density $n \sim 1/(\pi R^2)$, and the contributions to the evolution from recombinations of gluons into gluons or into quarks are

$$R_{gg\to g}(x,Q^2) = \frac{4\pi^3}{N^2-1}\left[\frac{\alpha(Q^2)C_A}{\pi}\right]^2\int_x^1\frac{dy}{y}\Big[yG(y,Q^2)\Big]^2 \ , \quad (4.20)$$

$$R^{(1)}_{gg\to q}(x,Q^2) = \frac{4\alpha^2(Q^2)T_f\pi}{N(N^2-1)}\left(\frac{4N^2}{15}-\frac{3}{5}\right)\Big[xG(x,Q^2)\Big]^2 \ , \quad (4.21)$$

$$R^{(2)}_{gg\to q}(x,Q^2) = -\frac{2\alpha(Q^2)T_f}{\pi}\int_x^1\frac{dy}{y}z\bar{\gamma}_{FG}(z)yG_{HT}(y,Q^2) \ . \quad (4.22)$$

In the above $T_f = 1/2$, $C_A = N = 3$, $\bar{\gamma}_{FG}(z) = -2x + 15x^2 - 30x^3 + 10x^4$.

$$Q^2\frac{\partial}{\partial Q^2}yG_{HT}(y,Q^2) = -R_{gg\to g}(y,Q^2) \quad (4.23)$$

gives the evolution for the higher-dimensional gluon distribution G_{HT}. This distribution function is basically not calculable [178]. Since it comes from two-gluon interaction, it has the form, at some scale Q_0, as

$$yG_{HT}(y,Q_0^2) = K_{HT}\Big[yG(y,Q_0^2)\Big]^2 \ , \quad (4.24)$$

where K_{HT} is a constant.

From the above AP+MQ-equations, the modification terms from two-gluon recombinations to the AP-equations are basically of the form

$$\alpha^2(yG)^2/(R^2Q^2) \quad . \tag{4.25}$$

We take gluons for example, and *roughly* represent the modified evolution equation(4.18) as

$$Q^2\frac{\partial xG(x,Q^2)}{\partial Q^2} \;\sim\; \alpha\frac{6}{2\pi}xG(x,Q^2) - \alpha^2\frac{4\pi n}{Q^2}\left[xG(x,Q^2)\right]^2 \quad . \tag{4.26}$$

The modification term, the second on the right-hand side in eq.(4.26), therefore slows down the Q^2 evolution of the gluon density function. To make a rough estimate of the onset of non-linear recombination effects, we equal the two terms in eq.(4.26), the usual AP-evolution term and the gluon recombination term, and get the condition as

$$xG(x,Q^2) \sim \frac{3Q^2}{4\pi^2 n\alpha} \sim \frac{Q^2R^2}{\pi\alpha} \quad . \tag{4.27}$$

The modification will be significant only when x is so small that the above condition is reached. If we take $R = 1fm$, $Q \simeq 2$GeV, the above condition will be reached only for extremely small x where $xG(x,Q^2) \sim 100$. Thus the recombination is likely to be a very small correction to the usual Q^2 evolution equations of parton structure functions.

Modified evolution equations (AP+MQ) was first numerically solved by Qiu [178], and then by Eskola [166]. Eskola assumes a shadowing ansatz at

an initial scale $Q_0 = 2\text{GeV}$ for heavy nuclei with $A \simeq 200$, then evolves shadowed Duke-Owens parton distributions [144] according to both AP equations and modified evolution equations (AP+MQ). The MQ-modification slows down the increase of the parton densities with Q^2, and therefore shadowing effects go away slower with the increase of Q^2 than in the AP-evolution case. However, the difference between the AP-evolution and the AP+MQ-evolution with this particular choice of input parton distributions is found to be only on the order of 10% [166], thus the mainline of the evolution of parton structure functions is given by the usual AP-equations.

4.4 Nuclear Shadowing in Open Charm Production

We use two common shadowing scenarios: the parameterization which does not depend on scale or component (HIJING's scaling) [70], and the scale-dependent, component-dependent shadowing (Eskola's shadowing) [166]. The production for $c\bar{c}$ in one $A+B$ collision at a fixed impact-parameter $\vec{b}$ is given by [62]

$$\frac{dN^{AB}}{dp_\perp^2\, dy_1 dy_2} = K \int d^2r \sum_{a,b} x_a \Gamma_{a/A}(x_a, Q^2, \vec{r}) x_b \Gamma_{b/B}(x_b, Q^2, \vec{b} - \vec{r}) \frac{d\sigma_{ab}}{d\hat{t}} \quad ,(4.28)$$

where

$$\Gamma_{a/A}(x, Q^2, \vec{r}) = T_A(\vec{r}) f_{a/N}(x, Q^2) R_{a/A}(x, Q^2, \vec{r}) \qquad (4.29)$$

is the nuclear parton density function in terms of the known nucleon parton structure functions $f_{a/N}(x, Q^2)$, the nuclear thickness function $T_A(\vec{r}) =$

$\int dz n_A(\sqrt{z^2+\vec{r}^2})$, and the unknown impact-parameter-dependent shadowing function $R_{a/A}(x,Q^2,\vec{r})$. The conventional kinematic variables $x_{a,b}$ are the incoming parton light cone momentum fractions, $\hat{t}=-(p_b-p_1)^2$, and the final $c,\bar{c}$ have rapidities y_1,y_2 and transverse momenta $\vec{p}_{1\perp}=-\vec{p}_{2\perp}\equiv\vec{p}_\perp$. Next-to-leading order corrections to the lowest order parton cross sections $d\hat{\sigma}_{ab}/d\hat{t}$ are approximately taken into account by a constant K factor [151, 152]. We use the recent MRSA [145] parton structure functions. From a fit to low energy open charm production data in pp collisions, we fix $m_c=1.4$ GeV, $K=3$, $Q^2=\hat{s}/2$ for $gg\to c\bar{c}$ and $\hat{s}$ for $q\bar{q}\to c\bar{c}$. This choice of parameters leads to a charm pair cross section of $340\mu b$ for pp collisions at RHIC. For impact-parameter-averaged collisions, the integral over the transverse vector in eq.(4.28) leads to a factor:

$$BAR_{b/B}(x_b,Q^2)R_{a/A}(x_a,Q^2)/\sigma_{in}^{BA} \quad , \tag{4.30}$$

where σ_{in}^{BA} is the inelastic $B+A$ cross section and $R_{a/A}(x_a,Q^2)$ is the impact-parameter-averaged shadowing function.

Therefore for $c\bar{c}$ production in impact-parameter-averaged $p+Au$ collisions, we have

$$\frac{d\sigma^{p+Au}}{dp_\perp^2\,dy_1dy_2}=KA\sum_{a,b}x_af_{a/N}(x_a,Q^2)x_bf_{b/N}(x_b,Q^2)R_{b/Au}^{p+Au}(x_b,Q^2)\frac{d\sigma_{ab}}{d\hat{t}}, \tag{4.31}$$

where $R_{b/Au}^{p+Au}(x_b,Q^2)$ is the impact-parameter-averaged shadowing function for the parton b in Au nucleus.

The two different shadowing functions are plotted in Figure 4.5. It is clear that HIJING's scenario has much stronger shadowing than Eskola's scenario

in almost all regions of interest, and Eskola's scenario has anti-shadowing in $x \geq 0.1$ region. These features are reflected in the final $e\mu$ spectrum, as we will show in the following chapter.

4.5 $e\mu$ Spectrum from $D/\bar{D}$ Decay

Since the mass difference of e and μ has little effect on the semileptonic decay of charmed meson, the spectra of dilepton pair ee and $\mu\mu$ from charm decay have shapes almost identical to the $e\mu$ spectrum. Since we include both $e^+\mu^-$ and $e^-\mu^+$ pairs, and assume the average branching ratio for $D \to \mu + X$ is the same as for $D \to e + X$, the $e\mu$ signal is twice as large as the ee and $\mu\mu$ signal.

To compute the $D\bar{D}$ pair distribution, a hadronization scheme for $c \to D$ must be adopted. In $e^+e^- \to c\bar{c} \to D\bar{D}X$ hadronization can be modelled via string fragmentation or fitted, for example, via the Peterson fragmentation function (see [141]). The final D carries typically only a fraction ~ 0.7 of the original c momentum. However, in pp collisions, charm hadronization is complicated by the high density of partons produced during beam jet fragmentation. In this system recombination or coalescence of the heavy quark with co-moving partons provides another mechanism which in fact seems to be dominant at least at present energies. The inclusive $pp \to DX$ data is best reproduced [141, 179] with the delta function fragmentation $D(z) = \delta(1 - z)$ in all observed x_f and moderate p_T regions. This observation can be understood in terms of a coalescence model if the coalescence

radius is $P_c \sim 400$ MeV. We assume that hard fragmentation continues to be the dominant mechanism at RHIC energies, and therefore no additional A-dependent effects from hadronization will arise. However, this assumption must be tested experimentally. Therefore our main dynamical assumption is that the $pp \to D$ transverse momentum distributions can be accurately reproduced from the QCD level rates assuming hard fragmentation, as at present energies [179]. At RHIC this can be checked either via single inclusive leptons [39] or directly via $K\pi$ [180].

With this assumption, the impact-parameter-averaged $D\bar{D}$ pair distribution in $p + A$ is given by

$$\frac{dN^{pA}}{dp_\perp^2 dy_3 dy_4} = \frac{KA}{\sigma_{in}^{pA}} \frac{E_3 E_4}{E_1 E_2} \times \sum_{b,a} x_b f_{b/N}(x_b, Q^2) x_a f_{a/N}(x_a, Q^2) R_{a/A}(x_a, Q^2) \frac{d\hat{\sigma}_{ab}}{d\hat{t}} \quad . (4.32)$$

Note that there is no $p_\perp$ kick here, and D and $\bar{D}$ in a pair have opposite azimuthal directions.

After the above spectrum $dN/dp_\perp^2 dy_3 dy_4$ for the charmed mesons is calculated, we use Monte Carlo programs to simulate their semileptonic decays [181]. We generate $D/\bar{D}$ events according to the above spectrum. For each event, we decay one charmed meson in its rest frame to an electron, and decay the other charmed meson in its rest frame to a muon isotropically, according to the parameterized semileptonic energy spectrum. We then boost the electron and muon back according to the momentum of its meson parent.

We then calculate the invariant mass

$$M = \sqrt{(p_e + p_\mu)^2} \tag{4.33}$$

and the rapidity

$$y = \tanh^{-1}[(p_e^{||} + p_\mu^{||})/(E_e + E_\mu)] \tag{4.34}$$

for the pair and have the final $e\mu$ pair spectrum $dN/dMdy$.

In Figure 4.2(a) we plot the absolute rate $d\sigma^{e\mu}/dMdy$ from the above Monte Carlo calculation, and it includes both $e^+\mu^-$ and $e^-\mu^+$ signals. The solid, dashed and dot-dashed curves represent the non-shadowing, Eskola's shadowing, and HIJING's shadowing case, respectively. From top to bottom, the three sets of solid, dashed and dot-dashed curves correspond to different pair-masses $M = 1, 2, 4$ GeV. In Figure 4.2(b), the ratio of the curves in (a) from two shadowing cases to that from the non-shadowing case is plotted at pair-masses $M = 1$ (solid), 2 (dashed), 4 (dot-dashed) GeV. The upper(lower) set of three curves corresponds to Eskola(HIJING)'s shadowing. The curves in Figure 4.2(b) resemble the shapes of shadowing curves in Figure 4.5. Note that in Figure 4.5 the abscissa is in logarithmic scale and in Figure 4.2 the abscissa is in linear scale. We see that the shadowing effect is much stronger in positive pair-rapidity region. This is expected since in $p + A$ collisions positive pair-rapidity corresponds to smaller x from nucleus A and thus deeper shadowing. For Eskola's scenario some anti-shadowing effect shows up in the negative pair-rapidity region. One may notice that in Figure 4.2(b) we have a narrower rapidity region at higher invariant masses.

That is because at the edges of the rapidity region we have fewer Monte Carlo events, and we discard the edges to restrain big statistical fluctuations.

4.6 Scaling

Since gluon fusion dominates, there is an approximate scaling in terms of the light cone fraction x_A that one of the gluon carries from nucleus A:

$$\ln x_A = -y_{c\bar{c}} + \ln(M_{c\bar{c}}/\sqrt{s}) \quad . \tag{4.35}$$

While the lepton pair-mass M and rapidity y fluctuate around a mean value for any fixed $M_{c\bar{c}}$ and $y_{c\bar{c}}$, on the average

$$\langle y \rangle \approx \langle y_{c\bar{c}} \rangle \quad , \tag{4.36}$$

and $\langle M_{c\bar{c}} \rangle$ can be well approximated by a linear relation

$$\langle M_{c\bar{c}} \rangle \approx \beta M + M_0 \tag{4.37}$$

over the lepton pair-mass range $1 \leq M \leq 4$GeV. For the delta function fragmentation case, $\beta \approx 1.5$ and $M_0 \approx 3.0$ GeV are determined by the D-meson decay kinematics. In Figure 4.3 we plot the average $M_{c\bar{c}}$ as a function of M, the mass of the correlated lepton pair from the $c\bar{c}$ decay with the delta function fragmentation. The above relation between the average masses is determined from the following histogram plot generated from Monte Carlo calculation, which showed the event number density on the plane of charm pair-mass $M_{c\bar{c}}$ and the mass M of the dielectron from the charm semileptonic decays (the unit of mass is GeV in the figure).

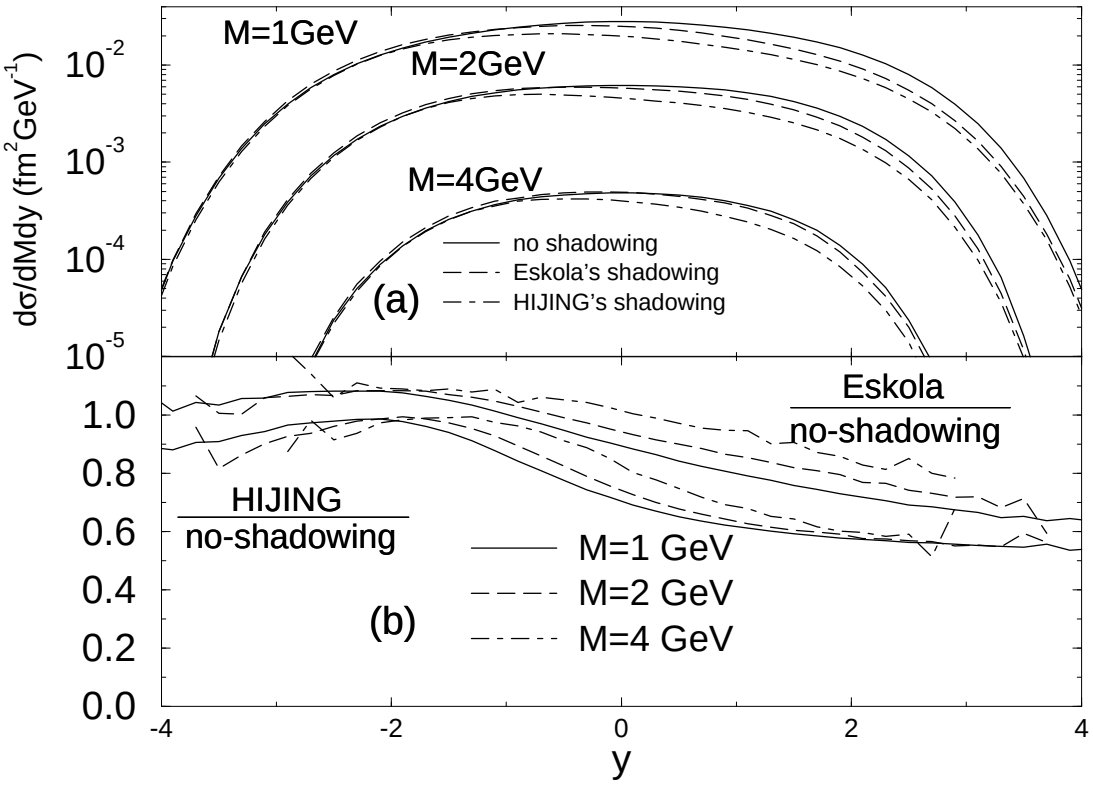

Figure 4.2: (a) The production of opposite-sign $e\mu$ pairs as a function of pair-rapidity y at pair-masses $M = 1, 2, 4$ GeV; (b) The ratio of shadowing curves over non-shadowing curves in (a).

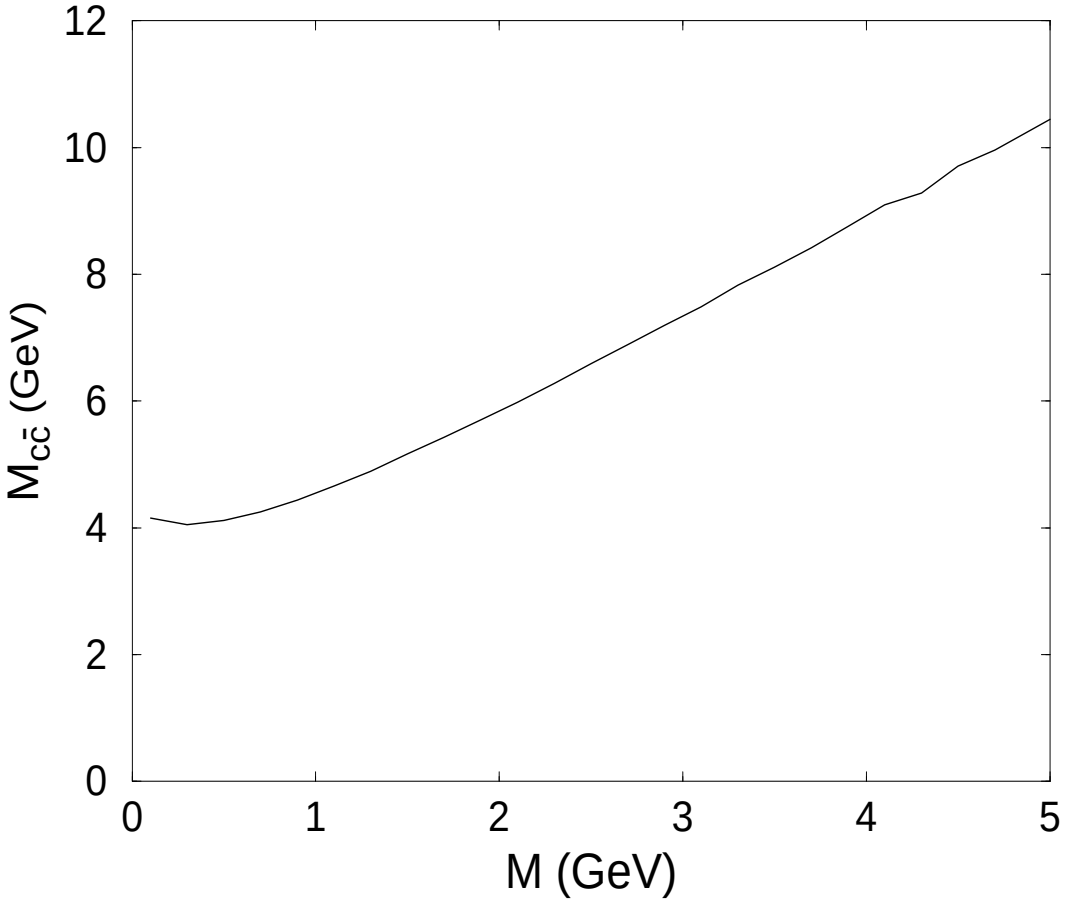

Figure 4.3: The average mass $M_{c\bar{c}}$ as a function of dilepton mass M.

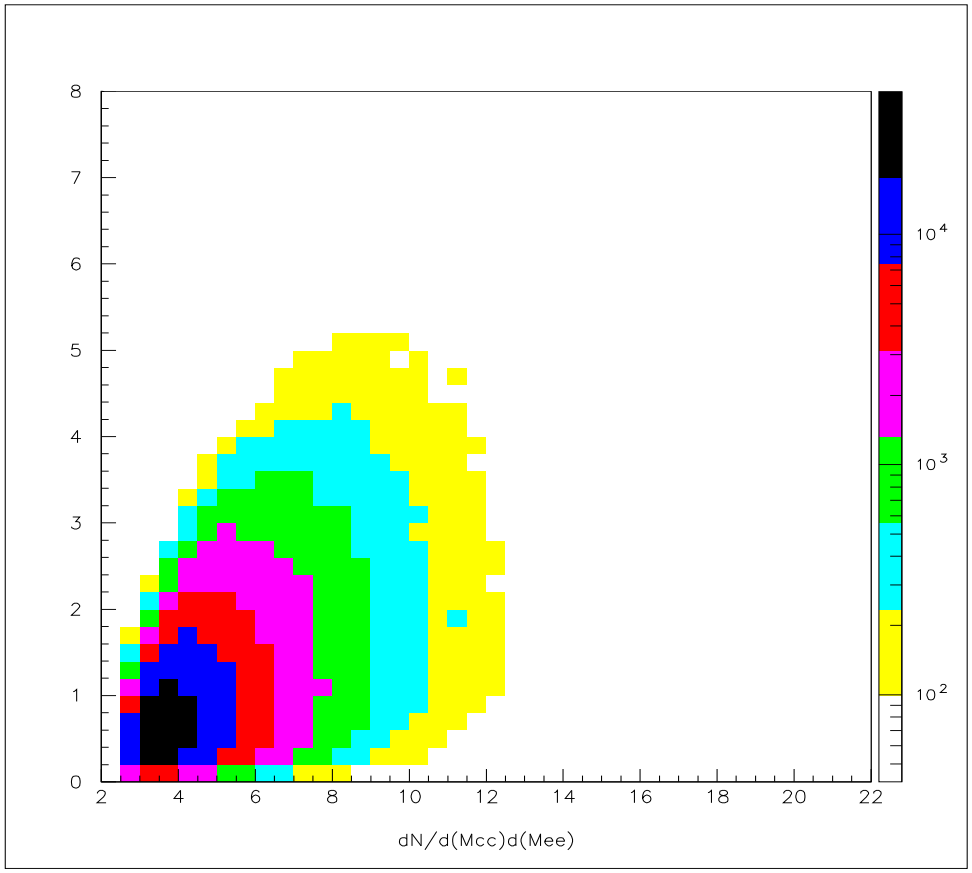

Figure 4.4: Probability distribution of M, the dilepton mass from charm pair decay, as a function of $M_{c\bar{c}}$ in $p + Au$ collision.

Therefore,

$$\ln x_A \approx -y + \ln[(\beta M + M_0)/\sqrt{s}] \ . \tag{4.38}$$

The ratio of the dilepton $dN/dMdy$ spectra in pA to scaled pp for different pair-masses is thus expected to scale approximately as

$$\begin{aligned} & R^{pA}_{e\mu}(M, y = -\ln x_A + \ln[(\beta M + M_0)/\sqrt{s}] \ ) \\ & \equiv \frac{1}{\nu}\frac{dN^{pA}_{e\mu}}{dN^{pp}_{e\mu}} \approx R_{g/A}(x_A, Q^2 \approx (\beta M + M_0)^2/2 \ ) \ , \end{aligned} \tag{4.39}$$

where $\nu \equiv A\sigma^{pp}_{in}/\sigma^{pA}_{in} \sim A^{1/3}$.

In order to test gluon dominance and the accuracy of the above approximate scaling, we compare in Figure 4.5 the gluon shadowing function to the above dilepton ratio from the Monte Carlo calculation. The upper solid curve is Eskola's gluon shadowing [166] for $Q^2 = 10$ GeV^2, and the lower solid curve is shadowing from HIJING [70]. The other six curves are ratios of dilepton $dN/dMdy$ spectra of shadowed $p + Au$ over those from unshadowed $p + Au$, as given by eq.(4.39) as a function of the scaling variable x_A for three different dilepton masses. In Figure 4.5 we first plot all the ratio curves in terms of reversed pair-rapidity $-y$, then we shift the ratio curves at $M = 1, 2, 4$ GeV to the left by $3.79, 3.51$, and 3.10 respectively.

Overall, with an approximate scaling the ratio of spectra from $p + A$ to those from pp reflects the nuclear shadowing function well. We conclude that this ratio can therefore serve to map out gluon shadowing in nuclei. Note that in the case of Eskola's shadowing, even the Q^2 dependence of the

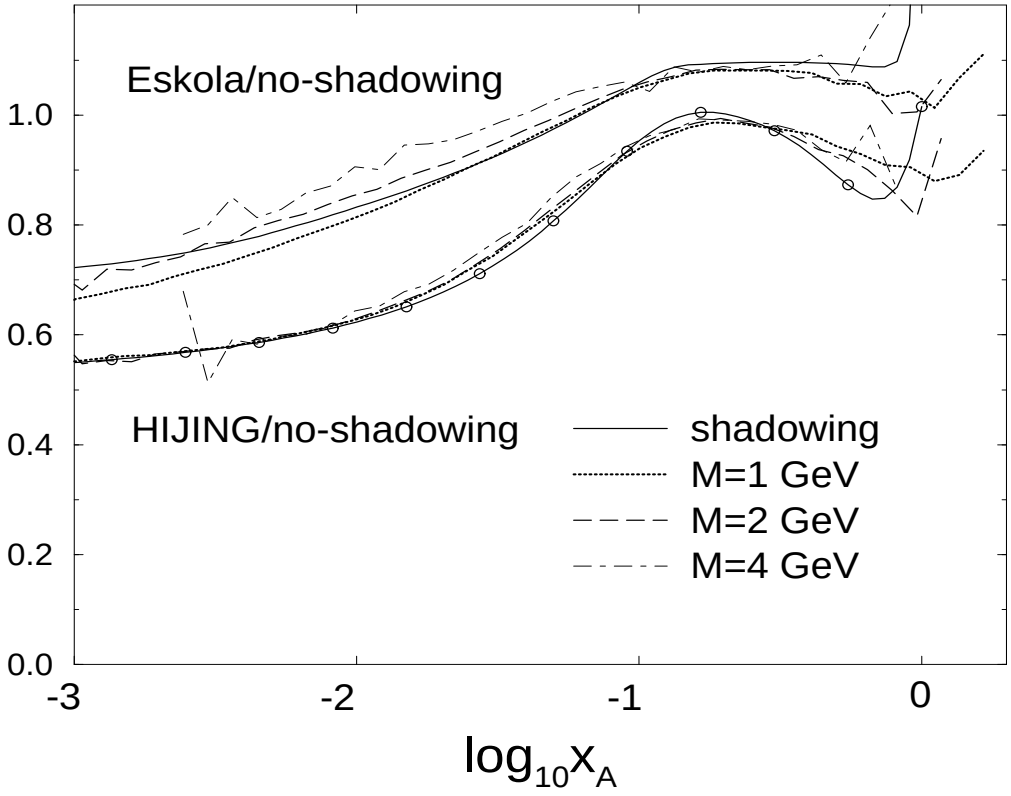

Figure 4.5: Dilepton $dN/dMdy$ ratio curves (shadowed over unshadowed) as a function of the scaling variable $\log_{10} x_A$ at different masses, and the comparison with shadowing curves.

shadowing function is visible through the rise of the ratio curves with M in the small x region.

4.7 Original Backgrounds

It is important to estimate the dilepton background to see if the proposed signal is experimentally feasible. In this chapter we estimate some dominant backgrounds without taking any suppression or kinematical cuts. In chapter 4.8 we calculate the signal and background dileptons for the PHENIX detector [39], taking into account the detector geometry and specific kinematical cuts.

The electron background comes from Dalitz decay of π^0 mainly, and also from Dalitz decay of higher mass particles and resonances. Also we have electron background from photon conversion. For dielectron measurements, π^0 Dalitz decay background ($\pi^0 \rightarrow e^+e^-\gamma$) is quite problematic. The correlated pair from Dalitz decay has an invariant mass smaller than the pion mass, so ideally we can eliminate all these electrons and positrons by invariant mass constraint. However, electrons with small momenta may be easily lost in the strong magnetic field in the detector, in addition, we will not have 4π solid angle coverage. Although we can reject many of these leptons by using techniques like small-angle cuts for dielectron pairs, we still have background from π^0 Dalitz decay, and this is also a problem for $e\mu$ measurements. The main muon background comes from the random decays of charged pions and kaons. They can decay in the free space before the hadron absorber, and they can also decay in the absorber or leak through. According to the momentum resolution in the PHENIX muon detector ($\sigma(\theta_p) = 0.4°, \sigma(\phi_p) = 1.6°$) [39], it is very difficult to differentiate these muons from muons coming directly

from charm decay.

Let us estimate the dielectron numbers in a central $p + Au$ collision at 200 GeV/A at RHIC. Given N as the number of π^0s, P as the branching ratio of $\pi^0 \rightarrow e^+e^-\gamma$, the average number of combinatoric (uncorrelated) dielectron pairs is then $N(N-1)P^2$. The HIJING Monte Carlo calculation [70] gives about 38 π^0s, and the branching ratio of π^0 Dalitz decay is about 1.2%. Therefore the average number of dielectrons originating from the π^0 background is 0.2. Compared to the next largest source (dileptons from the $D/\bar{D}$ decay), this background is enormous. Using HIJING's shadowing, we have 0.05 $D/\bar{D}$ pairs. With the average branching ratio of $D \rightarrow e + X$ at about 12%, the dielectron yield from charm decay is about 0.0007, a factor of 300 below the original background from π^0 Dalitz decay. For dimuon numbers in a central $p + Au$ collision at RHIC, HIJING gives about 34 π^+s and π^-s each, and they almost all decay to muons. Thus, the original dimuon background from charged pions is 1.1×10^3, which is enormous compared with the dimuon yield from charm decay (also about 0.0007). For opposite-sign $e\mu$ numbers, the original background originating from π^0 and $\pi^+(\pi^-)$ is 31., compared to $e\mu$ from charm decay (about 0.0014).

The above provides us with a rough idea of the opposite-sign lepton pair backgrounds before we suppress them. We must suppress them in order to observe signals from charm decay and thus probe nuclear shadowing.

4.8 Backgrounds Entering the Detector

In this chapter we study the backgrounds entering the detector by including detector-related effects: the suppression factor for leptons, proposed PHENIX detector geometry, and a specific kinematical cut for the events. These are based on the RHIC report [39]. Then we compare the backgrounds to the lepton pairs signal from charm decay.

The electrons from π^0 Dalitz decay could be suppressed by the small-angle cut for dielectron pairs since they have an invariant mass less than the pion mass. We suppose we could reject 90% of the π^0 Dalitz electrons [182]. We also have electron background from photon conversions, which has a softer spectrum. We suppose we have the same rejection rate of 90% for the conversion electrons. Each of the two photons decayed from π^0 has a 0.5% probability of conversion to electron/positron pair, and the π^0 Dalitz decay branching ratio is 1.2%; as an upper limit we will simply double the electron background from π^0 Dalitz decay to include the contribution from photon conversion. From HIJING program, in terms of number of electrons from π^0 Dalitz decay, there is approximately 40% more electrons from K^- decay. We also assume a rejection rate of 90% for these electrons based on the estimates of free space decay probability and angular resolution for the vertex. Thus, the number of background electrons after rejection is 24% of the number of π^0 Dalitz electrons, which means we have a suppression factor of about 4 for the original background electron number from π^0 Dalitz decay. We generate the background electrons from the electron spectrum calculated

from HIJING program (using proper weights for π^0 Dalitz and K^- Dalitz events), since electrons from K^- have a harder spectrum, and thus a greater probability of passing the kinematical cut.

The background muons can come from decays in the free space before the hadron absorber, which is about 32 centimeters(L) from the nominal vertex. For a charged pion with mass m, energy E, and proper decay time τ, the probability of the decay in free space is about $Lm/\tau E$. We would use an energy cut of 2 GeV for muons, therefore this probability is less than 0.3%. There is also a background from particles that have leaked through the absorber, which decay to muons in flight inside the muon arm. From the RHIC report, for charged hadrons above 1 GeV in the muon arm for a central $AuAu$ collision at 200 GeV, the leakage number is 4.8, which is about 0.1% of the total number of charged pions. Their decay to muons is also suppressed by the long proper lifetime τ and Lorentz γ factor as above, and those which have not decayed will mostly be differentiated by the muon identifier. So the probability of finding a muon above 1 GeV from the decays of leakage particles is about 0.003%. Considering the factor from the geometry and energy cuts explained below, the probability from leakage before these cuts is also 0.3%. The charged hadrons could also decay in the absorber during the shower. After all, we take 1% of the muon number from charged pion decay as the estimate of the muon background passing the hadron absorber and muon identifier, which means we have a suppression factor of 100 for the original background muon number. We generate background muons from

the muon spectrum calculated from HIJING program, which is mainly from π^+, π^- two-body decay, and, in very small amounts, from decay of heavier particles such as K^+ and K^-.

For the PHENIX detector geometry, the electron arm barrel covers electron pseudo-rapidity range

$$-0.35 < \eta_e < 0.35 \quad , \tag{4.40}$$

and azimuthal angle range

$$\phi_e \in \pm(22.5^\circ, 112.5^\circ) \quad . \tag{4.41}$$

The muon arm endcap covers the polar angle range $10^\circ < \theta < 35^\circ$ and almost the full azimuthal angle. Thus, we only require muon pseudo-rapidity range to be

$$1.15 < \eta_\mu < 2.44 \quad . \tag{4.42}$$

For the kinematical cut used to improve the signal-to-background ratio, we take

$$E_e > 1\text{GeV} \quad , \tag{4.43}$$

$$E_\mu > 2\text{GeV} \quad . \tag{4.44}$$

We also require the relative azimuthal angle of the lepton pair to be $\phi_{l^+l^-} > 90^\circ$, and this improves the ratio by a factor of 2. We find the following percentages for the numbers of leptons which pass the above energy and pseudo-rapidity requirements: 1.1% for electrons from charm decay, 2.7%

for muons from charm decay, 0.02% for background electrons, and 1.0% for background muons. The small percentage for background electrons is due to the small mass of the particles which make Dalitz decays, and this greatly lowers the electron background. Recently, a second muon arm at the opposite end is proposed to increase the muon rapidity coverage.

Considering the above suppression factors resulting from the geometry and the kinematical cuts, we calculate the signal and the backgrounds entering the detector. First, the ee, $e\mu$ and $\mu\mu$ signals entering the detector from charm decay are calculated in three different shadowing cases. The dN/dM plots of different shadowings are shown in Figure 4.6, and the dN/dy plots are shown in Figure 4.7. In Figure 4.6, results from non-shadowing case (solid), Eskola's shadowing (dashed), and HIJING's shadowing (dot-dashed) are plotted. Figure (a), (b), (c) are for opposite-sign ee, $e\mu$ and $\mu\mu$, respectively. In Figure 4.7, the left, middle and right set of three curves correspond to opposite-sign ee, $e\mu$ and $\mu\mu$ signals. Note that the $e\mu$ and $\mu\mu$ yields are scaled down by a factor of 4 and 15, respectively. Due to detector geometry and kinematical cuts, ee, $e\mu$ and $\mu\mu$ spectra cover pair-rapidity regions centered at about 0, 1 and 2, respectively (the second PHENIX muon arm can reach pair-rapidity region centered around -1 and -2). As shown in Figure 4.2(b) for the signal without cuts, the shadowing effect is stronger in larger pair-rapidity region.

We then generate background electrons and muons based on HIJING calculation, and calculate the ee, $e\mu$ and $\mu\mu$ backgrounds entering the detector.

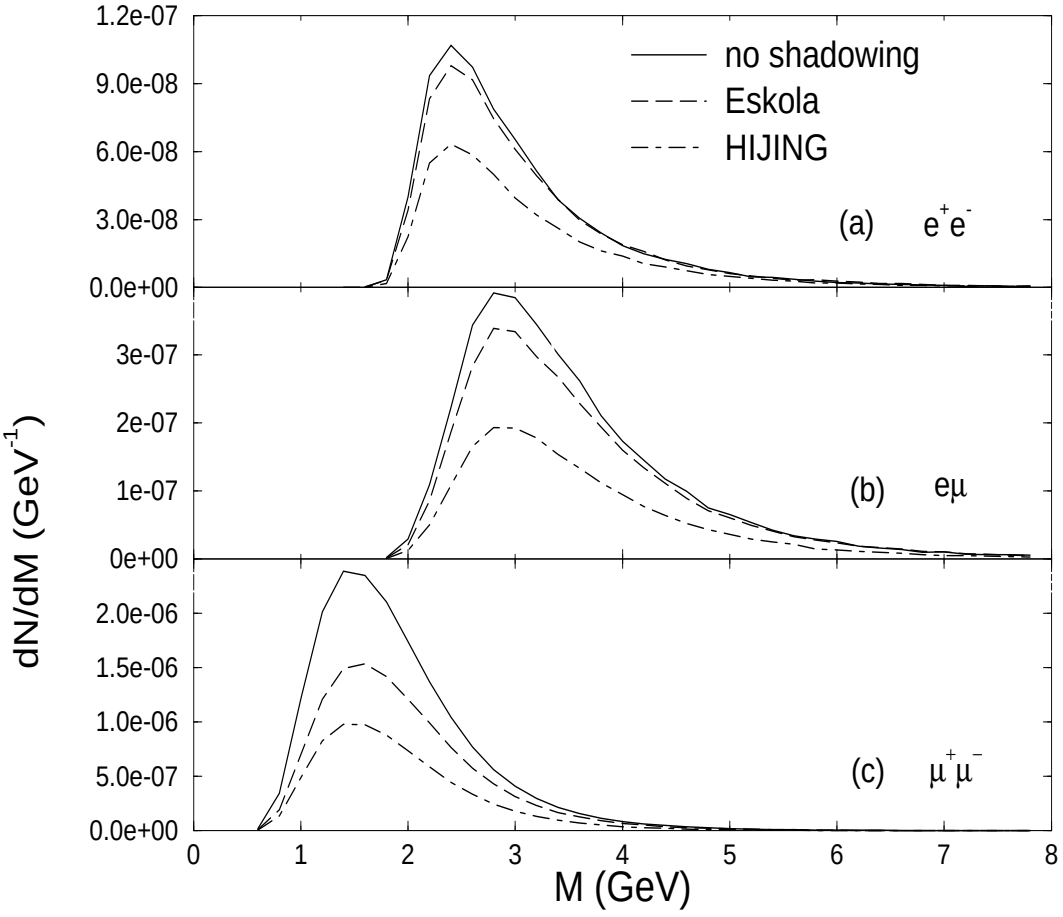

Figure 4.6: dN/dM spectra for lepton pairs entering the PHENIX detector for different shadowing cases.

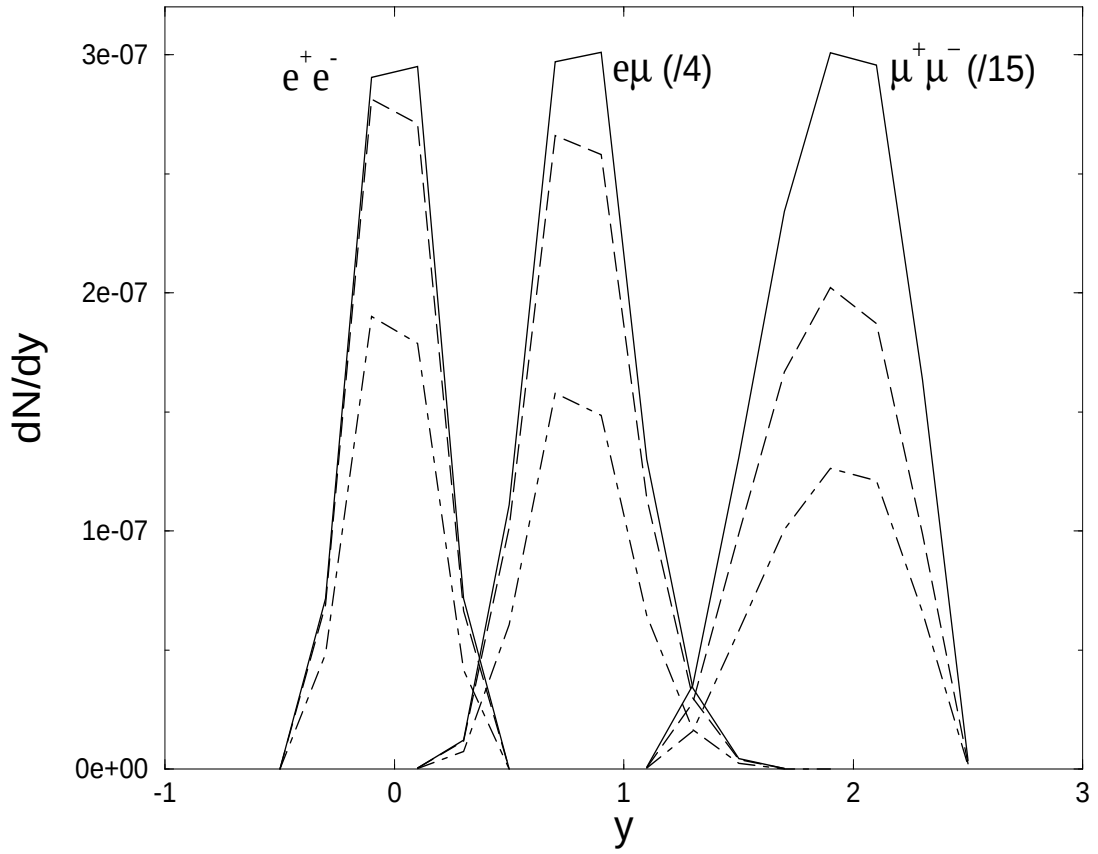

Figure 4.7: dN/dy spectra for lepton pairs entering the detector for different shadowing cases.

We compare the backgrounds with the calculated signal from the HIJING shadowing case. The dN/dM plots of signal and backgrounds are shown in Figure 4.8, and the dN/dy plots are shown in Figure 4.9. In Figure 4.8, the solid curves represent the signals from open Charm decay — labeled CC signal. The label C refers to the lepton originating from open Charm decay, label D refers to the electron originating from Dalitz and photon conversion, and label R refers to the muon originating from Random decay of pions and kaons. In (a), the dielectron backgrounds are represented by the dashed curve DC and the dot-dashed curve DD; and both are scaled up by a factor of 100. In (b), the opposite-sign $e\mu$ backgrounds are represented by the dotted curve CR, the dashed curve DR, and the dot-dashed curve DC. In (c), the dimuon backgrounds are represented by the dashed curve RR and the dot-dashed curve RC. The notations in Figure 4.9 are the same as in Figure 4.8.

We find that the signal-to-background ratio for ee is very large, thus the dielectron signal from open charm decay is the easiest to extract. That ratio falls to about 2.5 for $e\mu$, and about 1/4 for $\mu\mu$. Note that we have not included the backgrounds from Drell-Yan and thermal production that will most change the above signal-to-background ratio for ee.

One could further suppress the lepton pair backgrounds by like-sign subtraction, especially in the $\mu\mu$ channel. Since the particle production has a fairly good charge symmetry, the background opposite-sign lepton pairs are almost the same as the like-sign pairs. The signals from open charm decay are almost all opposite-sign pairs, so we could subtract like-sign pairs

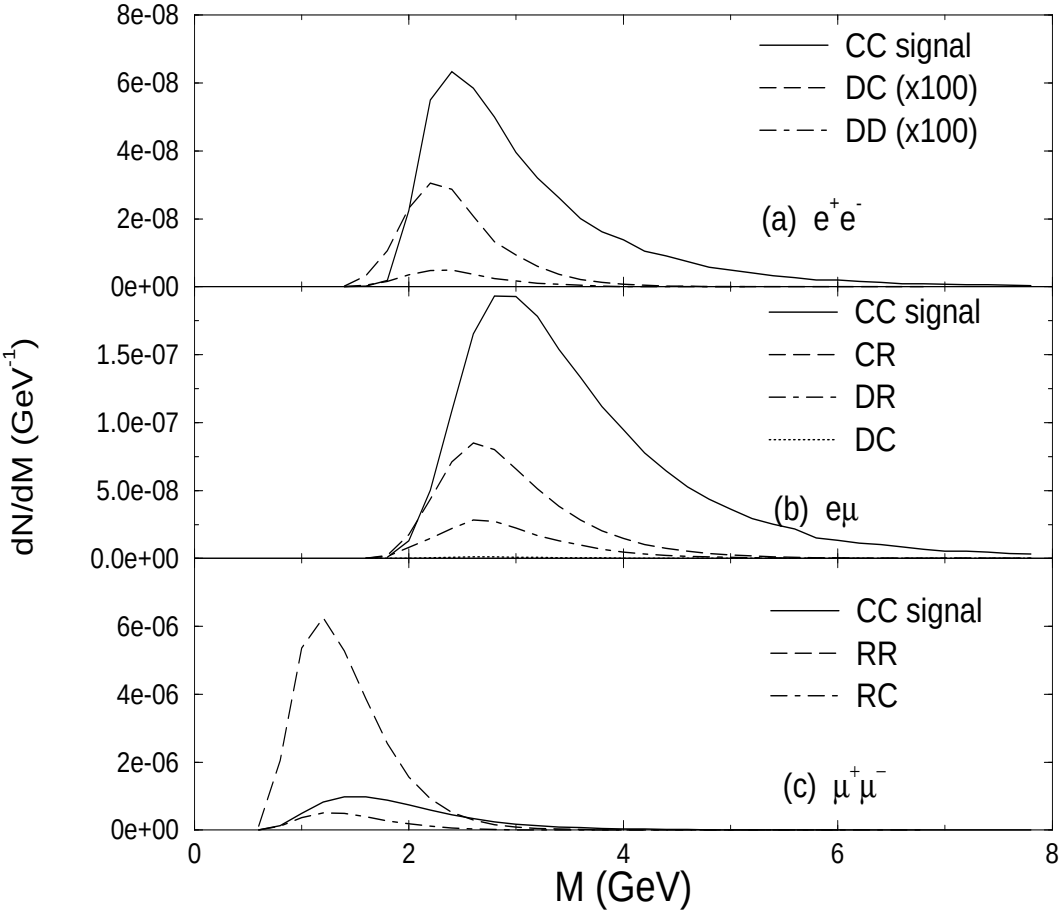

Figure 4.8: Charm signal and backgrounds entering the detector as a function of the lepton pair-mass M.

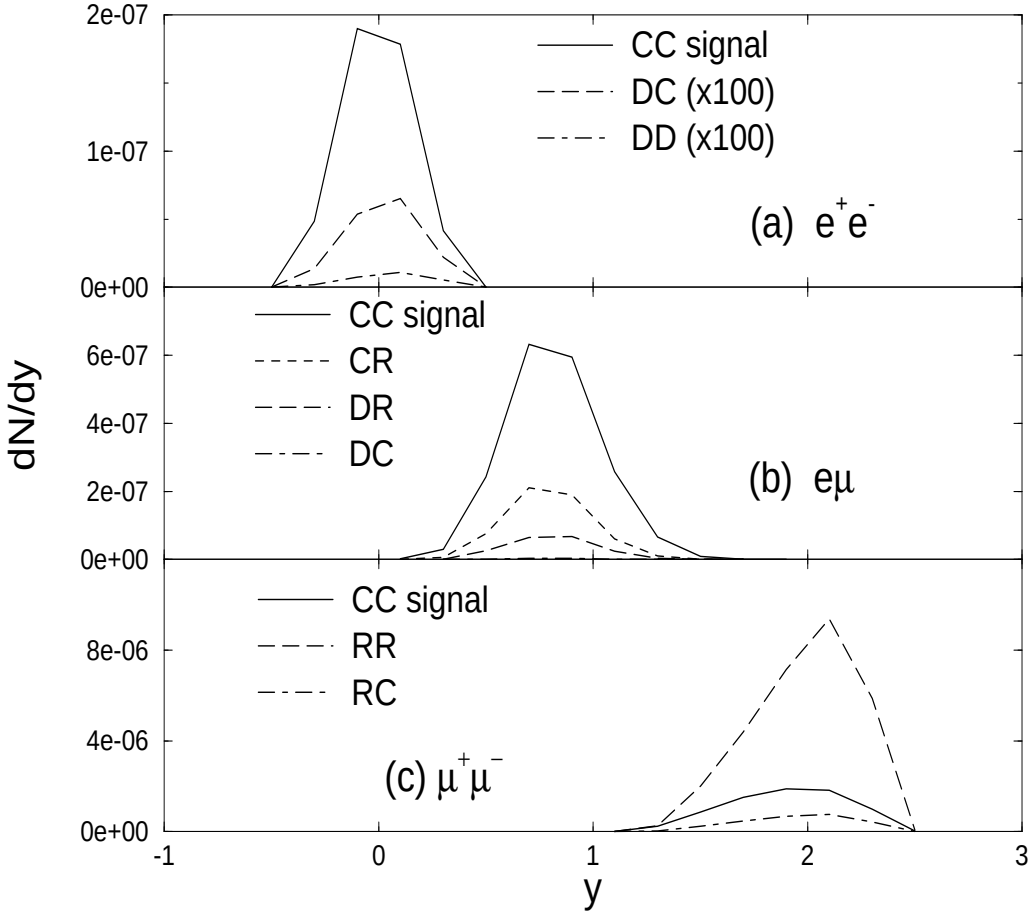

Figure 4.9: Charm signal and backgrounds entering the detector as a function of the lepton pair-rapidity y.

from opposite-sign pairs to suppress the backgrounds. The efficiency of the like-sign subtraction depends on the charge and isospin asymmetry of the collision. With the help of like-sign subtraction, the $e\mu$ and $\mu\mu$ signal could be observed.

4.9 Single Inclusive Lepton Spectrum

The kinematics here are considerably less restricted, so the relation between the kinematic variable E, η for the single lepton and the gluon Bjorken variable x_A are more indirect. Thus, the single inclusive lepton spectrum reflects the nuclear shadowing effects less effectively. For the signal from open charm decay, the ratios of electron pseudo-rapidity ($\eta = 1/2 \ln[(1 + \cos\theta)/(1 - \cos\theta)]$) distributions $dN/d\eta$ from the two shadowing cases over those from the non-shadowing case are shown in Figure 4.10. The solid(dashed) curve represents HIJING(Eskola)'s shadowing.

Also the signal-to-background ratio in the detector is not as good as that for the lepton pair case. The estimated ratio is approximately 3 for single electrons and 1/22 for single muons (with HIJING's shadowing), compared with about 260 for ee, 2.5 for $e\mu$ and 1/4 for $\mu\mu$. Given the above small signal-to-background ratio, it is difficult to observe single muons. Since the single electron and muon spectrum cover pair-rapidity ranges around 0 and $0, 2$ respectively, we can only observe mid-rapidity single electrons. While for the the three pair spectra, they cover rapidities around 0, 1 and 2, and have reasonable signal-to-background ratio. So we conclude that although

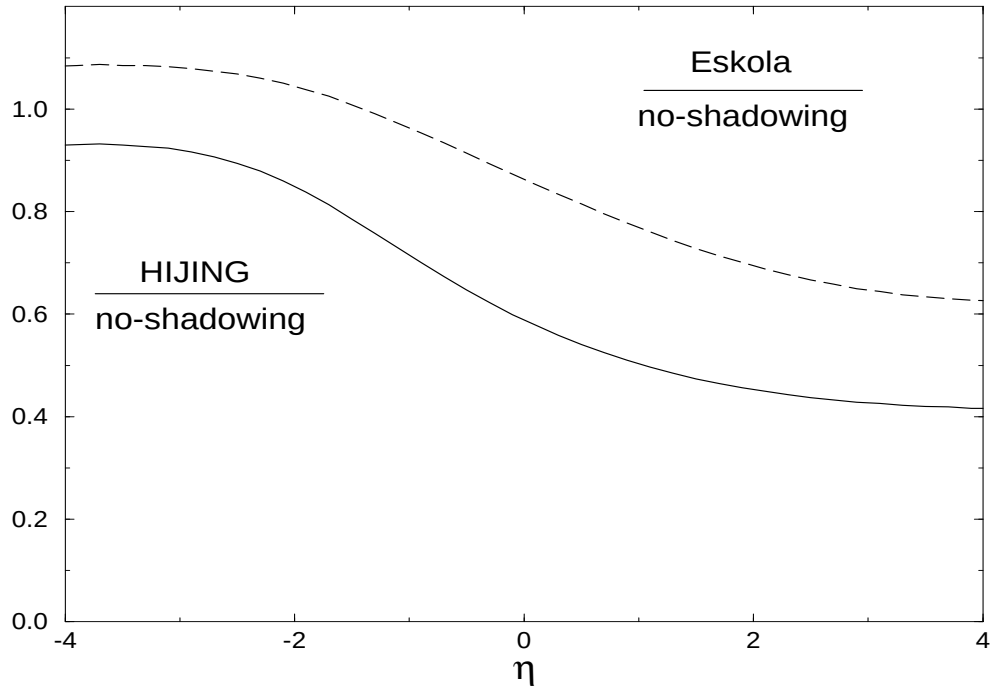

Figure 4.10: Ratios of single electron signals from the two shadowing cases over those from the non-shadowing case as a function of the pseudo-rapidity η.

the single electron spectrum signal could be seen as an easy initial measure of shadowing effects, the shadowing effects will be seen much more clearly in the lepton pair spectrum than in the single spectrum.

4.10 Cronin Effect and Energy Loss

Cronin effect and energy loss will weaken the back-to-back type of correlation between the two charm mesons in the pair, and thus weaken the scaling behavior among the dilepton $dN/dMdy$ ratio curves showed in Figure 4.5. However, in the following they are estimated to lead to distortions of up to 10% in $p + A$ collisions at RHIC energies.

From studies of the nuclear dependence of transverse momenta of J/ψ production, the typical increment, $\delta p_\perp^2(A)$, due to multiple collisions is limited to ~ 0.34 GeV^2 even for the heaviest nuclei [183]. This momentum spread is shared between the c and $\bar{c}$, and distributed approximately as

$$g(\delta p_\perp) = e^{-\delta p_\perp^2/\Delta^2}/\pi\Delta^2 \quad , \tag{4.45}$$

where $\Delta^2 \sim 0.17$GeV^2. For energy loss, we assume that the charm quark loses an energy δE in the lab frame, and the charm quark $p_\perp$ is reduced by $(1-\epsilon)$, where

$$\epsilon = \delta E/[m_\perp \sinh(y + y_0)] \quad . \tag{4.46}$$

Combining these two effects, we may write for the charm quark that the final transverse momentum is

$$\vec{p}_\perp = (\vec{p_\perp^{ini}} + \vec{\delta} p_\perp)(1-\epsilon) \quad . \tag{4.47}$$

Assuming that the D-meson spectrum without these two effects can be expressed as

$$F(p_\perp) \equiv d^2N/dm_\perp^2 \quad , \tag{4.48}$$

then it becomes

$$F'(p_\perp) = \int F(p_\perp^{ini}) g(\delta p_\perp) d\vec{\delta} p_\perp \quad . \tag{4.49}$$

with

$$F(p_\perp) \propto e^{-\alpha p_\perp} \quad ; \alpha \simeq 1.3 \text{ GeV}^{-1} \tag{4.50}$$

from HIJING. Expanding the convolution to lowest order, the relative change of the D-meson spectrum is given by

$$F'(p_\perp)/F(p_\perp) \simeq 1 - \alpha p_\perp \epsilon + \alpha^2 \Delta^2/4 \quad , \tag{4.51}$$

This is also the relative change of the $c\bar{c}$ pair spectrum when $M_{c\bar{c}} = 2m_\perp$ in case of $y_1 = y_2$, $p_{\perp 1} = p_{\perp 2}$. Take

$$m_\perp \sim 3\text{GeV} \quad , \tag{4.52}$$

$$\delta E = 10\text{GeV} \quad , \tag{4.53}$$

$$\cosh y_0 \simeq 100 \quad , \tag{4.54}$$

then the relative change in the pair spectrum is estimated to be

$$F'(p_\perp)/F(p_\perp) \simeq 1 \ - 0.1(e^{-y} - 1) \quad . \tag{4.55}$$

4.11 Effect of Energy Loss in $A + A$ Collisions

In heavy ion experiments, dileptons from a few GeV region were suggested to be possible signals of the quark-gluon plasma; however, they were later claimed [88] to be dominated by the dileptons from open charm decay. Nevertheless, it has been suggested recently [89] that energy loss is an important factor which could soften greatly the dilepton spectrum from open charm decays.

In $A + A$ collisions, open charm must pass through the dense parton medium formed after the initial collision; it will therefore lose a certain amount of energy, typically 2GeV/fm. Moreover, the two charm mesons in a pair tend to have opposite azimuthal angles, so the probability that both of them can escape without substantial energy loss is very small. Considering that we are interested in dileptons with energies of a few GeV, the dilepton spectrum from correlated open charm (also open bottom) decay will be greatly softened compared to the conclusion in [88], and is possibly comparable to the signal from the quark-gluon plasma.

In order to get a better understanding of the magnitude of the softening of the charm dilepton signal, we can take into account the following facts: in a finite size nucleus, partons lose energy in finite number of collisions, not by the simple linear energy loss formula. Therefore the energy loss has more fluctuations than in the linear assumption case. Secondly, the dilepton $p_\perp$ spectrum depends crucially on the angular distribution, thus it is important to calculate the open charm production to the next-to-leading order in order

to take into account the fact that the open charm pair are not always back-to-back azimuthally.

In the mid-rapidity region in $p+A$ collisions, there are much fewer partons than in the $A+A$ case, and the most energy loss occurs in the target rapidity region where $y << 0$. This energy loss effect was estimated in the above chapter 4.10 and shown to be very small.

4.12 Discussion and Summary

We use Delta function as the charm quark fragmentation function to D meson. The above analysis depends on the validity of this basic assumption regarding the hard fragmentation of charm quarks. Although this assumption is being supported by the low energy pp data [141, 179], it should be checked explicitly via the single inclusive measurements of D production at RHIC.

In this study, we included only the geometrical part of the experimental acceptance in our calculations. In order to get the detailed background spectra for photon conversions, leakage muons, etc, the full detector simulation should be carried out. Since the geometry is asymmetric for $p + Au$ collisions, energy loss will shift the rapidity of the particles toward the target rapidity region, which is an additional shift to the larger rapidity shift due to shadowing effects. Jet quenching could also change the rapidity distribution slightly if the nuclear density is high, particularly for the high $p_\perp$ part. We must separate contributions due to other effects such as energy loss in order

to clearly observe the interesting shadowing curves shown in Figure 4.5.

We choose $p + Au$ since it has much smaller combinatoric background. It also demonstrates the shadowing effects more clearly in the $dN/dy(M)$ spectrum for the lepton pairs as shown in Figure 4.5.

In summary, we calculated the lepton pair spectra from open charm decay in two different shadowing scenarios. By scaling the ratios for different mass ranges according to eq.(4.39), we showed that the dilepton rapidity dependence of those ratios on x_A reproduces well the underlying gluon shadowing function defined in eq.(4.1). Finally we showed that the measurements required to extract the gluon shadowing are experimentally feasible at RHIC. The signal can be seen in $p + Au$ collisions, some even before using like-sign subtraction.

We conclude by emphasizing the importance of determining gluon shadowing in $p + A$ to fix theoretically the initial conditions in $A + A$. In $A + A$ the open charm decay is regarded as an annoyingly large background that must be subtracted to uncover the thermal signal. In $p + A$ that background becomes the signal needed to determine the incident gluon flux in $A + A$. The continuum charm dileptons in $p + A$ at RHIC are likely to provide a unique source of information on the low x_A nuclear gluon structure at least until HERA is capable of accelerating heavy nuclei.

Chapter 5

Outlook

In this thesis work, we have investigated the open charm production in nuclear collisions and whether it can serve as a probe of the quark-gluon plasma phase. We found that the additional open charm production from the pre-equilibrium stage is negligible if we allow strong correlations between the space-time coordinate and the momentum of minijet partons. Contrary to an earlier result, which claimed an enormous enhancement in the open charm production given the formation of the quark-gluon plasma, we showed that open charm is not likely to be a good probe of the plasma phase formed in relativistic heavy ion collisions.

We then proposed to use the open charm as a probe of the initial parton structure function in nuclei, and thus turned our attention from probing the quark-gluon plasma to probing the nuclear shadowing effect. The dominance of the open charm in lepton-pair spectra with a few GeV energy makes it possible to observe the open charm via high-mass lepton-pairs in $p + A$ collisions. To make a better connection with ongoing experimental projects, we

then estimated the signal-to-background ratio for the proposed lepton-pair measurements for the PHENIX detector at RHIC, and showed that these measurements are feasible.

In our study, we find that the pre-equilibrium charm production depends strongly on the space-time and momentum correlation of minijet partons. Our model is a minimal modification of the Bjorken correlation by taking into account the uncertainty principle. The exact strength of the correlation of minijet partons is yet an open question, and needs to be further investigated.

The assumption on the hard fragmentation function of charm quarks needs to be tested in high energy hadroproductions. The latest Fermilab data support this assumption. However, we need to further study the dependence of the hardness of fragmentations on both the beam atomic number, A, and the beam energy.

Charmonium productions provide us with very interesting experimental data. The uncertainty from the fudge factors needs to be addressed in order to calculate the absolute yield of charmonium states.

Another open problem that needs future investigation is the effect of the energy loss. It has been suggested that, due to the energy loss of charm quarks, the large initial open charm production could be kinematically shifted to the lower-mass region in dilepton spectra in $A + A$ collisions. To evaluate this possibility, parton cascade simulations will be needed. Such models are currently being formulated, and it will soon be possible to carry out detailed numerical simulations. The energy-loss effect could have interesting

consequences on the PHENIX search for direct thermal dileptons. In addition, a detailed analysis on dilepton spectra from open charm decays in $A + A$ collisions could provide information on the still-controversial energy-loss mechanism in the QGP.

Appendix

In the appendix, we shall consider the impact-parameter-dependence of nuclear shadowing effects.

For the shadowing used in HIJING model [70], the density function is:

$$\Gamma_{a/A}(x, Q^2, \vec{r}) = T_A(\vec{r}) f_{a/N}(x, Q^2) S_A(x, \vec{r}) \ , \tag{A.1}$$

where $f_{a/N}(x, Q^2)$ is the parton structure function in a nucleon, $\vec{r}$ is the transverse vector of parton a inside nucleus A, $T_A(\vec{r})$ is the transverse density function of the nucleus, and for a uniform-sphere nucleus

$$T_A(\vec{r}) = (3A/2\pi R_A^2)\sqrt{1 - r^2/R_A^2} \ . \tag{A.2}$$

$S_A(x, \vec{r})$ describes shadowing effects with the following parameterization, which is independent of the parton species and the Q^2 scale:

$$\begin{aligned} S_A(x, \vec{r}) &\equiv \frac{f_{a/A}(x, \vec{r})}{A f_{a/N}(x)} \\ &= 1 + 1.19 \ln^{1/6} A [x^3 - 1.5(x_0 + x_L)x^2 + 3x_0 x_L x] \\ &\quad - \left[\alpha_A(\vec{r}) - \frac{1.08(A^{1/3} - 1)}{\ln(A+1)}\sqrt{x}\right] e^{-x^2/x_0^2} \ , \end{aligned} \tag{A.3}$$

where

$$x_0 = 0.1, \ \ x_L = 0.7 \ , \tag{A.4}$$

$$\alpha_A(\vec{r}) = 0.1(A^{1/3} - 1)\frac{4}{3}\sqrt{1 - r^2/R_A^2} \ . \tag{A.5}$$

For central $p + Au$ collisions, we should take the average over $r \leq r_0 (\sim$

$1.12fm$), where $r_0 \ll R_A(\sim A^{1/3}r_0)$. Therefore

$$S_A(x,\vec{r}) \simeq S_A(x,\vec{0}) \ , \tag{A.6}$$

and the integral over the transverse vector in Equation (4.28) gives the following factor:

$$\int d^2r T_p(\vec{r}) T_{Au}(\vec{r}) S_{a/p}(x,\vec{r}) S_{Au}(x,\vec{r}) \simeq \frac{3A^{1/3}}{2\pi r_0^2} S_{Au}(x,\vec{0}) \ . \tag{A.7}$$

Note that there is no shadowing on the proton projectile in $p+Au$ collisions.

The other shadowing functions from Eskola [166] depend on Q^2 and are also different for valence quarks, sea quarks and gluons. The density function is:

$$\begin{aligned} \Gamma_{a/A}(x,Q^2,\vec{r}) &= T_A(\vec{r}) f_{a/N}(x,Q^2) \\ &\quad \times \left\{ 1 - \frac{AT_A(\vec{r})}{\int d^2r T_A^2(\vec{r})} \left[1 - S_{a/A}(x,Q^2) \right] \right\} \ . \end{aligned} \tag{A.8}$$

If we average over the impact parameter, we get

$$\begin{aligned} f_{a/A}(x,Q^2) &\equiv \int d^2r \Gamma_{a/A}(x,Q^2,\vec{r}) \\ &= A f_{a/N}(x,Q^2) S_{a/A}(x,Q^2) \ , \end{aligned} \tag{A.9}$$

which is precisely the definition of the impact-parameter-independent shadowing function $S_{a/A}(x,Q^2)$. For central $p+Au$ collisions, the integral over the transverse vector yields

$$\begin{aligned} &\int d^2r T_p(\vec{r}) T_{Au}(\vec{r}) \left\{ 1 - \frac{AT_{Au}(\vec{r})}{\int d^2r T_{Au}^2(\vec{r})} \left[1 - S_{b/Au}(x,Q^2) \right] \right\} \\ &\simeq \frac{3A^{1/3}}{2\pi r_0^2} \left[\frac{4}{3} S_{b/Au}(x,Q^2) - \frac{1}{3} \right] \ . \end{aligned} \tag{A.10}$$

From equations (A.7) and (A.10), the overall shadowing factor for central $p + Au$ collisions is

$$S_{Au}(x, \vec{0}) \tag{A.11}$$

for HIJING's case, and

$$[4/3 S_{b/Au}(x, Q^2) - 1/3] \tag{A.12}$$

for Eskola's case.

References

[1] J.C. Collins and M.J. Perry, Phys. Rev. Lett. 34, 1353 (1975).

[2] M.B. Kislinger and P.D. Morley, Phys. Rev. D 13, 2765 (1976);
P.D. Morley and M.B. Kislinger, Phys. Rep. 51, 63 (1979).

[3] D.J. Gross and F. Wilczek, Phys. Rev. Lett. 30, 1343 (1973);
H.D. Politzer, Phys. Rev. Lett. 30, 1346 (1973).

[4] G. Baym and C. Pethick, Ann. Rev. Astron. Astrophys. 17, 415 (1979).

[5] J.H. Applegate, Nucl. Phys. A 527, 195c (1991).

[6] E.V. Shuryak, Phys. Lett. B 78, 150 (1978); Sov. J. Nucl. Phys. 28, 408 (1978).

[7] T.D. Lee, Rev. Mod. Phys. 47, 267 (1975);
T.D. Lee and G.C. Wick, *Mesons in Nuclei*, eds. M. Rho and D. Wilkinson (1979), p867.

[8] A.B. Migdal, Rev. Mod. Phys. 50, 107 (1978).

[9] S. Nagamiya and M. Gyulassy, *Advances In Nuclear Physics*, eds. J.W. Negele and E. Vogt (1982), Vol. 13, p201.

[10] Proc. Quark Matter'88, Lenox, Massachusetts, eds. G. Baym et al. (1988).

[11] Proc. Quark Matter'95, Monterey, California, eds. A.M. Poskanzer et al. (1995).

[12] Proc. Quark Matter'96, Heidelberg, Germany, eds. P. Braun-Munzinger et al. (1996).

[13] E. Shuryak, Phys. Rep. 61, 71 (1980); Phys. Rept. 115, 151 (1984).

[14] T.D. Lee and G.C. Wick, Phys. Rev. D 9, 2291 (1974);
T.D. Lee, Nucl. Phys. A 590, 11c (1995).

[15] B. Svetitsky and L.G. Yaffe, Phys. Rev. D 26, 963 (1982);
Nucl. Phys. B 210, 423 (1982).

[16] F. R. Brown, N.H. Christ, Y.F. Deng, M.S. Gao and T.J. Woch, Phys. Rev. Lett. 61, 2058 (1988);
R.V. Gavai, F. Karsch and B. Petersson, Nucl. Phys. B 322, 738 (1989).

[17] F. Green and F. Karsch, Nucl. Phys. B 238, 297 (1984).

[18] G. 't Hooft, Phys. Rev. Lett. 37, 8 (1976); Phys. Rev. D 14, 3432 (1976).

[19] S.L. Adler, Phys. Rev. D 177, 2426 (1969);
J.S. Bell and R. Jackiw, Nuovo Cimento 60, 47 (1969).

[20] C. Callan, R. Dashen and D.J. Gross, Phys. Lett. B 63, 334 (1976).

[21] R.D. Pisarski and F. Wilczek, Phys. Rev. D 29, 338 (1984).

[22] J.I. Kapusta, Nucl. Phys. B 148, 461 (1979);
T. Toimela, Phys. Lett. B 124, 407 (1983);
for the other three higher order coefficients, see P. Arnold and C.X. Zhai, Phys. Rev. D 50, 7603 (1994); Phys. Rev. D 51, 1906 (1995);
C.X. Zhai and B. Kastening, preprint hep-ph/9507380.

[23] M. Gyulassy, Prog. in Part. and Nucl. Phys. 15, 403 (1985).

[24] Raymond Brock et al., CTEQ Collab., Rev. Mod. Phys. 67, 157 (1995).

[25] A.D. Linde, Phys. Lett. B 96, 289 (1980).

[26] K.G. Wilson, Phys. Rev. D 10, 2445 (1974).

[27] M. Creutz, Phys. Rev. D 21, 2308 (1980).

[28] J. Kogut and L. Susskind, Phys. Rev. D 11, 395 (1975).

[29] F.R. Brown, F.P. Butler, H. Chen, N.H. Christ, Z. Dong, W. Schaffer, L.I. Unger and A. Vaccarino, Phys. Rev. Lett. 65, 2491 (1990).

[30] Y. Iwasaki, K. Kanaya, T. Yoshie, T. Hoshino, T. Shirakawa, Y. Oyanagi, S. Ichii and T. Kawai, Phys. Rev. Lett. 67, 3343 (1991).

[31] F. Karsch and E. Laermann, Phys. Rev. D 50, 6954 (1994);
C. Bernard, T. Blum, C. DeTar, S. Gottlieb, K. Rummukainen,

U.M. Heller, J. Hetrick, D. Toussaint and R.L. Sugar, preprint hep-lat/9605028.

[32] G. Boyd, J. Engels, F. Karsch, E. Laermann, C. Legeland, M. Lutgemeier and B. Petersson, Nucl. Phys. B 469, 419 (1996).

[33] C. Bernard, T. Blum, C.E. DeTar, S. Gottlieb, U.M. Heller, J.E. Hetrick, L. Karkkainen, C. McNeile, K. Rummukainen, R.L. Sugar, D. Toussaint and M. Wingate, preprint hep-lat/9608026.

[34] U. Heller and F. Karsch, Nucl. Phys. B 251, 254 (1985);
B. Beinlich, F. Karsch and E. Laermann, Nucl. Phys. B 462, 415 (1996).

[35] G. Cella, G. Curci, R. Tripiccione and A. Viceré, Phys. Rev. D 49, 511 (1994);
G. Cella, G. Curci, A. Viceré and B. Vigna, Phys. Lett. B 333, 457 (1994).

[36] I.V. Arsenin et al., Nucl. Phys. B (Proc. Suppl.) 42, 902 (1995).

[37] K.J. Eskola, Z. Phys. C 51, 633 (1991).

[38] K.J. Eskola and M. Gyulassy, Phys. Rev. C 47, 2329 (1993);
M. Gyulassy, K.J. Eskola, A.V. Selikhov and X.-N. Wang, *in* CCAST Symposium Proceedings, Vol 10, eds. Y. Pang, J. Qiu, Z. Qiu (Gordon and Breach, Amsterdam, 1994) p393.

[39] S. Nagamiya et al., PHENIX Conceptual Design Report (1993) (unpublished);
on internet see *http://rsgi01.rhic.bnl.gov/phenix/phenix_home.html*. Recently a second muon arm is proposed.

[40] J. Schukraft et al., Nucl. Phys. A 566, 311c (1994).

[41] A.M. Rossi et al., Nucl. Phys. B 84, 269 (1975);
W. Thome et al., Nucl. Phys. B 129, 365 (1977);
F. Abe et al., Phys. Rev. D 41, 2330 (1990);
U. Heinz, P. Koch and B. Friman, *Aachen ECFA Workshop*, (1990), p1079.

[42] J.D. Bjorken, Phys. Rev. D 27, 140 (1983).

[43] T.S. Biró, E. van Doorn, B. Müller, M.H. Thoma and X.-N. Wang, Phys. Rev. C 48, 1275 (1993).

[44] K. Geiger, Phys. Rev. D 48, 4129 (1993).

[45] E. Shuryak, Phys. Rev. Lett. 68, 3270 (1992).

[46] R. Baier, Yu.L. Dokshitser, S. Peigné and D. Schiff, Phys. Lett. B 345, 277 (1995);
R. Baier, Yu.L. Dokshitser, A.H. Mueller, S. Peigné and D. Schiff, preprint hep-ph/9604327; hep-ph/9607355; hep-ph/9608322.

[47] T.S. Biró, B. Müller and X.-N. Wang, Phys. Lett. B 283, 171 (1992).

[48] P. Danielewicz and M. Gyulassy, Phys. Rev. D 31, 53 (1985).

[49] G. Baym, H. Monien, C.J. Pethick and D.G. Ravenhall, Phys. Rev. Lett. 64, 1867 (1990).

[50] L. Xiong and E. Shuryak, Phys. Rev. C 49, 2203 (1994).

[51] L.D. Landau and I.Ya. Pomeranchuk, Dokl. Akad. Nauk SSSR, 92, 535 (1953);
A.B. Migdal, Phys. Rev. 103, 1811 (1956).

[52] M. Gyulassy and X.-N. Wang, Nucl. Phys. B 420, 583 (1994);
X.-N. Wang, M. Gyulassy and M. Plümer, Phys. Rev. D 51, 3436 (1995).

[53] T. Matsui, B. Svetitsky and L.D. McLerran, Phys. Rev. D 34, 783 (1986); D 37, 844(E) (1988).

[54] P. Lévai, B. Müller and X.-N. Wang, Phys. Rev. C 51, 3326 (1995).

[55] X.-N. Wang, preprint hep-ph/9605214.

[56] L.P. Csernai, *Introduction to Relativistic Heavy Ion Collisions*, (John Wiley & Sons, 1994), p 86.

[57] L.P. Csernai and J.I. Kapusta, Phys. Rep. 131, 223 (1986).

[58] E.L. Feinberg, Nuovo Cimento 34A, 391 (1976);
J.F. Owens, Rev. Mod. Phys. 59, 465 (1987).

[59] E. Shuryak and L. Xiong, Phys. Rev. Lett. 70, 2241 (1993).

[60] K. Kajantie, J. Kapusta, L. McLerran and A. Mekjian, Phys. Rev. D 34, 2746 (1986).

[61] T. Matsui and H. Satz, Phys. Lett. B 178, 416 (1986).

[62] B. Müller and X.-N. Wang, Phys. Rev. Lett. 68, 2437 (1992).

[63] G. Agakichev et al., CERES Collab., Phys. Rev. Lett. 75, 1272 (1995).

[64] J.P. Wurm, CERES Collab., Nucl. Phys. A 590, 103c (1995).

[65] M. Gonin, NA50 Collab., Proc. Quark Matter'96, Heidelberg, Germany, eds. P. Braun-Munzinger et al. (1996).

[66] A. Bussière, NA38 Collab., Proc. Quark Matter'87, Z. Phys. C 38, 117 (1988); Phys. Lett. B 220, 471 (1989).

[67] S. Gupta and H. Satz, Z. Phys. C 55, 391 (1992).

[68] D. Kharzeev and H. Satz, Phys. Lett. B 366, 316 (1996).

[69] C. Baglin et al., NA38 Collab., Phys. Lett. B 270, 105 (1991);
S. Ramos et al., NA38 Collab., Proc. Quark Matter'95, Nucl. Phys. A 590, 117c (1995).

[70] X.-N. Wang and M. Gyulassy, Phys. Rev. D 44, 3501 (1991); D 45, 844 (1992).

[71] K. Werner, Phys. Lett. B 208, 520 (1988).

[72] S.D. Drell and T.M. Yan, Phys. Rev. Lett. 24, 181 (1970); Ann. Phys. 66, 578 (1971).

[73] R.A. Salmeron, Nucl. Phys. B 389, 301 (1993).

[74] C. Baglin et al., NA38 Collab., Phys. Lett. B 345, 617 (1995).

[75] J.-P. Blaizot and J.-Y. Ollitrault, preprint hep-ph/9606289;
D. Kharzeev and H. Satz, Proc. Quark Matter'96, opcit.

[76] Figure 1.10 is taken from the NA50 experiment internet site at *http://infodan.in2p3.fr/qgp/cern/www_fleuret/fleuret.html.*

[77] S. Gavin and R. Vogt, preprint hep-ph/9606460.

[78] S. Gavin, H. Satz, R.L. Thews and R. Vogt, Z. Phys. C 61, 351 (1994);
S. Gavin, Nucl. Phys. A 566, 383c (1994).

[79] S. Gavin, M. Gyulassy and A. Jackson, Phys. Lett. B 207, 257 (1988).

[80] D. Kharzeev and H. Satz, Phys. Lett. B 334, 155 (1994).

[81] M.B. Einhorn and S.D. Ellis, Phys. Rev. D 12, 2007 (1975);
H. Fritzsch, Phys. Lett. B 67, 217 (1977);
M. Glück, J.F. Owens and E. Reya, Phys. Rev. D 17, 2324 (1978);
J. Babcock, D. Sivers and S. Wolfram, Phys. Rev. D 18, 162 (1978).

[82] R. Gavai, D. Kharzeev, H. Satz, G.A. Schuler, K. Sridhar and R. Vogt, Int. J. Mod. Phys. A 10, 3043 (1995).

[83] C.H. Chang, Nucl. Phys. B 172, 425 (1980);
E.L. Berger and D. Jones, Phys. Rev. D 23, 1521 (1981);
R. Baier and R. Rückl, Phys. Lett. B 102, 364 (1981); Z. Phys. C 19, 251 (1983).

[84] G.T. Bodwin, E. Braaten and G.P. Lepage, Phys. Rev. D 46, 1914 (1992).

[85] G.T. Bodwin, E. Braaten, T.C. Yuan and G.P. Lepage, Phys. Rev. D 46, 3703 (1992).

[86] E. Braaten and S. Fleming, Phys. Rev. Lett. 74, 3327 (1995).

[87] G.T. Bodwin, E. Braaten and G.P. Lepage, Phys. Rev. D 51, 1125 (1995).

[88] R. Vogt, B.V. Jacak, P.L. McGaughey and P.V. Ruuskanen, Phys. Rev. D 49, 3345 (1994).

[89] E.V. Shuryak, preprint nucl-th/9605011.

[90] I. Tserruya, Nucl. Phys. A 590, 127c (1995).

[91] M. Masera, HELIOS/3 Collab., Nucl. Phys. A 590, 93c (1995).

[92] R. Pisarski, Phys. Lett. B 110, 155 (1982).

[93] A. Shor, Phys. Rev. Lett. 54, 1122 (1985).

[94] G.Q. Li, C.M. Ko and G.E. Brown, Phys. Rev. Lett. 75, 4007 (1995).

[95] G.Q. Li, C.M. Ko and G.E. Brown, preprint nucl-th/9608040.

[96] T. Hatsuda and S.H. Lee, Phys. Rev. C 46, 34 (1992).

[97] W. Cassing, W. Ehehalt and C.M. Ko, Phys. Lett. B 363, 35 (1995).

[98] W. Cassing, W. Ehehalt and I. Kralik, Phys. Lett. B 377, 5 (1996).

[99] M. Herrmann, B.L. Friman and W. Nörenberg, Nucl. Phys. A 560, 411 (1993).

[100] F. Halzen and D.M. Scott, Phys. Rev. Lett. 40, 1117 (1978);
F. Halzen and D.M. Scott, Phys. Rev. D 18, 3378 (1978);
L. Cormell and J.F. Owens, Phys. Rev. D 22, 1609 (1980).

[101] R. Santo et al., WA80 Collab., Nucl. Phys. A 566, 61c (1994);
T.C. Awes et al., WA80 Collab., Nucl. Phys. A 590, 81c (1995).

[102] D.K. Srivastava and B. Sinha, Phys. Rev. Lett. 73, 2421 (1994).

[103] A. Dumitru, U. Katscher, J.A. Maruhn, H. Stocker, W. Greiner and D.H. Rischke, Phys. Rev. C 51, 2166 (1995).

[104] X.-N. Wang, Z. Huang and I. Sarcevic, preprint hep-ph/9605213.

[105] J. Kogut et al., Phys. Rev. Lett. 50, 393 (1983).

[106] A.A. Anselm and M.G. Ryskin, Phys. Lett. B 266, 482 (1991);
J.P. Blaizot and A. Krzywicki, Phys. Rev. D 46, 246 (1992).

[107] K. Rajagopal and F. Wilczek, Nucl. Phys. B 399, 395 (1993).

[108] K. Rajagopal and F. Wilczek, Nucl. Phys. B 404, 577 (1993).

[109] C.M.G. Lattes, Y. Fujimoto and S. Hasegawa, Phys. Rep. 65, 151 (1980).

[110] M. Asakawa, Z. Huang and X.-N. Wang, Phys. Rev. Lett. 74, 3126 (1995).

[111] S. Gavin and B. Müller, Phys. Lett. B 329, 486 (1994).

[112] T. Csörgő, M. Asakawa, J. Helgesson and B. Lörstad, preprint nucl-th/9506006.

[113] J.D. Bjorken, K.L. Kowalski and C.C. Taylor, preprint hep-ph/9309235.

[114] J. Barrette et al., E877 Collab., Phys. Rev. Lett. 73, 2532 (1994).

[115] H.A. Gustafsson et al., Phys. Rev. Lett. 52, 1590 (1984).

[116] S. Voloshin and Y. Zhang, preprint hep-ph/9407282.

[117] P. Danielewicz and M. Gyulassy, Phys. Lett. B 129, 283 (1983).

[118] T. Hemmick, E877 Collab., Proc. Quark Matter'96, Heidelberg, Germany, eds. P. Braun-Munzinger et al. (1996).

[119] R. Mattiello, A. Jahns, H. Sorge, H. Stöcker and W. Greiner, Phys. Rev. Lett. 74, 2180 (1995).

[120] D.E. Kahana, Y. Pang and E. Shuryak, preprint nucl-th/9604008.

[121] D.H. Rischke and M. Gyulassy, preprint nucl-th/9606039.

[122] M. Gyulassy, S.K. Kauffmann and L.W. Wilson, Phys. Rev. C 20, 2267 (1979).

[123] S. Pratt, Phys. Rev. Lett. 53, 1219 (1986).

[124] R. Hanbury-Brown and R.Q. Twiss, Nature 178, 1046 (1956).

[125] S.S. Padula and M. Gyulassy, Nucl. Phys. B 339, 378 (1990).

[126] S. Chapman, J.Rayford Nix and U. Heinz, Phys. Rev. C 52, 2694 (1995).

[127] G. Bertsch, M. Gong and M. Tohyama, Phys. Rev. C 37, 1896 (1988).

[128] H. Beker et al., NA44 Collab., Nucl. Phys. A 566, 115c (1994);
D. Ferenc, Proc. Quark Matter'96, Heidelberg, Germany, eds. P. Braun-Munzinger et al. (1996).

[129] M. Gyulassy, D.H. Rischke and B. Zhang, preprint nucl-th/9606045.

[130] J.J. Aubert et al., European Muon Collab., Phys. Lett. B 123, 275 (1983);
M. Arneodo et al., EM Collab., Nucl. Phys. B 333, 1 (1990);
P. Amaudruz et al., NM Collab., Z. Phys. C 51, 387 (1991);
M.R. Adams et al., E665 Collab., Phys. Rev. Lett. 68, 3266 (1992).

[131] A.H. Mueller and J. Qiu, Nucl. Phys. B 268, 427 (1986);
J. Collins and J. Kwiecinski, Nucl. Phys. B 335, 89 (1990).

[132] Z. Lin and M. Gyulassy, Phys. Rev. C 51, 2177 (1995); C 52, 440(E) (1995).

[133] Z. Lin and M. Gyulassy, Phys. Rev. Lett. 77, 1222 (1996).

[134] K.J. Eskola, J. Qiu and X.-N. Wang, Phys. Rev. Lett. 72, 36 (1994).

[135] X.-N. Wang, M. Gyulassy, Phys. Rev. Lett. 68, 1480 (1992).

[136] B.L. Combridge, Nucl. Phys. B 151, 429 (1979).

[137] J.C. Collins, D.E. Soper and G. Sterman, Nucl. Phys. B 263, 37 (1986).

[138] R.K. Ellis, FERMILAB-CONF-86/35-T, Apr 1986. 17pp.

[139] E. Hoffmann and R. Moore, Z. Phys. C 20, 71 (1983).

[140] G. Ingelman, L. Jönsson and M. Nyberg, Phys. Rev. D 47, 4872 (1993).

[141] R. Vogt, S.J. Brodsky and P. Hoyer, Nucl. Phys. B 383, 643 (1992); R. Vogt and S.J. Brodsky, Nucl. Phys. B 438, 261 (1995).

[142] S.J. Brodsky, P. Hoyer, A.H. Mueller and W.K. Tang, Nucl. Phys. B 369, 519 (1992).

[143] M. Glück, E. Reya and A. Vogt, Z. Phys. C 48, 471 (1990).

[144] D.W. Duke and J.F. Owens, Phys. Rev D 30, 49 (1984).

[145] A.D. Martin, W.J. Stirling and R.G. Roberts, Phys. Rev. D 50, 6734 (1994).

[146] H.L. Lai, J. Huston, S. Kuhlmann, F. Olness, J. Owens, D. Soper, W.K. Tung and H. Weerts, preprint hep-ph/9606399.

[147] P. Nason, S. Dawson and R.K. Ellis, Nucl. Phys. B 303 (1988) 607; Nucl. Phys. B 327, 49 (1989).

[148] W. Beenakker, H. Kuijf, W.L. van Neerven and J. Smith, Phys. Rev. D 40, 54 (1989);
W. Beenakker, W.L. van Neerven, R. Meng, G. Schuler and J. Smith, Nucl. Phys. B 351, 507 (1991).

[149] E.L. Berger, *Proc. Advanced Workshop on QCD Hard Processes*, (St. Croix, 1988).

[150] E.L. Berger and R. Meng, Phys. Rev. D 46, 169 (1992).

[151] I. Sarcevic and P. Valerio, Phys. Lett. B 338, 426 (1994).

[152] R. Vogt, preprint hep-ph/9510293.

[153] S. Aoki et al., Phys. Lett. B 224, 441 (1989).

[154] A.T. Goshaw, *Proc. Advanced Workshop on QCD Hard Processes*, (St. Croix, 1988).

[155] M. Aguilar-Benitez et al., Phys. Lett. B 189, 476 (1987).

[156] R. Ammar et al., Phys. Rev. Lett. 61, 2185 (1988).

[157] K. Kodama et al., Phys. Lett. B 263, 573 (1991).

[158] M.J. Leitch et al., Phys. Rev. Lett. 72, 2542 (1994).

[159] S.P.K. Tavernier, Rep. Prog. Phys. 50, 1439 (1987).

[160] C. Albajar et al., UA1 Collab., Phys. Lett. B 256, 121 (1991).

[161] M.E. Duffy et al., Phys. Rev. Lett. 55, 1816 (1985);
H. Cobbaert et al., Phys. Lett. B 206, 546 (1987).

[162] G.A. Alves et al., E769 Collab., Phys. Rev. Lett. 70, 722 (1993).

[163] J. Qiu, Phys. Lett. B 191, 182 (1987).

[164] K. Goulianos, *Physics Simulations at High Energies*, eds. V. Barger et al., (World Scientific, Singapore, 1987).

[165] L. Combridge, J. Kripfganz and J. Ranft, Phys. Lett. 70, 234 (1977).

[166] K.J. Eskola, Nucl. Phys. B 400, 240 (1993).

[167] K. Geiger and B. Müller, Nucl. Phys. B 369, 600 (1992).

[168] M. Gyulassy and X.-N. Wang, Nucl. Phys. B 420, 583 (1994).

[169] P.V. Ruuskannen, *Quark-Gluon Plasma*, ed. R.W. Hwa, (World Scientific, Singapore, 1990), Adv. Ser. on Directions in High En. Phys., Vol. 6, p519.

[170] S. Liuti, R. Vogt, Phys. Rev. C 51, 2244 (1995);
R.V. Gavai, R.M. Godbole, J. Phys. G 22, 25 (1996).

[171] D.M. Alde et al., Phys. Rev. Lett. 66, 133 (1990). J. Badier et al., Z. Phys. C 20, 101 (1983).

[172] C. Gerschel and J. Hüfner, Phys. Lett. B 207, 253 (1988).

[173] S. Gavin and J. Milana, Phys. Rev. Lett. 68, 1834 (1992).

[174] T. Gousset and H.J. Pirner, preprint hep-ph/9601242.

[175] A. Mücklich, Ph.D. thesis, Universität Heidelberg, 1995.

[176] G. Altarelli and G. Parisi, Nucl. Phys. B 126, 298 (1977).

[177] S. Kumano, Phys. Lett. B 378, 267 (1996).

[178] J. Qiu, Nucl. Phys. B 291, 746 (1987).

[179] S. Frixione et al., Nucl. Phys. B 431, 453 (1994);
P.E. Karchin, E769 Collab., Report No. FERMILAB-CONF-95-053-E.

[180] STAR Collab., Nucl. Phys. A 566, 277c (1994).

[181] T. Sjöstrand, Report No. CERN-TH.6488/92 (1992), on internet see *http://heplibw3.slac.stanford.edu/FIND/FREEHEP/NAME/JETSET/FULL.*

[182] P.H. Zhang et al., in The TALES/SPARHC EXPERIMENT at RHIC, p23.

[183] S. Gavin and M. Gyulassy, Phys. Lett. B 214, 241 (1988).